POLITECNICO DI MILANO

D.I.I.A.R.

Dottorato in Ingegneria

dell'Ambiente e delle Infrastrutture

XXIV Ciclo , 2009-2011

INVESTIGATION OF FLOW PATTERNS AND SEDIMENTATION IN RECTANGULAR SHALLOW RESERVOIRS

Ph. D. Thesis
Erica CAMNASIO
Matr. 738553

Supervisors: Prof. Enrico M. Orsi
Prof. Anton J. Schleiss
Tutor: Prof. Alberto Guadagnini
Coordinator: Prof. Fernando Sansò

ABSTRACT

This thesis deals with the classification of the different types of flow patterns that can develop in a rectangular shallow reservoir. After a bibliographic research, with the aim to get knowledge on the state of the art on the subject, the first part of the work has been an experimental activity carried out in the Laboratory of Hydraulic Construction at the Ecole Polytechnique fédérale de Lausanne. From this research, a wide overview has been obtained on the types of flow patterns that can develop in different reservoir configurations depending on reservoir geometry, at fixed hydraulic conditions.

The interest in the investigation of flow patterns types is generated by the strong influence that the fluid-dynamic of the reservoir exerts on the sedimentation processes inside the reservoir. The idea is that, if we better know the fluid-dynamics of the reservoir, then we could also manage in a more effective and efficient way the sediments deposits in the reservoir. So, as far as concerns sediments, experiments were also carried out in order to observe at laboratory scale the influence that the velocity field exerts on sediments deposition of suspended solids entering in the reservoir.

Then, a numerical activity has been carried out in collaboration with Liège University, with the aim to have a numerical model able to reproduce the velocity fields experimentally found. The experimental data previously collected have been the basis to validate the numerical model WOLF2D, which revealed to be able to reproduce in a quite accurate way and in numerous reservoir configuration, the experimental results. So, thanks to the validated numerical model, it has been possible to test new reservoir configurations, changing the boundary conditions of the problem. In particular not only the geometry of the reservoir could be easily modified, but also the hydraulic condition were varied, in order to extend the classification of the developing flow patterns not only as a function of reservoir geometry but also on the basis of the hydraulic conditions of the system, reaching a more complete view of the phenomenon.

The change of the hydraulic conditions opens a wide range of possible combinations of the non-dimensional hydraulic parameters of the system (mainly the Reynolds and Froude numbers), which

could lead to different types of flow patterns and to a future flow patterns classification not only based on the geometry of the reservoir but also as a function of the hydraulics of the reservoir.

For the moment, the change of the inlet Froude number, that is to say the Froude number of the inlet channel, has shown the existence of a new type of flow pattern, not registered in the previous experiments object of this thesis: it is the meandering flow, whose characteristics have been partially investigated in this thesis by numerical simulations. The aim is, in future, to collect quantitative experimental data in order to confirm the numerical model results, even if the existence of this type of flow pattern has been already assessed also from the experimental point of view.

The numerical model WOLF2D has been also endowed with a suspended sediments transport module, by which the deposition process of suspended load can be modelled; the aim is to reproduce the sediments deposits thickness and the global trapping efficiency of the reservoirs configurations experimentally tested, in order to develop a suspended sediment transport model available to simulate other reservoir configurations, changing sediments characteristics or hydraulics parameters, and evaluating their influence on the sedimentation processes.

Index

CHAPTER 1

INTRODUCTION AND MOTIVATION

This doctoral thesis focuses on the analysis of the hydrodynamic performance of shallow rectangular reservoirs. In this context, we start with the study of the different types of flow patterns which can develop in these types of reservoirs as a function of some geometric and hydraulic characteristic of the reservoir and then present some analyses on the interaction of the flow field with the transport and the deposition of suspended solids entering the reservoir.

The geometry of the reservoir and the imposed hydraulic conditions influence strongly the resulting flow pattern, giving raise to different types of large scale turbulent structures. These structures are typically called eddies or gyres and can influence significantly other processes taking place in the reservoir, such as pollutants transport and mixing or sediments deposition.

1.1. Motivation for the research

The key motivation for this doctoral work lies in the practical and compelling problem of reservoir sedimentation. It is well known that reservoirs are destined to be progressively filled up by the inflowing sediments. The sudden reduction of the flow velocity in the lake (which is typically much lower than that of the inflowing river) causes the suspended sediments to deposit. Several studies have been devoted to the problem of reservoir filling up with sediments (e.g., Morris and Fan, 1998; Kantoush, 2008). Besides of reducing the available water volume contained in the reservoir, sediments deposition in proximity of the intake structures of hydroelectric power plants negatively affects the hydraulic performances of the entire plant and can totally prevent the functioning of gates and other hydraulic structures.

At the beginning of these PhD studies, the aim was to concentrate the research on the subject of reservoir sedimentation but it was soon realized that there is strong link between the reservoir fluid-

dynamics and the sediment transport and deposition phenomena; so, it has been first of all necessary to concentrate on the detailed analysis of the characteristics of the flow field developing in the reservoirs, as a function of geometric and hydraulic conditions. In fact, if the influence on the flow field of the boundary conditions was well known it would be also much easier to operate on sediments behaviour and distribution in natural or artificial reservoirs.

1.2. Practical applications of flow patterns study

Beyond the benefits that an in-depth understanding of flow field characteristics and sediments behaviour could lead to shallow reservoir management operations, the investigations of this thesis contribute to other practical engineering applications. For example, understanding the influence of reservoir geometry on flow field and sedimentation processes can be useful for effective designs of primary settling tanks or sedimentation basins in hydroelectric and depuration plants, or the design of storage chambers along sewers systems (e.g., Stovin, 1996; Dufresne, 2008;). In particular, knowledge of the flow field which develops in the tank as a function of geometry and hydraulic conditions can lead to improved estimates of the trapping efficiency of these hydraulic structures and their general performances, leading also to the effective planning of their management and maintenance operations.

Large shallow basins are also frequently used for other types of treatments, including waste stabilization, oxidation, cooling or disinfection. In these cases, the efficiency of the treatment depends strongly on the actual residence time, which is in turn influenced by the type of flow pattern that develops in the basin. Thackston et al. (1987), Hannoun and Boulos (1997) and Wood et al. (1998) among others, dealt with this subjects. They studied the residence time distribution of some tracers inside the reservoir to prevent the formation of short-circuiting (i.e., the most direct path of the water from the inlet to the outlet) and dead water zones (i.e., zones with stagnant water).

Persson et al. (1999), Persson J. (2000), and Persson and Wittgren (2003) studied the hydraulic efficiency of constructed wetlands for stormwater management because "poor wetland hydrodynamics are often identified as a major contributor to wetland management problems". Ponds with a high hydraulic efficiency are expected to promote full utilization of the available detention volume and near plug flow conditions."

The key characteristics of the flow fields developing under different configurations within aquaculture tanks are also of high interest (Oca and Masalò, 2007). Understanding the precise flow pattern is conducive to design these structures ensuring optimal fish culture conditions. The occurrence of short-circuiting and dead water zones with low renovation rates can lead to insufficient water mixing and to the formation of preferential zones for bio-solids sedimentation. These conditions clearly impact the life conditions of the fish in the tank (Oca et al., 2004). On the contrary, when strong velocity gradients take place in the tank, territorial behaviours emerge and agonistic interactions arise between fish. Furthermore, the average velocities in the tank should not be exceedingly large, in order to limit the fish energy expenditure for swimming, but they should be large enough to allow self-cleaning of the tank.

1.3. Scope of the work

The first aim of this doctoral research is to identify and classify the different types of flow patterns that can develop in a shallow rectangular reservoir, depending on its length-to-width ratio and expansion ratio. This has been accomplished on the basis of a detailed series of laboratory-scale experiments within which the hydraulic conditions are fixed while different geometries are adopted. Then, numerical simulations have been performed by using the depth-averaged two-dimensional code WOLF2D and compared to experimental results. Two different turbulence closures were tested and their key advantages and disadvantages have been analyzed in direct comparison against data. The assessment of the capability of the numerical model to interpret the laboratory

experiments has allowed employing WOLF2D to test numerically other reservoir configurations which were not subject to laboratory investigation due to physical constrains of the experimental facility. The influence of selected hydraulic conditions of the system on the flow pattern developing within the reservoir has been analyzed numerically and the results have been assessed in terms of appropriate dimensionless quantities, i.e., Froude, Strouhal and Reynolds numbers.

Varying the hydraulic boundary conditions for a given reservoir geometry has highlighted the onset of a *meandering flow pattern* within the reservoir. This phenomenon has been scarcely studied in the literature, even if its occurrence has been evidenced by means of published laboratory experiments (Kantoush, 2008). Here, detailed numerical investigations have been focused on the analysis of the oscillation frequency of the meandering jet; a future objective is providing experimentally-based reliable quantitative observations against which numerical results can be compared.

An additional set of laboratory investigations has been performed to study the influence of a variation of the location of the inlet and outlet channels of the reservoir on the developing flow pattern and consequently on reservoir trapping efficiency. Laboratory experiments have been performed upon considering three asymmetric reservoir configurations, measuring both the velocity fields and the thickness of sediments deposits by the inflowing suspended load.

The numerical model WOLF2D has been extended with an original sediment transport module. This has allowed to numerically simulate the processes of sedimentation and deposition observed at the reservoir bottom. For the moment preliminary simulations have been performed, in order to test the good functioning of the model. In the next future the calibration of the parameters will aim at reproducing with more accuracy the sediments deposits distribution on reservoir bottom.

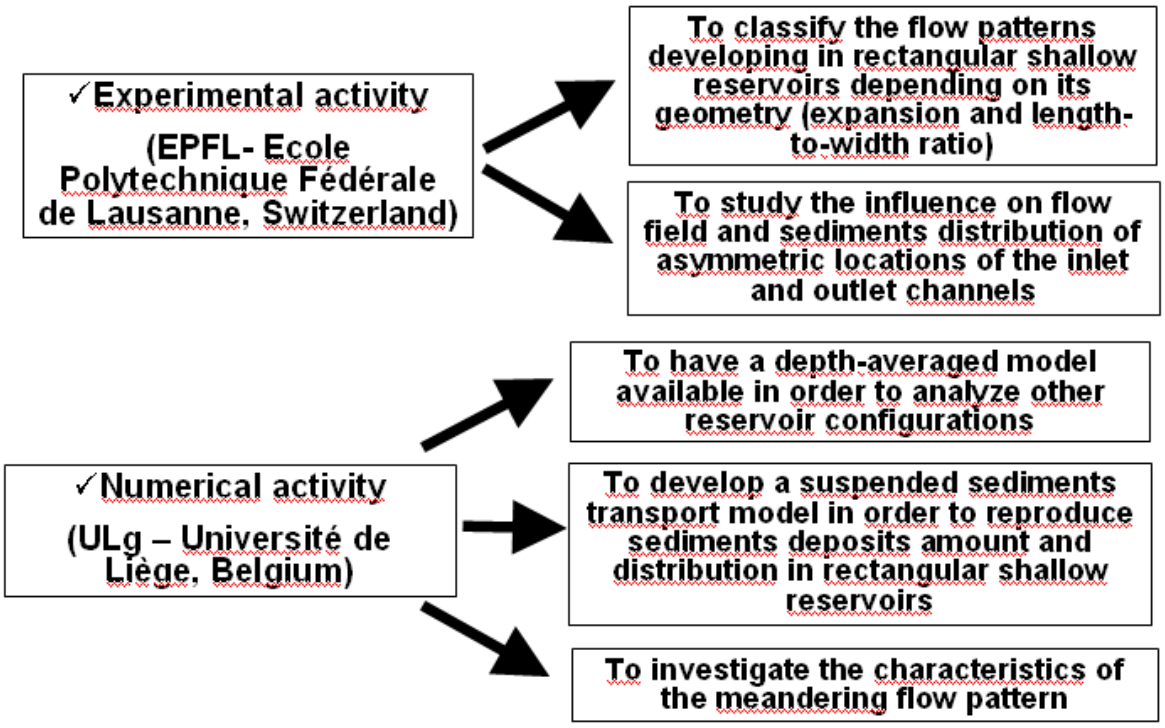

Figura 1. 1 – Thesis outline: main constitutive parts and respective objectives

CHAPTER 2

RESEARCH CONTEXT

In this chapter, the present state of the scientific research on the main subject dealt with in this thesis is shortly summarized. In fact, many authors, involved in fluid mechanics studies, have tried to investigate the relationship between the type of flow field, the geometry of the system and the hydraulic conditions of the experiments, by both experimental works and numerical simulations.

In particular, three authors have investigated the relationship existing between the flow patterns and the sedimentation processes, trying to arrive to a link between the geometrical characteristics of the tank and its trapping efficiency.

Moreover, these studies of the flow patterns has revealed the existence of phenomena of instability which have been partially studied but which have been not yet fully explained.

2.1. Main related research

The work presented in this thesis has commune features with three recent research which dealt with the problem of the influence of geometry on the fluid-dynamics and with the influence of the flow patterns on sedimentation. Moreover, the following authors combined, as in the present work, experimental activities and numerical modelling:

- The strongest link is with the work of Sameh Kantoush (2008), who started to perform experiments in the same laboratory facility at EPFL where the experiments here presented have been carried out. The author started in investigating, by LSPIV and by UVP, the flow patterns developing in different rectangular reservoir configurations: he started from a 6x4m reservoir, then he progressively reduced the length of the reservoir, with a fixed width B = 4 m, or, on the contrary, he fixed the length of the reservoir L = 6 m and varied the width of the reservoir, observing the flow pattern type which developed in each of these

configurations. He observed that an asymmetric flow field could arise in some particular reservoir configuration despite the symmetry of the geometry. Then, he developed an index, called SK, in order to distinguish between reservoir configurations leading to symmetric or asymmetric flow patterns. Anyway, the work carried out in the framework of the present thesis, has much enlarged the range of reservoir configurations tested by Kantoush, leading to a more complete overview on the types of flow patterns that can develop in a rectangular reservoir as a function of its geometrical characteristics at constant hydraulic conditions, as it will be shown in the following chapters.

Besides the analysis of rectangular reservoirs, Kantoush analysed also the flow pattern that develops in a lozenge shaped reservoir and he also varied the Froude number of the experiments, showing the possible existence of an oscillating flow field, without deepening the analysis of the characteristics of this type of time dependent flow. In this thesis, on the contrary, a chapter is specifically dedicated to the quantitative study, by numerical simulations, of the characteristics of the oscillation of this meandering flow pattern.

Kantoush performed also tests with an inflowing suspended load and he measured the thickness of sediments deposits on reservoir bottom for some rectangular reservoir configuration. He observed that the presence of sediments was able to change the flow pattern in the reservoir. Kantoush also performed flushing operations tests, after the test of sediment deposition, in order to study the evolution of the erosion cone caused by the re-suspension of the deposited particles.

In the framework of this thesis, other tests with a suspended solid inflow have been performed, but in this case the reservoir configurations analysed have asymmetric position of the inlet and of the outlet channel, as it will be wider explained in the following chapters.

Kantoush also tried to reproduce in his PhD thesis the flow patterns that he had found during the experiments, in particular using the software CCHE2D. Afterwards, he tried to move to a

three-dimensional simulation of the process, using an approach LES (large eddy simulation) in which the Navier Stokes equations are spatially filtered (Ushijima et al., 2009).

- An other important branch of research about flow patterns and sedimentation, is constituted by the work of Virginia Stovin (1996), which focused her attention on the study of sedimentation in storage chambers for sewers systems. The main contribution of her work has been to develop empirical relationship to predict the efficiency η of a storage chamber as a function of some of its geometrical characteristics, and considering also the type of sediments entering the tank. Besides the influence of the length-to-width ratio, she also considered the longitudinal slope of the storage chamber and the slope of the lateral walls, parameters that were integrated in the empirical non-dimensional relationships. For the simulation of deposition or erosion of the particles on the bottom of the reservoir, she developed two types of methods: one is based on a bed shear stress criterion, the other is a particle tracking methods. Anyway, her work didn't aim to reproduce the long-term accumulation of sediments on reservoir bottom. In fact, for example when using the particle tracking method, if a solid particle touch the reservoir bottom, it simply disappears from the simulation, and the efficiency is simply linked to the computed number of particle that collide with the bottom.
- Matthieu Dufresne, during his PhD thesis at Strasbourg University (2008) and his post-doctoral staying at Liège University (2010), strongly contributed to the research on flow patterns and sedimentation, and his works constitute for large part the basis for the further studies carried out in this thesis, as it will be shown later (see Chapter 4).

  During his PhD thesis Dufresne carried out experiments at laboratory scale and he also tried to extrapolate some of his conclusions to field cases. He performed, like Stovin, three-dimensional simulations by the commercial software Fluent. The geometry simulated by the author in the framework of his thesis is quite different from the rectangular shallow reservoir of EPFL, because it was constituted by a tank endowed by a circular inlet channel.

Moreover, he investigated the role in influencing the efficiency of the storage chamber of vertical stages placed inside the tank: in fact, with their presence they could affect the fluid-dynamics of water in the chamber and consequently they could influence the deposition of sediments.

On the contrary, during his post-doctoral staying at EPFL, Dufresne analysed the flow patterns and the sedimentations processes in a laboratory facility very similar to that of EPFL:. The differences with the present work, which well integrate itself with the research of Dufresne, are: first, about the sedimentation aspects, the author dealt with bed load transport, while the present thesis concerns suspended load transport studies; secondly, about flow patterns classification, Dufresne concentrated mainly on the study of the reattachment length, while the present research tried to depict the entire flow field developing in the different reservoir configurations by velocity measurements.

2.2. Other studies about flow patterns investigation

The investigation of flow patterns, and in particular of the geometric and hydraulic conditions that lead to the formation of a specific type of flow pattern, has been object of the research of many authors, who studied the behaviour of water jets, free-surface or pressurized ones, in different hydraulic regimes (laminar or turbulent), in correspondence of sudden expansions. In fact, the case of a channel entering a rectangular reservoir can be effectively considered as a jet subjected to a two-dimensional sudden expansion, confined laterally and downstream by the reservoir walls, and vertically by the water table, in contact with the atmosphere.

The visualization of flow trajectories is performed upon injecting dye or small seeding particles in the flowing water. This allows visualizing the flow pattern when they are lightened. Moreover, Laser Doppler Anemometry (LDA) and the quite recent development of Particel Image Velocimetry (PIV) and Large Scale Particle Image Velocimetry (LSPIV) have given the

possibility to identify with more precision, and in a quantitative way, the characteristic of the flow field, arriving to the representation of vectorial velocity maps.

Here a quick chronological overview on the most important works carried out about flow patterns investigation and instability phenomena is presented:

- The work of Abbott and Kline (1962) is one of the earliest studies in the field of flow pattern investigation. These authors investigated the behavior of a turbulent free-surface jet subjected to a sudden expansion of infinite length. The authors found that for small expansion ratios ($B/b<2$) the flow pattern is symmetric, with 2 small stall regions on the sides of the main jet near the expansion, followed by a channel like flow, that is to say a flow with uniform velocity distribution. Otherwise, for expansion ratios larger than this limit, the flow field becomes asymmetric, with the main jet deflected to one lateral wall.

  A variation of the inlet Reynolds number (tested range 10.000 – 100.000) and of turbulence intensity at the inlet was found not to have any influence on flow pattern and on reattachment length of the jet to the lateral walls. The flow was found to be essentially two-dimensional, except for a very small region near the expansion. Anyway, as it has been underlined, this case concern the study of an expansion with infinite length, so the influence on the flow field of the length-to-width ratio was not taken into consideration.

- The works of Durst et al. (1974) and Cherdron et al. (1978) considered air flow at low Reynolds numbers, in laminar regime and in a pressurized conduit, and they showed that the flow pattern presents a transition from symmetric to asymmetric when the Reynolds number is increased. Critical Reynolds numbers corresponding to the transition between the flow fields were identified. Moreover, they found that the length of the lateral recirculation regions on the side of the main jet of the symmetric flow, increases with the increase of the Reynolds number.

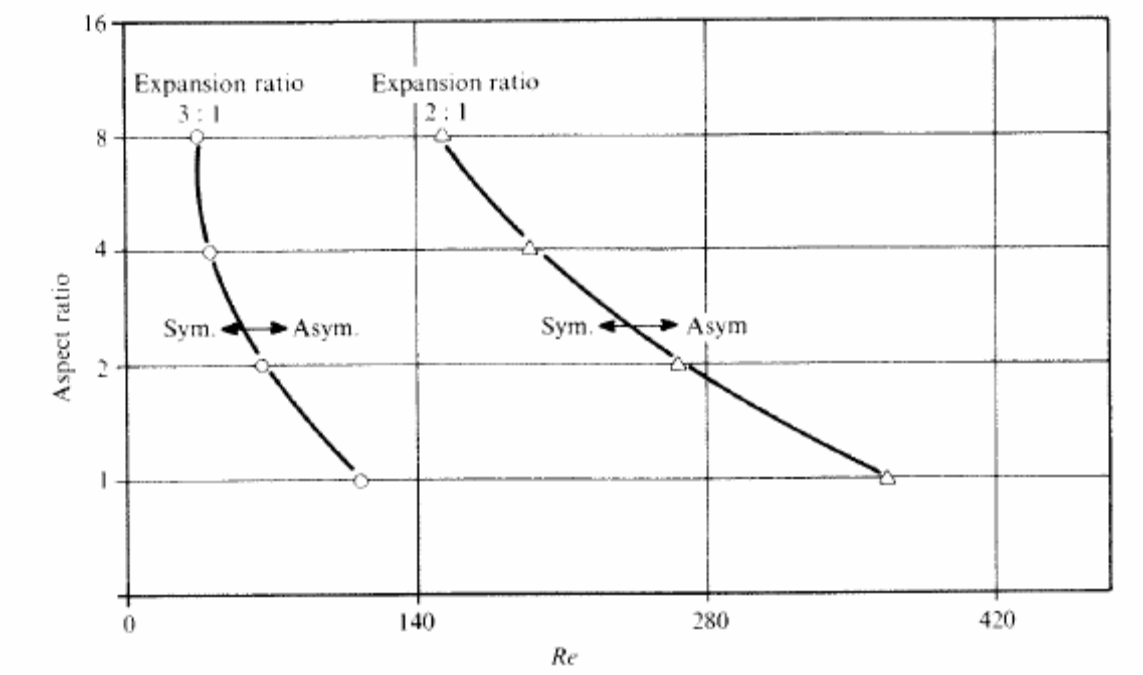

Figure 2. 1– Classification of asymmetric or symmetric flow fields according to Cherdron et al. (1978), as a function of the Reynolds number, the aspect ratio B/h and the expansion ratio of the conduit

The critical Reynolds number at which the transition occurs, is influenced by the expansion ratio and also by the aspect ratio *B/h*, as demonstrated firstly by Cherdron et al. (1978) and confirmed afterwards by other authors (e.g. Escudier et al., 2002). In particular, Cherdron demonstrated that reducing the expansion and the aspect ratio has a stabilizing effect on the flow field, postponing the occurrence of the asymmetric field to larger Reynolds numbers (Figure 2.1).

- Fearn et al. (1990) identified with their experiments also a time-dependent flow field, which arises when further increasing Reynolds number. The occurrence of this type of flow field is attributed by the authors to the increased importance of three dimensional effects at larger Reynolds numbers.
- Mizushima and Shiotani (2000; 2001) studied numerically and experimentally, by flow visualizations, the instabilities of a flow in channel with a suddenly expanded and contracted part. They observed the transitions that occur between different types of flow patterns, as a function of the Reynolds number. They found that sometimes multiple stable steady state solutions can co-exists for a same Reynolds number. This fact means

that we are in presence of a bifurcation phenomenon, that is to say that multiple solution of the Navier-Stokes equation exist, given the same boundary condition.

- Escudier et al. (2002) analyzed the turbulent flow through a plane sudden expansion of modest aspect ratio. They state that "symmetric flow is a valid but unstable solution to the Navier-Stokes equation"; for this reason, an unsteady simulation is needed to assess if the resulting symmetric flow field is stable or unstable, evolving with time towards asymmetry. Moreover they say that "a strongly asymmetric flow generated in a symmetric geometry represents a major challenge to the CFD community".
- Battaglia and Papadopoulos (2006) developed the concept of effective expansion ratio, incorporating in one index the influence of expansion ratio and aspect ratio, but they did not consider the influence of the length to width ratio. They demonstrated that the side walls proximity enhances the flow stability, that is to say that, for smaller expansion ratios, the transition to the asymmetric flow field occurs at larger Reynolds numbers.

In conclusion, the analysis of the existing body of research suggests that further research is needed to fully understand and model the combined influence of geometry and hydraulic conditions on the flow patterns developing within shallow reservoirs. In particular, while existing studies have focused on the effects of the Reynolds number and on laminar regimes, the present research emphasises the influence of the Froude number in the presence of turbulent flow conditions, Particular relevance will be given to the study of the phenomenon of instability and bifurcation (co-existence of multiple solutions of the Navier-Stokes equations) that could generate during transition from a symmetric to an asymmetric flow configuration.

CHAPTER 3

EXPERIMENTAL ACTIVITY

The main experimental activity was carried out in the Laboratory of Hydraulic Constructions (LCH) at the Ecole Polytechnique Fédérale de Lausanne (EPFL). The experiments are aimed at analysing the influence of some geometrical parameters on the type of flow fields developing in a rectangular shaped shallow reservoir.

In particular, several rectangular reservoir configurations having different length-to-width ratio and expansion ratio were analysed, identifying the different kinds of flow field developing in the reservoir as a function of the values of these two non dimensional geometrical parameters, at constant hydraulic conditions. The length-to-width ratio is the ratio between the length of the reservoir and its width, while the expansion ratio is the ratio between the width of the reservoir and the width of the inlet channel. As demonstrated by pre-existing studies, dealt with in the previous chapter, these two non-dimensional parameters have a strong influence on the type of developing flow pattern, and in particular on the onset of an asymmetric flow field despite the symmetry of the geometry.

The second part of the experimental research concerned the study of the influence of the location of the inlet and outlet channel on the flow field and on the deposition of sediments on the reservoir bottom. So, besides the measurements of the velocity field, in this case also tests with a controlled sediments inflow were performed and the thickness of sediments deposits was measured after 4 hours of sediments supplying.

In this chapter, the characteristics of the experimental facility, the measurements methods and the experimental procedures of the tests are presented.

3.1. The experimental set-up

The experimental facility at LCH consists in a rectangular shaped PVC shallow reservoir, with a flat smooth bottom (Figure 3. 1). The maximum horizontal dimensions of the reservoir are a width B = 4 m and a length L = 6 m, while the maximum water depth is h = 0.30 m. The water enters into the reservoir by an horizontal rectangular channel having a width b = 0.25 m and then goes out by an identical channel placed on the opposite side of the reservoir. On the outlet channel a flap gate is placed, acting as a weir, in order to regulate the water level in the reservoir. Both the channels can be moved in different locations along the upstream and the downstream wall of the reservoir, in order to realize geometrical configurations having asymmetrical positions of the inlet and of the outlet channels.

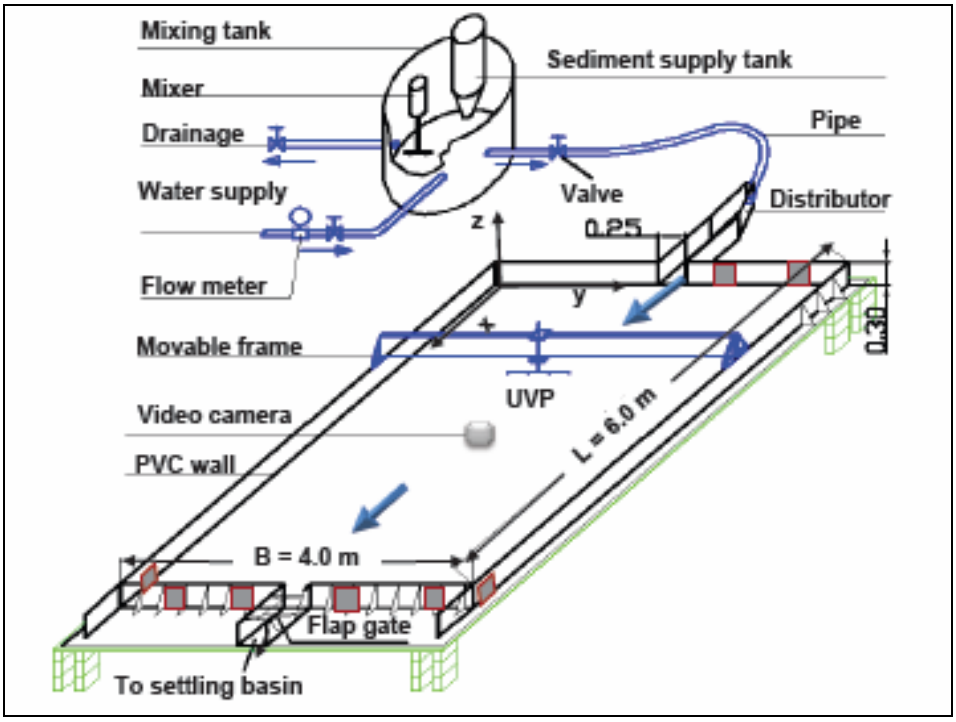

Figure 3. 1 - Experimental facility (Kantoush, 2008)

The movable PVC walls allow to change the inner dimensions of the reservoir in order to obtain configurations having different length-to-width ratio L/B and expansion ratio B/b.

The reservoir is linked to the hydraulic circuit of the laboratory, so the water is circulated by a pump in a conduit, on which an electromagnetic flow meter is installed. The conduit leads to the

mixing tank, which is a cylindrical tank allowing (during the tests with sediments) the mixing between sediments and water by a rotating propeller. The sediments fall by gravity from a sediment supply tank into the mixing tank. A vibrator and an adjustable opening at the bottom of the sediment supply tank allow to regulate the sediment discharge directed to the mixing tank.

Then, from the mixing tank the water is lead by gravity to the shallow reservoir by a PVC pipe with a diameter of 10 cm. On the inlet channel, a series of honeycombs and thin grids are placed in order to reduce the turbulence of the inflowing water.

An aluminium bar mounted on wheels running on the two lateral sides of the reservoir allows to carry the transducers for UVP measurements (paragraph 3.3.2). An high frame-rates camera for LSPIV measurements is placed over the reservoir at an height of about 3 m.

The water going out from the reservoir is lead first to a settling basin, in which some filters are placed, and then it is re circulated in the laboratory hydraulic circuit.

Figure 3. 2– Photo of the experimental facility (Kantoush, 2008)

3.2. Similarity with prototype

The experimental reservoir of the LCH laboratory had been initially created as a schematic model of a real shallow reservoir existing along the Rhone River (Bollaert, et al, 2000; Kantoush et al., 2005). The geometric scale of the model is approximately 1:50. It means that the dimensions of the reservoir at field scale are a width of the order of 200 m, a length of 300 m, and a depth of 10 m, with an inflowing channel 12.5 m wide.

The geometric scale λ_G is the ratio between the geometric dimensions of the prototype L_p and the geometric dimensions of the model L_m :

$$\frac{L_p}{L_m} = \lambda_G = 50 \qquad (3.1)$$

As typical for free-surface flows, a Froude similarity has been applied, in order to keep the same inlet Froude number F_{in} for the prototype and for the model. In this way, the scale for the velocity λ_V can be obtained as referred in the following formulations:

$$F_{in\_p} = F_{in\_m} = \frac{V_p}{\sqrt{g \cdot L_p}} = \frac{V_m}{\sqrt{g \cdot L_m}} \qquad (3.2)$$

$$\frac{V_p}{V_m} = \lambda_V = \frac{\sqrt{L_p}}{\sqrt{L_m}} = \sqrt{\lambda_G} = 7.07 \qquad (3.3)$$

To find the scale for the discharge λ_Q the following procedure must be followed:

$$\frac{Q_p}{Q_m} = \lambda_Q = \frac{V_p \cdot L_p^{\,2}}{V_m \cdot L_m^{\,2}} = \sqrt{\lambda_G} \cdot \lambda_G^{\,2} = \lambda_G^{\,5/2} = 17677 \qquad (3.4)$$

The results of the application of the Froude similarity law are referred in Table 3. 1.

Table 3. 1 – Geometric and hydraulic characteristics of the prototype at field scale (Rhone river) and of the nodel at laboratory scale (LCH laboratory)

	Prototype	**Scale**	**Model**
Reservoir length [m]	300	$\lambda_G = 50$	6
Reservoir width [m]	200	$\lambda_G = 50$	4
Reservoir depth [m]	10	$\lambda_G = 50$	0.2
Width of the inlet channel [m]	12.5	$\lambda_G = 50$	0.25
Inlet Velocity [m/s]	0.98	$\lambda_V = \sqrt{\lambda_G} = 7.07$	0.140
Discharge [m^3/s]	123	$\lambda_Q = \lambda_G^{5/2} = 17677$	0.007

3.3. The measurements methods

In this section the techniques of measurement adopted to describe the velocity field from a qualitative (streamlines) and quantitative (vectorial velocity maps) point of view will be presented, together with the methods used to monitor the concentration of the suspended load and to measure the thickness of sediments deposits on the bottom of the reservoir.

3.3.1 LSPIV measurements

The Large Scale Particle Image Velocimetry (LSPIV) is a quick and quite cheap way to obtain the average and the turbulent velocity field at the surface of a water body. Furthermore, this method allows to track in a simple way the two dimensional large coherent eddy structures which characterize shallow water flows (Weitbrecht et al., 2002; Kantoush and Schleiss, 2009).

This technique consists in registering a sequence of images of the water surface, seeded by apposite tracers, by an high frames rate video camera. The difference with standard PIV applications, is that no laser light is needed to apply the LSPIV, since natural light is generally sufficient to lighten the tracers on the water body. In some case, for example inside hydraulics laboratories, it is better to

add some artificial spot light to achieve a uniform lightening of the tracers, that is necessary to obtain correct results. An other difference between the typical PIV and the LSPIV is that large surfaces can be investigated at one time by LSPIV (Meselhe et al., 2004), while PIV allows to investigate only the small portion of the flow field that is reached by the laser light.

An other merit of the LSPIV is that it is a non-intrusive measurement technique. Anyway, the tracers must be chosen with great attention, since they must faithfully follow the water trajectories, so, not only they have to float on the water; but also they must be light enough in order not to have a proper inertia.

In the specific case of the experiments in the LCH laboratory, white plastic particles with an average diameter of 2 mm were used as floating tracers. They were manually spread before the beginning of the experiment over the water surface, in order to have an initial insemination of the different parts of the water body. Then the water was circulated by the pump and the tracers were continuously added to the inflowing water in correspondence of the inlet channel, in order to guarantee a continuous seeding of particles.

At least four spot lights were placed around the reservoir, keeping attention that they didn't cause direct light reflections on the water table, which would have disturbed the regular data acquisition; the aim of the spot light was simply to assure a uniform environmental light to have a good lightening of the white seeding particles on the water table, making a good contrast with the dark gray colour of the walls and of the bottom of the reservoir.

The images of the water table seeded by tracers were recorded by a CMOS Camera with USB interface (SMX-155 USB2.0) registering 8 – 10 fps, and showing in real time on the personal computer the video recorded during the acquisition. This quite low frequency of acquisition is justified by the fact that the velocity in the reservoir were not much high (maximum velocity 0.14 m/s), so the tracers moved quite slowly, and a few pictures per second were sufficient to describe their displacement.

The camera was placed at an height of about 3 meters over the reservoir, in the way that it was possible to have an entire view of all the reservoir surface even in its largest configuration (6x4m), except for a small portion less than 50 cm wide, near the inlet channel).

Images were taken for about 3 minutes for each experiment: in this way it was possible to collect about 1500-1800 images on which the cross-correlation algorithm could be applied in order to arrive, after some filtering operation, to depict the average flow field of the reservoir.

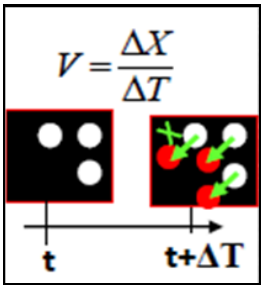

Figure 3. 3 – Basic principle for cross-correlation between successive images

First, the images acquired by the camera were subjected to a process of un-distortion using a Matlab routine, in the way to remove the optical distortion caused by the lens of the camera.

Then, using the commercial software of Dantec Dynamics, Flowmanager (User's Guide, 2000), the cross-correlation between two successive images and the image treatments necessary to "clean the signal" could start.

The concept of cross-correlation, that is nowadays at the basis of numerous commercial softwares, can be explained briefly in this way: first of all, a small area of the image, the so-called interrogation area (that generally has the width of 32 or 64 pixels), is chosen; then, the same interrogation area in the following image, that has been taken after a time ΔT, is considered. As it is shown in Figure 3. 3, during the time ΔT between the two images acquisition, the particles have moved to the red position, so a displacement vector ΔX can be individuated. The velocity V of the tracers, and consequently of the water, is simply given by the ratio between the spatial displacement ΔX and the time interval ΔT between the 2 images. Of course, this operation is repeated for all the interrogation area that together form the entire reservoir surface. At this point of the process, we

have the instantaneous flow field derived from the cross correlation of two successive images; then, if we repeat the cross correlation algorithm for all the available images, and we average all the instantaneous flow field produced by cross correlation, we obtain in the end the average flow field of the entire reservoir.

Unfortunately, during the process, many outliers vectors can appear, due to incorrect correlations between particles of two successive images, or due to lack seeding or excessive seeding in the experimental set-up. Nevertheless, different techniques to reach a good quality of the resulting flow field can be applied: in particular, in this case first the outliers vectors have been individuated by the peak validation method (Flowmanager User's Guide, 2000) and removed. Afterwards, a moving average validation has been applied: this operation compares the value of the velocity vector in one cell of the reservoir, with the value of the neighbour vectors; if the value of the central vector is too much different from the value of the surrounding vectors, the central vector is replaced by an average of the surrounding vectors. In this way, the velocity field is "smoothed" and too high/too low velocity vectors are removed. Further details about the procedure of validation of the experimental data acquired by LSPIV can be found in the master thesis of Celenza (2010).

In the end, despite all the precautions to well lighten the water surface and to seed in a uniform way the water surface, the results obtained by LSPIV for this thesis were simply streamlines plots (Figure 3. 4); in fact, it hasn't been possible to consider as valid data the modules of the velocity vectors obtained by LSPIV, since the resulting flow field didn't respect continuity. However, the streamlines plots have been very useful to distinguish the different types of flow fields, because they indicated clearly the shape and the positions of the horizontal large scale turbulent structures depending on reservoir geometry. So, thanks to the LSPIV technique, it has been possible to test a great number of reservoir configurations in a reasonable time, since the time necessary for an LSPIV acquisition is only of some minutes, even if every experiment is preceded and followed by a lot of practical operations that lengthen the total time dedicated to an experiment.

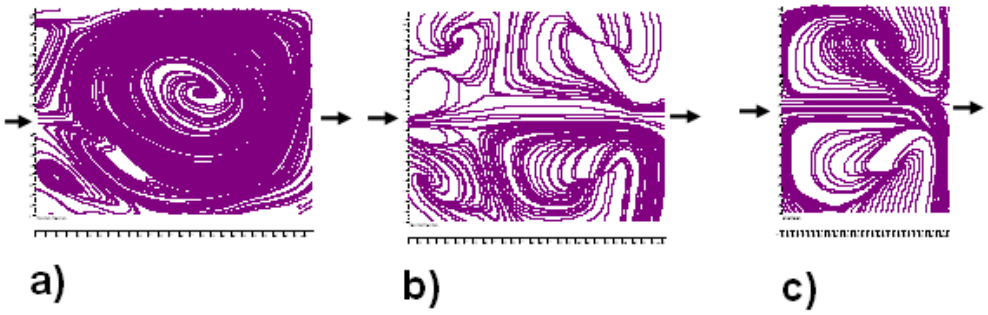

Figure 3. 4 – Examples of streamlines plots (top view of the reservoir surface) resulting from Flowmanager image treatment, corresponding to a) A1 flow field, b) S1 flow field, c) S0 flow field. For details about the typology of these flow patterns, see chapter 4.

3.3.2 UVP measurements

Generalities

Ultasound Velocity Profilers technique is a widely utilized method to measure flow velocity. Details about this measurement technique can be found in the user's guide of the instrument (Metflow, 2002) and in the thesis of Carrara and Gervasoni (2010).

In the present case, velocity measurements were made to investigate the horizontal velocity field in the experimental reservoir. Since the reservoir depth h is much smaller than its horizontal characteristic length scale L ($h/L<<1$), the vertical velocity component w can be neglected, as is typical for shallow free surface flows (Vreugdenhil 1994), and as was also confirmed by additional model measurements.

A horizontal movable square grid of 1 m × 1 m equipped with 8 UVP transducers (2 MHz) four placed along the x direction and four along the y direction, which allowed to measure the horizontal velocity components u and v along the transducer axis, (Figure 3. 5).

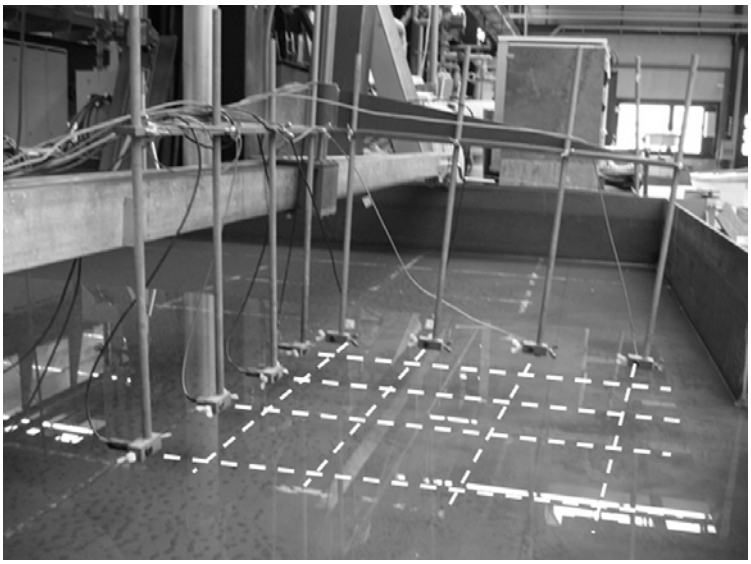

Figure 3. 5 - Movable square grid formed by 8 UVP transducers utilized for horizontal velocity components measurements. Directions of measured horizontal velocity profiles are represented by dashed lines

The maximum distance from the instruments was 723 mm based on the velocity range recordable by the transducer of ±0.189 m/s (Metflow 2002). The horizontal velocity vectors were determined at the 16 points formed at the intersections between the velocity profiles recorded by each transducer (Camnasio et al., 2010b). The distance between each measurement point was ~24 cm. Each transducer acquired 150 velocity profiles (Figure 3. 6) during 80 s; these can be considered to represent the instantaneous velocity.

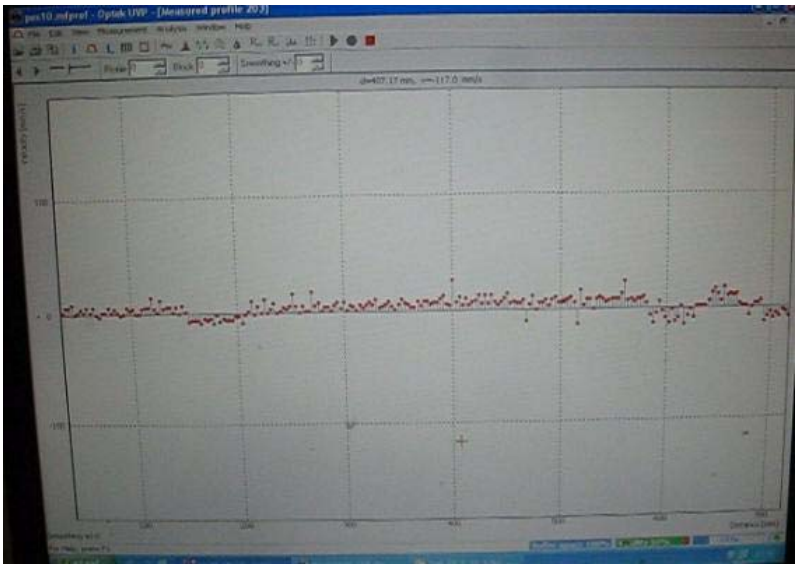

Figure 3. 6 – Example of instantaneous velocity profile recorded by a UVP transducer

However, the profiles were automatically subdivided by the acquisition software in 15 subsets, which result in 15 average velocity maps, showing the velocity vector in each of the 16 points of intersection between the velocity profiles of the transducers grid. The final map of the average velocity field was obtained by averaging the 15 velocity maps (Figure 3. 7).

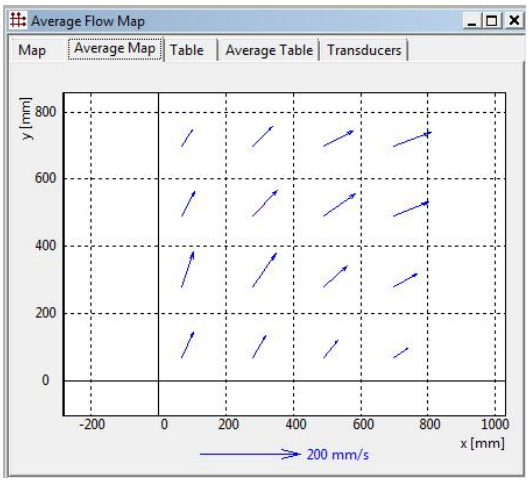

Figure 3. 7 – Example of the average velocity maps obtained by UVP measurements

After having acquired the data at one reservoir location, the grid was moved to the next position, thus covering step-by-step the entire reservoir surface. For the largest reservoir configuration of 6 m × 4 m), 24 grid positions were necessary, corresponding to 384 measurement points regularly distributed all over the reservoir (Figure 3. 8).

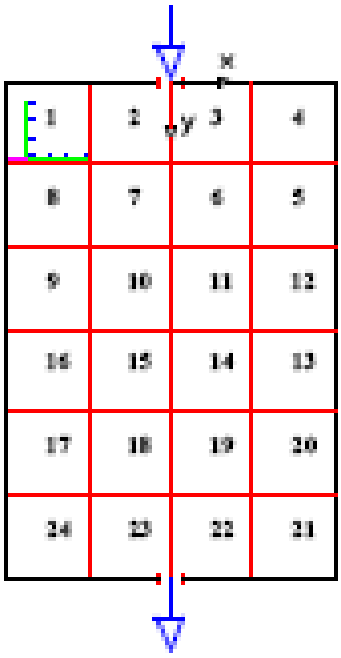

Figure 3. 8 – Top view of the grid formed by the successive positions of the UVP instrumentations on the reservoir surface (24 grid positioning are necessary for the reservoir 6x4 m).

Therefore, the recorded velocity field was in principle not instantaneous, but the steady flow condition (constant discharge and depth) and the macroscopic steadiness of the flow patterns guaranteed the steadiness of the recorded average velocity fields. Longer measurement durations would be necessary in the future to identify more accurately the effective mean velocities, and not only the time-averaged quantities presented in this thesis. By matching the average velocity maps to the reference coordinate system of the reservoir, the average horizontal velocity field was obtained: it allowed to classify the different types of flow patterns as a function of reservoir geometry, indicating also quantitative information on the intensity and on the direction of velocity vectors.

Due to practical problems in grid positioning, a band having a width negligible compared to the entire reservoir surface, could not be experimentally investigated along all the reservoir perimeter. Note that UVP measurements are an invasive method, since transducers are submerged into water, yet the transducer presence did not affect the measured flow fields. Since velocities are small, the transducer affects velocity data only within its vicinity (in a radius of a few millimetres), not affecting the measurement in correspondence of the first measurement point.

As it will be explained more in detail later, horizontal velocity vectors at various heights z from the reservoir bottom (z = 0.01, 0.06, 0.11, 0.18 m) and in several reservoir locations were measured, to define the average shape of the vertical profile versus distance z. Since the average velocity profile is logarithmic, it was decided to set the UVP transducers at height z = 0.08 m (0.4h), so that the measured velocity represents the mean vertical velocity (Graf and Altinakar 2008).

UVP measurements of the vertical velocity component $w(z)$ were carried out as well, as the flow is in principle not completely two-dimensional (Abbott and Kline 1962, Casarsa and Gianattasio 2008). To apply the shallow-water theory, the order of magnitude of the vertical velocity must be inferior or equal to the order of magnitude of the product between the horizontal velocity scale and h/L (Pedlosky 1979). In the present case, $h/L = O(10^{-2})$, the horizontal velocity scale is $O(10^{-1})$ m/s, so the vertical velocity component must be of the order of some mm/s, as confirmed by vertical velocity measurements. Therefore, the horizontal velocity components are sufficient to describe the main characteristics of the reservoir flow field, in particular the large-scale turbulent structures, which have a vertical axis. These turbulent structures have dimensions of the order of the reservoir length scale L, they contain the main portion of the kinetic energy and depend on the geometric boundary conditions (Versteeg and Malalasekera 1995).

Table 3. 2 - Characteristic parameters used for UVP acquisition.

Maximum measurable depth	723 mm
Velocity range of measurement	-0.189 m/s ÷ + 0.187 m/s
Number of samples: profiles acquired for every transducer during one cycle	10
Number of transducers	8
Number of cycles	15
Minimum sampling time	39 ms
Delay between transducers	100 ms
Delay between cycles	100 ms

SIGNAL	
Transmitting frequency	2 MHz
Number of cycles per pulse	4
Number of repetitions	32
Channel width (spatial resolution)	1.48
MEASUREMENT WINDOW	
Start - End	33 - 721 mm
Number of channels forming every profile	232
Channel distance	2.96

Temporal stability of the average velocity

To assess the adequacy of the performed UVP measurements, an analysis about the temporal stability of the average velocity calculated at each measurement point on the basis of the successive 15 flow maps was performed.

In fact, in a turbulent flow, according to the RANS approach (Reynolds Averaged Navier Stokes), the instantaneous velocity vector $\boldsymbol{V}$ can be decomposed in the following way:

$\boldsymbol{V} = V + V'$ *(3.5)*

where V is the average velocity and V' represents the turbulent fluctuation. By definition, the mean of the fluctuations is zero.

The average velocity V, in a stationary flow field, is defined as follows:

$$V = \lim_{t_1 \to \infty} \frac{1}{t_1} \int_0^{t_1} V(t)dt \qquad (3.6)$$

where t_1 is the temporal interval for integration.

So the problem from the experimental point of view is to find which is the minimum time interval that allows to identify with sufficient accuracy the true mean velocity of the flow, calculated as average of a finite number of velocity vectors. This time interval, necessary to obtain a correct measurement, depends on the time scale of the turbulence for the specific problem, and cannot be

known “a priori”. For this reason, it is difficult to find the right duration for the velocity acquisition, which can be identified only after a lot of experiments, as a compromise between the accuracy of the measurements and the time duration of the acquisition. In the experiments object of this thesis, a measurement time interval of 80 seconds has been chosen for every grid positioning, in order to achieve a compromise between measurement accuracy and the time utilized for the experiment.

In order to assess if the measurement time utilized in the experiments (about 80 sec for every map) is sufficient to obtain a stable mean velocity, the average velocity was calculated separately on two different subsets, for several measurement points placed in different zones of the reservoir (in low velocity zones and in high velocity zones, both), obtaining two partial average values V_1 and V_2.

Then, an index e that identifies the shifting between the two average values, normalized to the largest of the two average values has been developed:

$$\boldsymbol{e} = \frac{\boldsymbol{V}_1 - \boldsymbol{V}_2}{\max(\boldsymbol{V}_1, \boldsymbol{V}_2)} \qquad (3.7)$$

Further details on this subject can be found in the master thesis of Carrara and Gervasoni (2010).

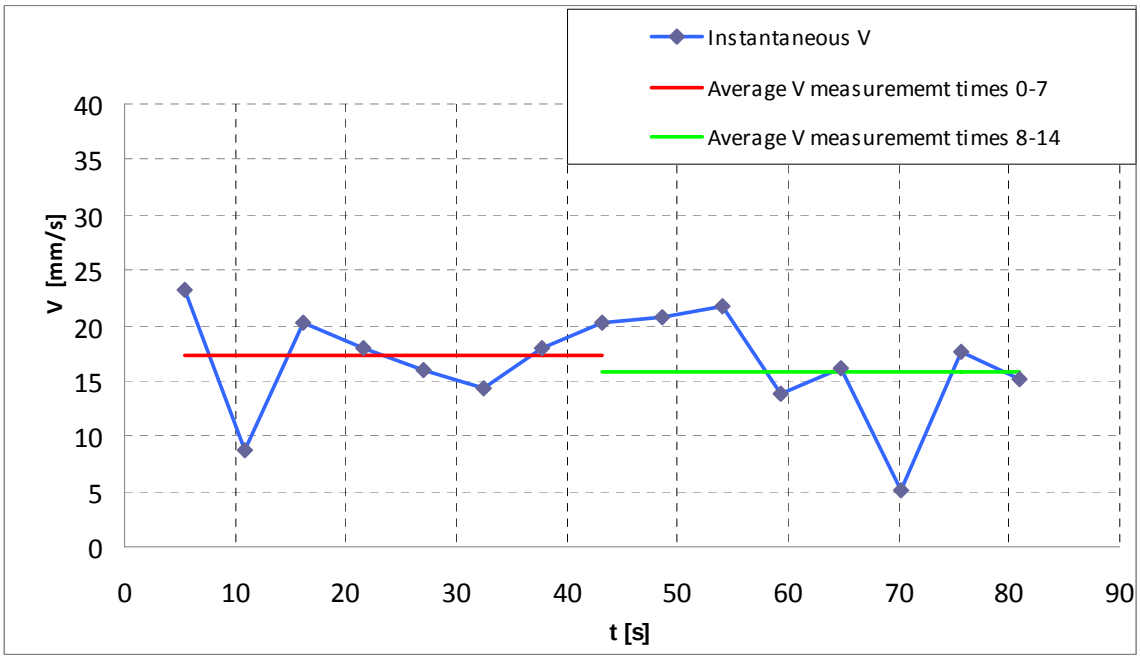

Figure 3. 9– Example of the analysis on the stability of the average value for one reservoir position in the reservoir 6x4 m (e = 0.08)

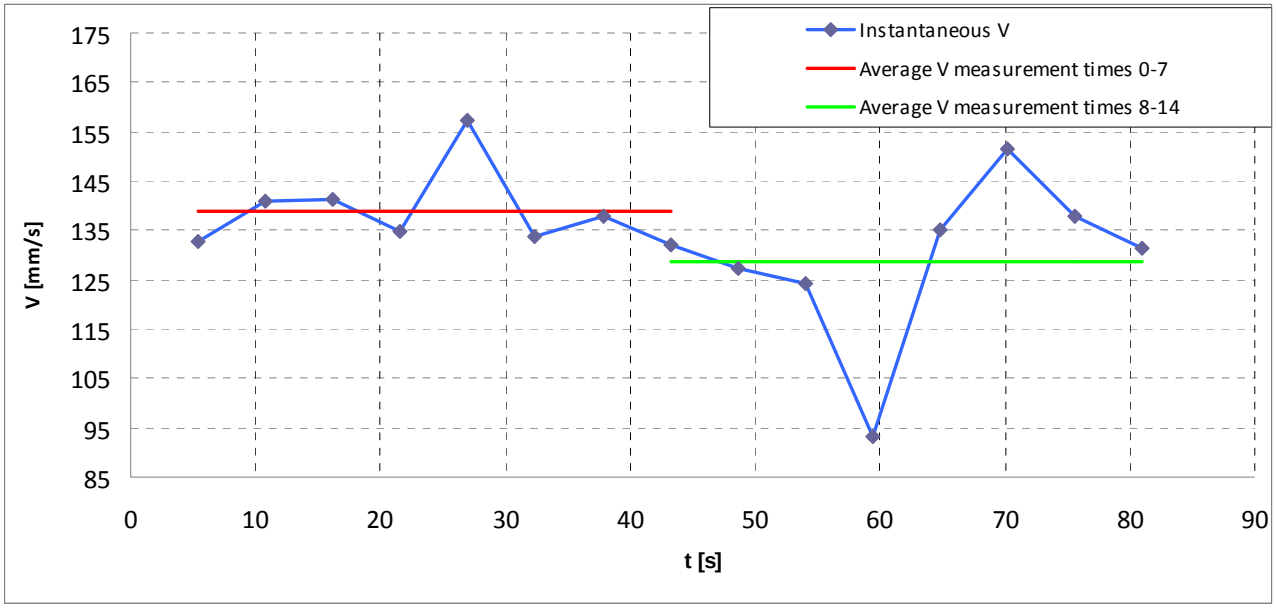

Figure 3. 10- Example of the analysis on the stability of the average value for one reservoir position in the reservoir 3x4 m (*e* = 0.06)

If this index has low values, it means that the two partial average values are near, and for this reason also the overall mean is near to the value identified by the two partial averages. For example, for the cases referred in Figure 3. 9 and Figure 3. 10, the deviation between V_1 and V_2 is equal to the 6% and to the 8% of velocity; so, for the purpose of this thesis, the recorded average value can be considered sufficiently stable in time, and the time interval adopted can be considered adequate to calculate a nearly time independent average velocity. Anyway, for future studies, more attention should be paid in order to have completely stable first order statistics, in the way to depict more accurately the true mean velocity field.

Furthermore, it has to be remembered that the calculated *V'* hides in itself, besides the real physical turbulent fluctuation, also the instrumental measurement error of the transducer. In particular, when velocities are very small, as in the re-circulation zones, the influence of the measurement error of the UVP transducers could become not negligible. In fact, according to the constructor, the global error of UVP measurement is < 5%. Anyway the velocity resolution in this case is 1.4 mm/s, because it is 1/127 of the maximum selected velocity (in this case, 0.18m/s).

Analysis of velocity profiles V(z) and of vertical velocity component w(z)

Local UVP measurements were performed also in order to investigate:

1) the horizontal $V(z) = \sqrt{u(z)^2 + v(z)^2}$ velocity at different height z from the bottom of the reservoir;

2) the vertical velocity component *w(z).*

1) A preliminary investigation of the 2D horizontal velocity at different height *z* from the bottom of the reservoir (*z* = 0.01 – 0.06 – 0.11 – 0.18 m) was carried out, in several points of the reservoir. The horizontal velocity intensity *V* was obtained by compositions of the 2 horizontal velocity components *u* and *v* measured by the UVP transducers: $V(z)=\sqrt{u(z)^2 + v(z)^2}$. The aim was to define the average shape of the vertical velocity profile as a function of the distance *z* from reservoir bottom, and to choose the height at which the transducers must be placed for the following depth-averaged measurements. Since the resulting average velocity profile matches well with a logarithmic one, it was decided to put the UVP transducers at a height *z* = 0.08 m (0.4*h*) to perform the following velocity measurements, since the measured velocity at that height can be considered as representative of the average velocity in the vertical direction *V* (Graf and Altinakar, 2008), whose formulation is given by:

$$V = \frac{1}{h} \cdot \int_0^h V(z)dz = V(0.4) \qquad (3.8)$$

The experimental average velocity profile along water depth *V(z)*, normalized to the depth-averaged theoretic plug flow velocity *Q/(Bh)*, is represented in Figure 3. 11, together with the fitted logarithmic profile:

$$\frac{V(z)}{U^*} = \frac{1}{K} \cdot \ln\left(\frac{z}{z_0}\right) \qquad (3.9)$$

where U^* is the friction velocity (0.005 m/s) and z_0 is a reference height from the bottom (0.001 m). Both these quantities have been evaluated by fitting the experimental data, while K is the Von Karman constant (0.4) and z is the coordinate indicating the vertical direction.

As far as concern the friction velocity, its definition is: $U^*=\sqrt{\frac{\tau_w}{\rho}}$, where τ_w is the wall tangential stress and ρ is the density of the water.

Accuracy bands, represented by the standard deviation from the average, are also represented in Figure 3. 11, showing the variability of velocity. As it can be seen, the variability of velocity for the different measurement points is quite high, because the magnitude of velocity is very different from a zone to another of the reservoir, but in any case the general shape of the average profile is well represented by the logarithmic interpolation.

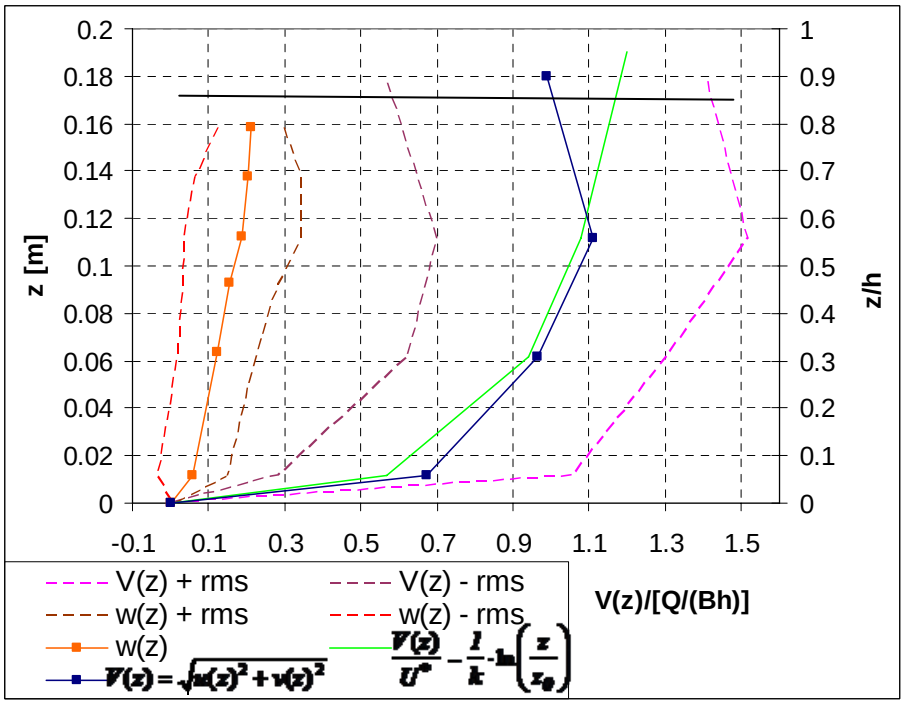

Figure 3. 11 – a) Average vertical velocity profile *V(z)* and its variability, represented by the standard deviation (rms). b)Average vertical velocity component *w(z)* across water depth (*h* = 0.2 m) and its variability, represented by the standard deviation (rms). c) Logarithmic velocity profile fitting experimental points. d) Horizontal line indicating the maximum depth under the water table at which UVP measurements are valid.

It can be noted from Figure 3. 11 that the measurement point closest to the water surface, presents an evident decrease of velocity, not in agreement with the logarithmic profile. Even if a decrease of

velocity near the surface could be physically explained by the "dip" phenomenon (Absi, 2011, among others), in this case the recorded velocity decay is more likely due to the utilized measurement technique. Indeed, the amplitude of the signal emitted by the UVP transducer increases as it goes further from the transducer, forming the so-called measurement cone. The velocity measurement is an average of the velocity of the points at the basis of this cone. So, if the transducer is placed too close to the water surface, the measurement cone goes partially out of the water and the resulting velocity measurement is not representative of the actual flow velocity. In particular, the divergence angle of the measurement cone for the utilized transducers is about 3°, so the transducer must be placed at a minimum distance of 0.036 m under the water table, as indicated by the horizontal line in Figure 3. 11, in the way that the acoustic signal doesn't go out of the water.

2) UVP measurements of the vertical velocity component *w(z)* were carried out as well, in order to confirm the assumption of a negligible vertical velocity component with respect to the horizontal ones, hypothesis that is at the basis of the application of the shallow waters theory. A transducer was placed perpendicular to the water surface, in the way that it could measure the complete profile of the velocity component *w(z)* along the water depth. The values of the average *w(z)* profile, obtained from several measurements points in different locations of the reservoir, are shown in Figure 3. 11. The ratio between the vertical component and the horizontal velocity is on average 10 %. For this reason, the measurement of horizontal velocity components is adequate, as a first approximation, to depict the main characteristics of the velocity field in the reservoir, in particular the large scale horizontal flow structures having a vertical axis, which contain the main portion of energy content.

Anyway, the presence of a small vertical velocity means that the flow is not really two dimensional, so a more accurate description of the flow field should be three-dimensional, since actually also smaller eddies having an horizontal axis are present in the reservoir, as assessed for example by the experiments of Abbott and Kline (1962). However, it is known that the largest turbulent structure (associated to long wavelengths, of the order of the geometrical length scale *L*)

contain the biggest part of the kinetic energy (Versteeg and Malalasekera, 1995), and that it exists an energy cascade which "moves" kinetic energy from the large scale to the smaller ones, until it is dissipated by the viscous forces. Anyway, since the aim of this thesis is to investigate the typology of largest coherent turbulent structures, which are the ones depending on the geometrical boundary conditions of the problem, the investigation of the only horizontal velocity components can be considered adequate to the purpose.

Moreover, it has to be underlined that the results presented in Figure 3. 11 are average values obtained on a quite large sample; so, it may be that for some singular measurement point the vertical component is not really negligible with respect to the horizontal ones, since the horizontal velocities in the reservoir vary in quite a wide range (3 - 140 mm/s). Also the shape of the horizontal velocity profile along water depth could be quite different from the mean logarithmic profile in some measurement points, due to local particular conditions.

For this reason, a more detailed investigation of both the vertical velocity component and of the 2D horizontal flow field at different heights from the bottom could be interesting in a future, even if it would be very expensive in terms of data acquisition time.

3.3.3 Sediment concentration measurements by turbidimeters

Sediment concentration was monitored during the whole duration of tests with sediments supplying by two turbidimeters. These instruments (HACH SOLITAX sc100) measure in continuous (at time steps of 5 sec) the turbidity of the water, expressed in *NTU* (number of turbidity units). Then, a calibration curve allows to convert the optical measurement of turbidity into the corresponding sediment concentration.

The calibration curve for the used instruments is:

$$C = 0.0037 \cdot NTU + 0.0557 \quad (3.10)$$

where:

C [g/l] = suspended solids concentration;

NTU = number of turbidity units.

Tests were performed in order to check if some parameter such as the environmental light, the turbulence of the water or the proximity of the walls influenced the formulation of the calibration line, but no significant influence was found, confirming the validity of the calibration line here referred.

One turbidimeter was placed on the inlet channel, measuring the inlet sediment concentration C_{in}, while the other was placed on the outlet channel (Figure 3. 12), measuring the outlet sediment concentration C_{out}; both the instruments were linked to a data logger (Figure 3. 13) to store the acquired information. Then, the quantity of sediments being trapped in the reservoir could be determined by difference between the inflowing and outflowing sediment volumes, and the reservoir trapping efficiency TE_1 concerning the experiment could be determined in this way:

$$TE_1 = \frac{\int_0^t C_{in}(t) \cdot Q dt - \int_0^t C_{out}(t) \cdot Q dt}{\int_0^t C_{in}(t) \cdot Q dt} = \frac{\overline{C_{in}} - \overline{C_{out}}}{\overline{C_{in}}} \qquad (3.11)$$

where $\overline{C_{in}}$ and $\overline{C_{out}}$ are the average concentrations of inflowing and out-flowing suspended solids.

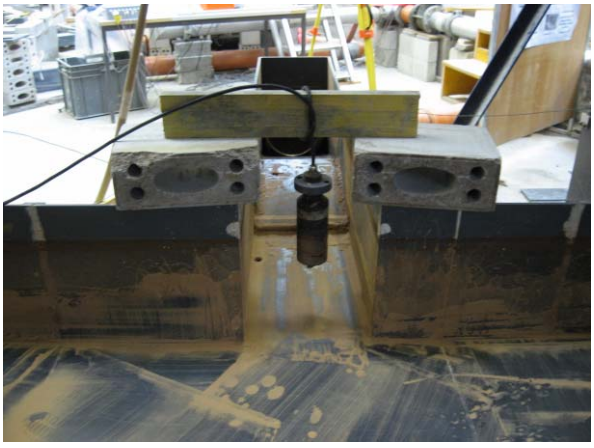

Figure 3. 12– Turbidimeter placed on the outlet channel

Figure 3. 13 – SOLITAX turbidimeter data logger

As it can be seen in Figure 3. 14, turbidity measurements are subjected to peaks, due to the non constant sediment discharge coming from the mixing tank but also to the fact that the optical measurement performed by turbidimeters is strictly local.

Nevertheless, the average sediments concentration resulting from the measurement of the turbidimeter placed on the inlet channel is about 2 g/l or, in other words, 14 g/s; this value corresponds to the value that can be obtained considering that the experiment consisted in 200 kg of sediments supplying in 4 hours, conveyed to the reservoir by a discharge of 7 l/s.

The value of the inflowing and outflowing sediment concentration was also checked by sampling of water during the experiment. The samples were weighted, dried in an oven at low temperature, and then weighted again, in order to determinate the quantity of sediments present in the sample.

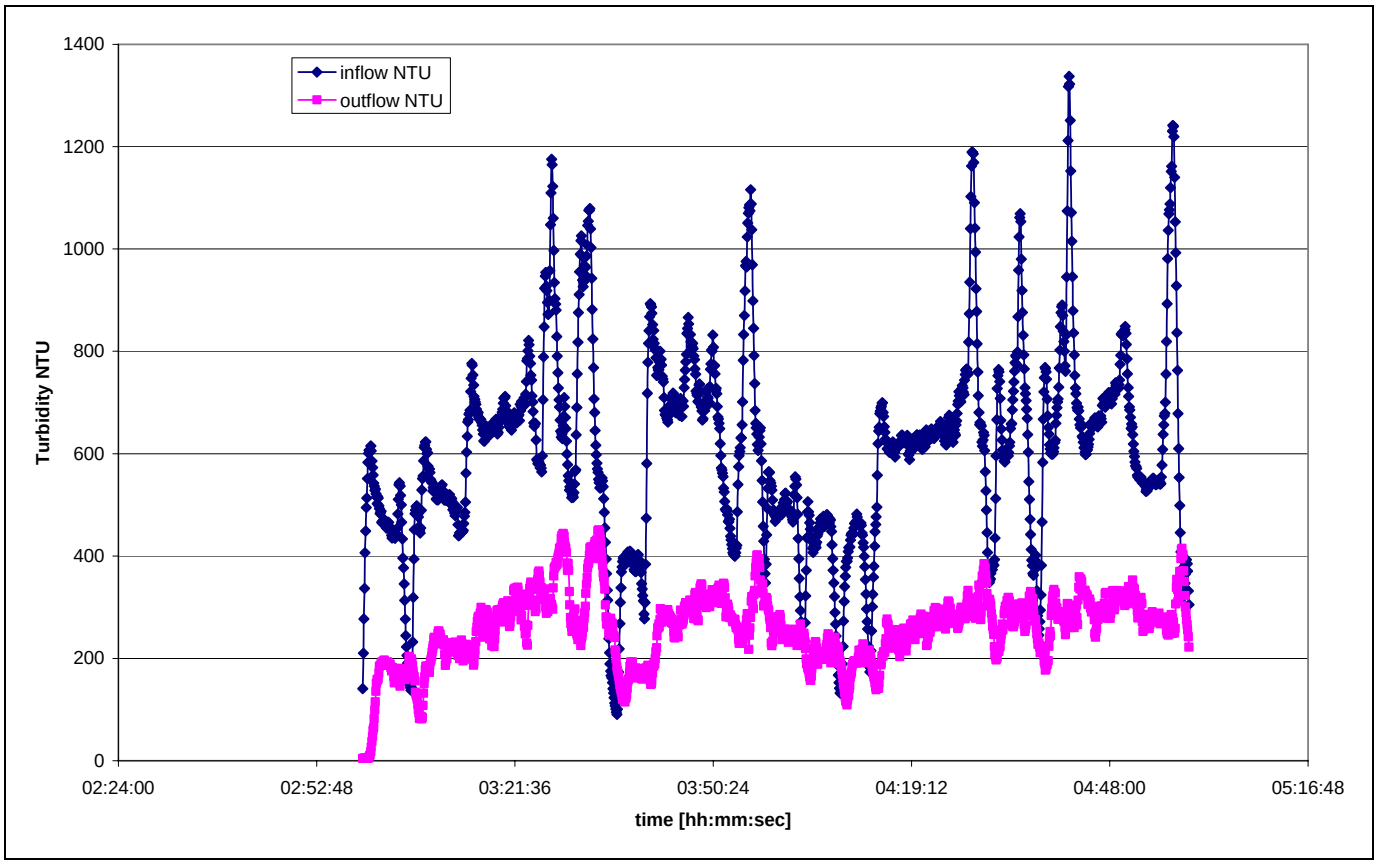

Figure 3. 14 – Example of a turbidity measurement for a 2 hours test

3.3.4 Sediment deposits thickness measurements by laser

In order to obtain the maps representing the sediments distribution on the whole reservoir bottom after 2 hours and 4 hours of sediments supplying, sediments thickness was measured by a laser method.

The laser (Baumer, OADM13) was placed in a water-proof box fixed on a movable metallic bar (Figure 3. 15), at a known height from the bottom of the reservoir. Then, by the characteristic calibration line of the laser, the voltage given in output by the laser could be linked to the distance of the laser light source from the top of the sediments deposits, and consequently the thickness of sediments deposits could be known:

$$D = 0.05 \cdot S - 0.0301 \qquad (3.12)$$

where:

D [mm] = distance between the laser light source and the top of sediments deposits or the bottom surface of the reservoir, when it is clean;

S [V] = output of the laser (voltage) recorded on the computer by a purpose made Labview software for data acquisition.

The calibration equation was obtained for the laser in the real operating conditions, that is to say with the laser light crossing the glass on the bottom of the water-proof box and the water depth in the reservoir.

The measurements of sediments thickness were performed on the whole reservoir bottom according to the points of a regular grid, in the way to obtain a sufficient spatial resolution of the measurements: a basic grid formed by squares of 50x50 cm was used, but further measurement points were taken for example along the axis of the inlet and of the outlet channel, in order to have a more detailed information in these zones.

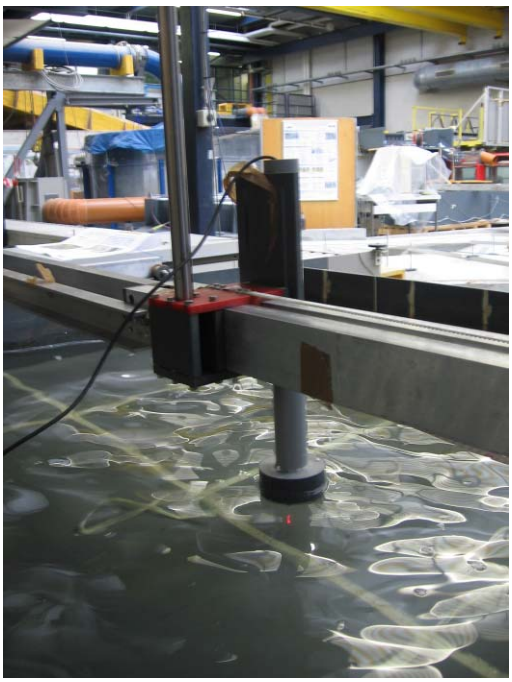

Figure 3. 15 – Laser light installed on the metal bar over the reservoir

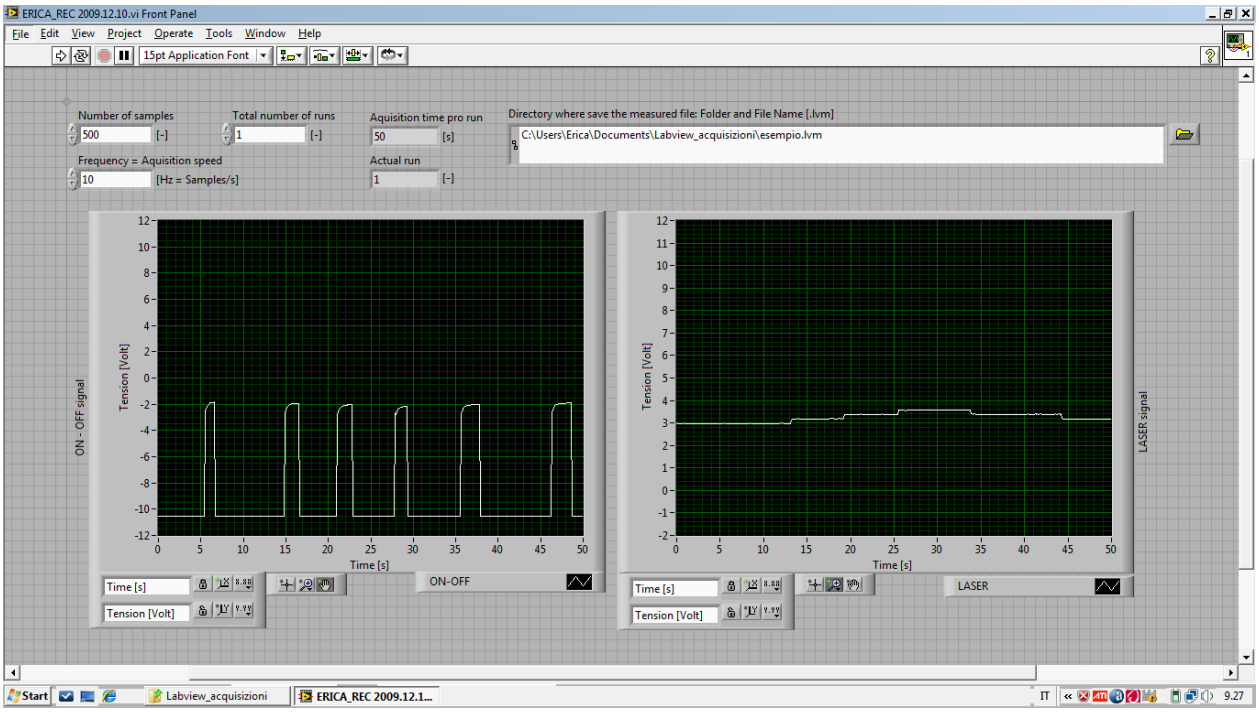

Figure 3. 16 – Interface of the Labview software for laser data acquisition

Actually, it must be underlined that the signal coming from the laser was a current intensity, but it was converted into a voltage signal by a current intensity – voltage converter; then it was sent to the PC by a USB high-speed data acquisition module (DAQ - National Instrument NI-USB6259). The signal trend in time was shown by the graphical interface (Figure 3. 16) of a purpose made Labview program (.vls), which acquired, displayed and stored the data.

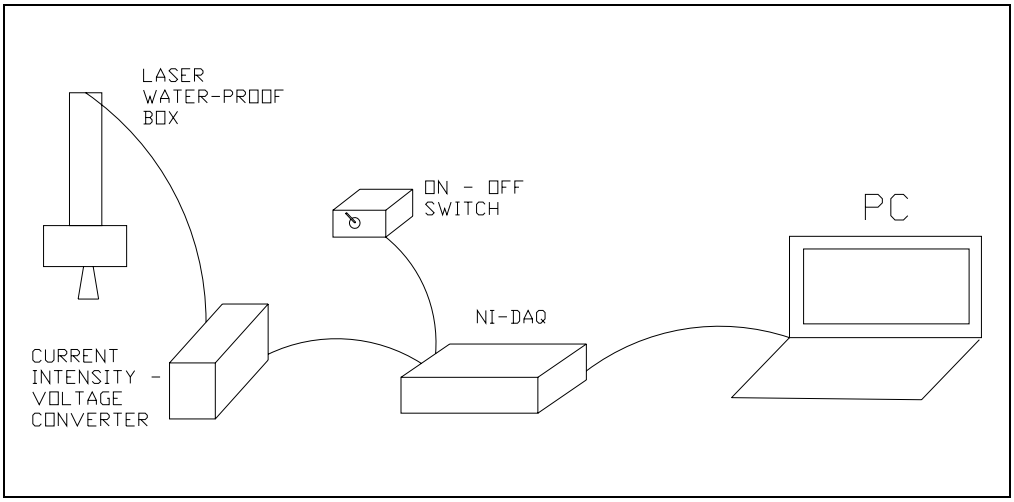

Figure 3. 17 – Schema of the laser measurement set-up

Since the measurement performed by the laser is continuous, an other signal was recorded simultaneously to the laser voltage on the Labview software in order to associate the voltage to the specific measurement point in the reservoir. This signal was produced by a switch on-off which was activated in correspondence of the desired measurement point; then, the switch was turned off and the laser was moved by the movable bar towards the next measurement point. The on-off signal coming from the switch was sent simultaneously with the laser measurements to the National Instrument data acquisition module, and then to the PC. In the end, only the voltage recorded by the laser in correspondence of the on-signal of the switch were considered as representative of the sediments thickness at the current measurement point.

3.4. Tests procedures

3.4.1 Clear water tests

The aim of clear water tests was to define the types of flow field developing in different geometrical configurations of the reservoir, by the realization of 2D velocity maps. The velocity flow field was measured by LSPIV and UVP, according to the following procedure: firstly, the pump was started, then the valve on the feeding pipe was opened, the reservoir was filled up with clear water and the water depth was regulated at the desired level by a flap gate placed on the outlet channel, till the steady state was achieved. The achievement of the steady state corresponding to the wanted circulating discharge was monitored in three ways: first, by the reading of the electromagnetic flow meter discharge value, shown on the laboratory control panel; furthermore, the water discharge was checked by reading the water level above the crest of the flap gate and applying a level-discharge relationship for thin and inclined weirs.

Moreover, since the desired circulating discharge corresponded to a definite level in the mixing tank, also the steadiness of this water level was checked.

The hydraulic parameters, kept constant for all the experiments, are shown in Table 3. 3.

Table 3. 3– Hydraulic parameters used in the experiments

Q [l/s] =	7
h [m] =	0.2
R_{in} =	112000 (turbulent flow)
F_{in} =	0.1
h/b =	0.8

The hydraulic conditions of the experiments can be synthesized by two non-dimensional parameter:

- R_{in} is the Reynolds number referred to the inlet channel:

$$R_{in} = \frac{4 \cdot V_{in} \cdot h}{\nu} \qquad (3.13)$$

where:

V_{in} = mean inlet velocity;

h =water height ;

ν = cinematic viscosity of water.

- F_{in} is Froude number referred to the inlet channel:

$$F_{in} = \frac{V_{in}}{\sqrt{g \cdot h}} \qquad (3.14)$$

g = acceleration of gravity.

3.4.2 Tests with sediment supply

The tests with sediments supplying concerned asymmetric reservoir configurations, that were obtained moving the inlet and the outlet channels respectively along the upstream and the downstream side of the reservoir. The configurations chosen for the tests of the present thesis are shown in Figure 3. 18 and they have the following characteristics:

a) C – C: this is the basic reference symmetric configuration, having both the inlet and the outlet channel at the middle of the upstream and of the downstream reservoir edge;

b) L – L: this configuration has both the inlet and the channel placed near the (hydraulically) left side of the reservoir. In particular, the upstream channel has the axis placed at a distance of 110.5 cm from the reservoir left side, while the outlet channel has the axis placed at a distance of 77 cm from the reservoir left side;

c) L – R: this configuration has the inlet channel placed near the left side of the reservoir (110.5 cm far), while the outlet channel is placed near the opposite corner, having the axis at a distance of 77 cm from the right wall;

d) C – R: this configuration has an asymmetry less pronounced than the c) configuration, since in this case the inlet channel is placed at the middle of the upstream edge, while the outlet channel is at the corner of the downstream side, having the axis at a distance of 77 cm from the right wall.

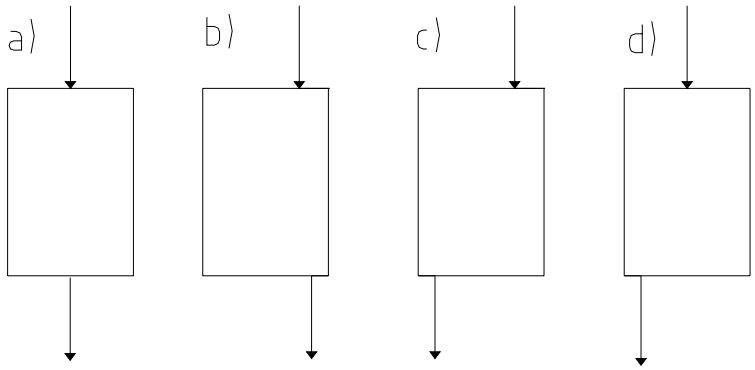

Figure 3. 18– Tested asymmetric reservoir configurations a) C-C b) L-L c) L-R d) C-R

For the tests with sediments supplying, reservoir width was set to B = 4 m and reservoir length to L = 4.5 m (L/B = 1.125, B/b = 16). Under these conditions, the C-C geometric configuration is characterized by a stable symmetric flow field S1 (as defined in chapter 4), with a central main jet that goes straight from the inlet to the outlet and two recirculation zones at each side of the jet.

The aim of the tests performed with an asymmetric location of the inlet and of the outlet channel was to analyze the effect that this asymmetry produce on the flow pattern and consequently on the localization and on the amount of sediments deposits on the bottom of the reservoir.

These tests were performed with the same hydraulic conditions used for clear water tests, that is to say Q = 7 l/s and h = 0.2 m while, about the sediment supplying, a mean inflowing solid discharge of about 14 g/s was guaranteed, corresponding to a concentration of about 2 g/l.

Finely crushed walnut shells were used as suspended sediments in the experiments. The solid particle density is ρ_s = 1460 kg/m^3, determined by pyknometry (in collaboration with the Infrastructure Laboratory of Politecnico of Milano); the average diameter is $\overline{d}$ = 112 μm, the median diameter is d_{50} = 89 μm, and the coefficient of uniformity U is d_{60}/d_{10} = 4. The cumulative grain size distribution of the material, obtained by a laser particle-size analysis performed in the framework of this thesis at EPFL, is shown in Figure 3. 19, together with the estimated settling velocity v_{ss} corresponding to each diameter. Table 3. 4 summarizes the characteristics of the grain size distribution.

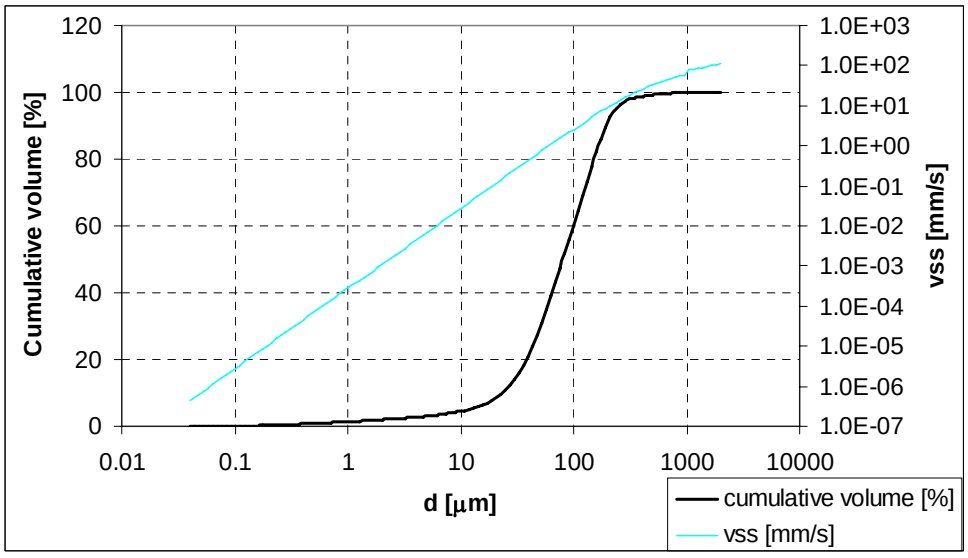

Figure 3. 19 – Cumulative grain size distribution by volume and settling velocity of the crushed walnut shells

Table 3. 4 – Characteristic size and respective settling velocities for the crushed walnut shells at T = 20°C

		v_{ss} [mm/s]
d_m [μm] =	112	3.1
d_{mode} [μm] =	140	4.9
d_{10} [μm] =	25	0.2
d_{25} [μm] =	49	0.6
d_{50} [μm] =	89	2.0
d_{75} [μm] =	152	5.8
d_{90} [μm] =	215	11.6
$U = d_{60}/d_{10}$ =	4	

Stokes' velocity for spherical grains was assumed as a valid first approximation of the effective settling velocity for particles having a diameter up to 100 μm. Since the material is not mono-granular, a specific Stokes settling velocity has been calculated for every class of diameters:

$$v_{ss} = \frac{g \cdot (\rho_s - \rho) \cdot d^2}{18 \cdot \mu} \qquad (3.15)$$

where:

g = gravity acceleration (m/s^2);

ρ_s = density of the solid particle (kg/m^3);

ρ = water density (kg/m^3);

d = particle diameter (m);

μ = dynamic viscosity of water (Pa·s).

It must be remembered that the Stokes law is strictly valid only for the sedimentation of a spherical particle in still water, while in the case of a particle settling in a turbulent flow, turbulent forces can influence the settling velocity (Wand and Maxey, 1993). Moreover, in order to take into consideration the influence of the real shape of the particle on settling velocity, a shape factor should be applied (P. K. Swamee and C. S. P. Ojha, 1991). So, the calculated Stokes velocity must be considered only as a reference velocity, giving the order of magnitude of the phenomenon, and not the effective settling velocity of the real non-spherical particle in a turbulent flow.

For particles larger than 100 μm the effect due to the non-spherical shape may become relevant, so other empirical formulations for the estimation of settling velocity were applied, as detailed in Van Rijn (1993). Here, the formulation concerning sediment diameters 100< d <1000 μm, used in the present case, is referred:

$$v_{ss} = \frac{10 \cdot \nu}{d} \cdot \left[\left(1 + \frac{0.01 \cdot \left(\frac{\rho_s}{\rho} - 1 \right) \cdot g \cdot d^3}{\nu^2} \right)^{0.5} - 1 \right] \qquad (3.16)$$

The main part of the sediments size fractions (about the 75% of the grain size distribution) can be carried by the flow as suspended load, since, according to Bagnold (1966), the ratio between friction velocity U^* and settling velocity v_{ss} is greater than 1.

Particles were mixed mechanically to the water in the supplying tank, then they were brought to the inlet channel by a pressurized pipe. Thus, when they entered the reservoir, they formed a suspension fully mixed with water. Nevertheless, the transport capacity of the flow is very low.

Suspended solid transport capacity for the inlet channel was calculated on the basis of the different size fractions, by applying the method of Celik and Rodi (1991). According to these authors the transport capacity C_T is given by the following formulation:

$$C_T = \beta \cdot \frac{\tau_w}{(\rho_s - \rho) \cdot g \cdot h} \cdot \frac{V}{v_{ss}} \qquad (3.17)$$

where β is an empirical coefficient (value suggested by Celik and Rodi: β = 0.034), V is the velocity of the flow, τ_w is the wall friction $\tau_w = 0.5 \cdot c_f \cdot \rho \cdot V^2$, in which c_f is the drag coefficient.

The calculated total suspended solid transport capacity is one order of magnitude lower than the inflowing solid discharge Q_s = 14 g/s. For this reason, the sediments start to settle already in the inlet channel and then, of course, in all the remaining part of the reservoir, without significant phenomena of re-suspension, due to the very low velocities.

The tests with sediments supplying were performed according to the following procedure:

- The pump was started, the valve on the feeding pipe was opened, the reservoir was filled up with clear water and the water depth was regulated at the desired level by the flap gate placed on the outlet channel, till the steady state was achieved. The achievement of the steady state corresponding to the wanted circulating discharge was monitored in three ways: first, by reading the electromagnetic flow meter discharge value; then, by reading the water level above the crest of the flap gate and applying a level-discharge relationship for thin and inclined weirs. Moreover, since the desired circulating discharge corresponded to a definite level in the mixing tank, the steadiness of this water level was checked.
- The turbidimeters were turned on.
- The motor of the propeller in the mixing tank was started, the sediment supply tank was filled by sediments, the opening gate at the bottom of the sediments supplying tank was opened and the motor governing the vibration of the sediments supplying tank was started, in the way that sediments started to fall in the mixing tank.
- When the water-sediment mixture arrived at the inlet channel, the chronometer was started and the test began.
- The sediments supplying tank was kept filled during the experiments, in the way to assure a solid discharge of 50 kg/h, corresponding to 2 packs of walnut crushed shells every hour.
- After 2 hours of experiment, the sediments supplying and the water discharge were suddenly and simultaneously stopped and the flap gate was raised up in the way to keep the reservoir water depth at its constant height. Then, the sediments deposits thickness on the bottom of the reservoir was measured by the laser (see paragraph 3.3.4). After the measurement, the hydraulic system and the sediments supplying were started again, like described before, and the flap gate was regulated in order to maintain the water depth at the desired value.

- During the experiment, samples of the water-sediments mixture both at the inlet and at the outlet channel were taken, for a total of three sampling during the 4 hours of the experiment.
- At the end of the experiment (total duration 4 hours), after stopping the system like described before, the sediments deposits thickness on the bottom of the reservoir was measured again by the laser.

The velocity field in the reservoir was measured by LSPIV and by UVP before and after the experiment, in order to assess if the sediments deposits affect in some way the flow patterns. In fact, as it will be explained in chapter 4, sometimes the flow field corresponding to the situation of clear reservoir bottom was strongly different from the flow field developing in presence of an inflowing suspended load.

3.5. Similarity for the suspended solids

The suspended solids used in the experiments to simulate real sediments at field scale were chosen in order to respect similarity about settling velocity. In fact, as the geometric scale of the model is undistorted, the scale of the settling velocity is the same scale of flow velocity. So, we obtain the following relationship:

$$\lambda_{v_{ss}} = \frac{v_{ss_p}}{v_{ss_m}} = \lambda_V = 7.07 = \frac{\frac{g \cdot (\rho_{s_p} - \rho) \cdot d_p^{\,2}}{18 \cdot \mu}}{\frac{g \cdot (\rho_{s_m} - \rho) \cdot d_m^{\,2}}{18 \cdot \mu}} = \frac{(\rho_{s_p} - \rho) \cdot d_p^{\,2}}{(\rho_{s_m} - \rho) \cdot d_m^{\,2}} \qquad (3.18)$$

Since the parameters of the model are d_{50m} = 89 μm and ρ_{sm}= 1460 kg/mc, while the density of the sediments that are usually present in nature is ρ_{sp}= 2650 kg/mc, the only unknown in the above equation is the diameter d_{50p} of the sediments at field scale. A value d_{50p} = 0.13 mm is obtained, which is representative of a quite fine sand, that can be often carried in suspension by natural rivers, having a settling velocity v_{ssp} = 14 mm/s.

The concentration adopted in the experiments was chosen in order to maintain the same volumetric concentration of sediments that it is normally found in real cases. So, from the definition of volumetric concentration C_{vol}, we obtain the following relationship:

$$C_{vol} = \frac{C_m}{\rho_{s\,m}} = \frac{C_p}{\rho_{s\,p}} \qquad (3.19)$$

in which, given the density ρ_{sm}= 1460 kg/mc and the concentration C_m = 2 g/l of the sediments used in the experiments, and the density ρ_{sp}= 2650 kg/mc of the sediments at field scale, we can obtain the concentration of the sediments at field scale C_p = 3.6 g/l; this value corresponds, for example for the Rhone River in Switzerland, to the maximum values that can be found in flood conditions (www.bafu.admin.ch). In this case the volumetric concentration is equal to 0.14 %.

In the end, to verify that at field scale and at model scale the sediments can be conveyed as suspended load, we must verify that:

$$\frac{U*}{v_{ss}} > 0.2 - 2 \qquad (3.20)$$

This is a quite wide range in which the already cited criterion of Bagnold (1966) $U^* > v_{ss}$ is included and it is due to the very different empirical formulations which can be used to calculate the threshold for the onset of suspend transport (Chanson, 1999).

In the present case, according to the Froude similarity, U^*_p = 35 mm/s, and we obtain

$$\frac{U^*_p}{v_{ssp}} = \frac{U^*_m}{v_{ssm}} = 2.5 \qquad (3.21)$$

which corresponds certainly to a condition of suspended load transport.

CHAPTER 4

RESULTS OF THE EXPERIMENTS

In this chapter the results of the experiments on the physical model in Lausanne are presented, as far as concern the experiments with clear water and the experiments with suspended solid.

The experiments with clear water aimed to classify the flow pattern developing in a reservoir configuration as a function of the length-to-width ratio and of the expansion ratio of the reservoir, at constant hydraulic conditions. A critical comparison with the results obtained in the same field by other authors, Dufresne and Kantoush, is presented and it is shown how these results can be matched together giving a wider view on the complexity of the phenomenon.

As far as concern the experiment with a suspended solid inflow, the flow fields developing in the different asymmetric configuration (with the inlet and the outlet channels placed in different positions) are analysed both before and after the sediment inflow. The amount and the localisation of the sediments deposits on reservoir bottom are described, and the trapping efficiency of the various reservoir configurations.

All these experimental data represent a precious database for a comparison between the results of numerical simulations by CFD codes, as it has been done for example in this thesis, comparing the experimental results with the results of simulations carried out with WOLF2D (as it will be shown in the following chapter 6), in order to check the accuracy of the results provided by the numerical model or to calibrate the turbulence model implemented.

4.1. Flow pattern classification

Since the measurement of Kantoush (2008) on the same experimental facility at LCH had shown that different kind of flow fields can develop in a rectangular reservoir depending on its geometrical characteristics, and in particular that an asymmetric flow field can develop despite the symmetry of the geometry, in the present research it was decided to deepen more systematically the study of the influence of reservoir geometry on the flow field, as it will be shown by the following paragraphs.

4.1.1 Classification as a function of L/B and B/b

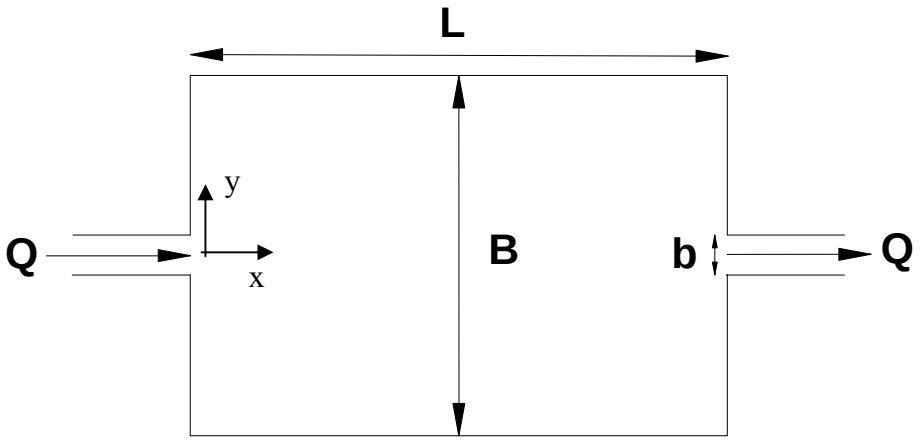

Figure 4. 1 –Schematic top view of the symmetrical reservoir configuration

The classification proposed in the framework of this thesis is based on the analysis of the combined influence on flow pattern type of 2 non dimensional geometrical parameters:

- The length-to-width ratio *L/B*, that is the ratio between reservoir length *L* and reservoir width *B*. The present research is different from past studies concerning sudden expansions, since in those cases (e.g. Abbott and Kline, 1962) the length of the downstream expanded section was infinite, while in this case the finite length of the reservoir is analyzed as it is a parameter influencing the typology of the flow field. So, the present research can be classified as a study of a sudden expansion followed by a sudden contraction, similarly to the work of Mizushima and Shiotani (2001) among others (see Chapter 2).

- The expansion ratio *B/b*, that is the ratio between reservoir width *B* and the width of the inlet channel *b* = 0.25 m which is a fixed value in the experiments here presented. As already said in chapter 2, a lot of research was carried out analyzing the influence of this parameter combined with the length-to width ratio and the Reynolds number on the onset of asymmetry in the flow field (e.g. Cherdron et al., 1978, among others), but the main part of these studies concerned pressurized conduits and laminar regimes, while the present case is a free-surface turbulent flow.

The classifications of the flow patterns developing in the reservoir for the 41 tests carried out by LSPIV and by UVP are shown in Figure 4. 2 as a function of L/B and B/b. The configurations tested by Dufresne et al. (2010a) for the same test conditions, and by Kantoush (2008) in the same LCH facility, are also included. Note that the additional data provided in the present work give a more complete view of the geometrical effect on flow patterns, because Kantoush's tests concerned only 8 configurations, with a fixed values of length (L = 6 m) and a varying width B = 0.5÷4 m, or a fixed width (B = 4 m) and a varying length L = 3÷6 m. In contrast, the present tests cover the entire range of combinations of reservoir widths and lengths feasible at the LCH facility, allowing to analyse the combined effects of L/B and B/b on the flow pattern. Figure 4. 2 can be divided into three main zones, corresponding to different flow patterns:

- *Channel-like flow* (CH-L), characterized by the smallest range of expansion ratios (maximum B/b = 2, corresponding to B = 0.5 m), independent from reservoir length L. This flow field has no large recirculation zones, except for two small eddies on both sides of the inflow jet. The flow field across most of the reservoir is one-dimensional, characterized by a constant velocity profile. This type of flow field was observed also by Abbott and Kline (1962), who found that an asymmetrical flow pattern develops if $B/b > 2.67$. However, their tests were such that the length L of the expanded reservoir portion could be considered infinite with respect to the expansion width B, so that the effect of the length-to-width ratio had not been analysed.

- *Symmetric flow* (S0 and S1) generated for sufficiently small L/B. The critical threshold L/B value below which a stable symmetric flow field develops is a function of B/b: in particular, the critical L/B value decreases with the increase of B/b. The threshold is identified in Figure 4. 2 by the dashed line corresponding to the critical non-dimensional shape parameter $T = L/[(B-b)^{0.6} \cdot b^{0.4}] = 4.09$ defined by Dufresne et al. (2010a). The T parameter validity was confirmed by the present tests (Figure 4. 2). Within the symmetric flow region, two subsets are identified, namely the two-eddies flow field S0, which develops if $L/B \leq 1$, and the four-eddies flow field S1, which develops otherwise. The symmetric flow fields S0 and S1 are characterized by a main jet traversing straight from the inlet to the outlet along the reservoir axis and by the presence of eddies placed symmetrically with respect to the main jet. For the S0 flow field, only one eddy at both sides of the main jet develops, occupying the entire reservoir length, while the S1 flow field is characterized by two eddies on each side of the main jet. In this case, the two upstream eddies, which are smaller and slower than the two downstream eddies, can be classified as stagnation zones.
- *Asymmetric flow* (A1 and A2), characterized by $B/b > 2$, and $T > 4.48$. Two types A1 and A2 of asymmetric flow patterns were observed. For both, the main jet is deflected towards one of the lateral reservoir sides, where it attaches to the wall. Further downstream, the jet flows along the wall to the outlet channel. This particular formation of an asymmetric flow field in a symmetric geometry is attributed to the 'Coanda effect' (Wille and Fernholz, 1965; Shapira and Degani, 1990). The main characteristic of flow field A1 is a large eddy occupying the main reservoir portion, with two smaller eddies in the upstream separated region. In contrast, for the A2 flow field, the large eddy does not span over the entire reservoir length and its downstream portion exhibits a channel-like flow. Dufresne et al. (2010a) also observed the A2 flow pattern under the same hydraulic conditions, as indicated in Figure 4. 2. Herein, flow field A2 was observed for narrow ($2 < B/b < 4$) and long ($L/B > 6$) reservoirs. However, the tests performed up to now in the framework of this thesis did not include configurations with $2 < B/b < 4$ and $L/B < 6$.

Therefore, additional experimental data would be required to identify the conditions necessary for the existence of this flow field and to define a criterion for the transition from the A1 to the A2 flow field. For the moment, the separation line between the A1 and A2 flow patterns in Figure 4. 2 should be considered only as a preliminary approximation. As it will be explained later, thanks to the performed numerical simulations, it has been possible to hypothesize a more definite shape for this separation line, which will be presented in chapter 6.

Furthermore, two reservoir configurations of 'unstable behaviour' were detected. For these configurations, some tests indicated a symmetrical flow field S1, while others, carried out under identical test conditions, were characterized by the asymmetric flow pattern A1. These configurations are included in the instability zone of transition between the symmetric flow-field region and the asymmetric flow-field region, which is defined by the two critical values of the non-dimensional shape parameter $T = 4.09$ and $T = 4.48$, as proposed by Dufresne et al. (2010a). The flow in this transitional zone is sensitive to external perturbations (Dewals et al. 2008) and results from the phenomenon of bifurcation (Shapira *et al.* 1990): two solutions of the Navier-Stokes equations exist, one corresponding to the symmetric, while the other to the asymmetric flow field. Outside of this instability region the flow pattern is stable, in the sense that the type of flow field is not sensitive to external disturbances.

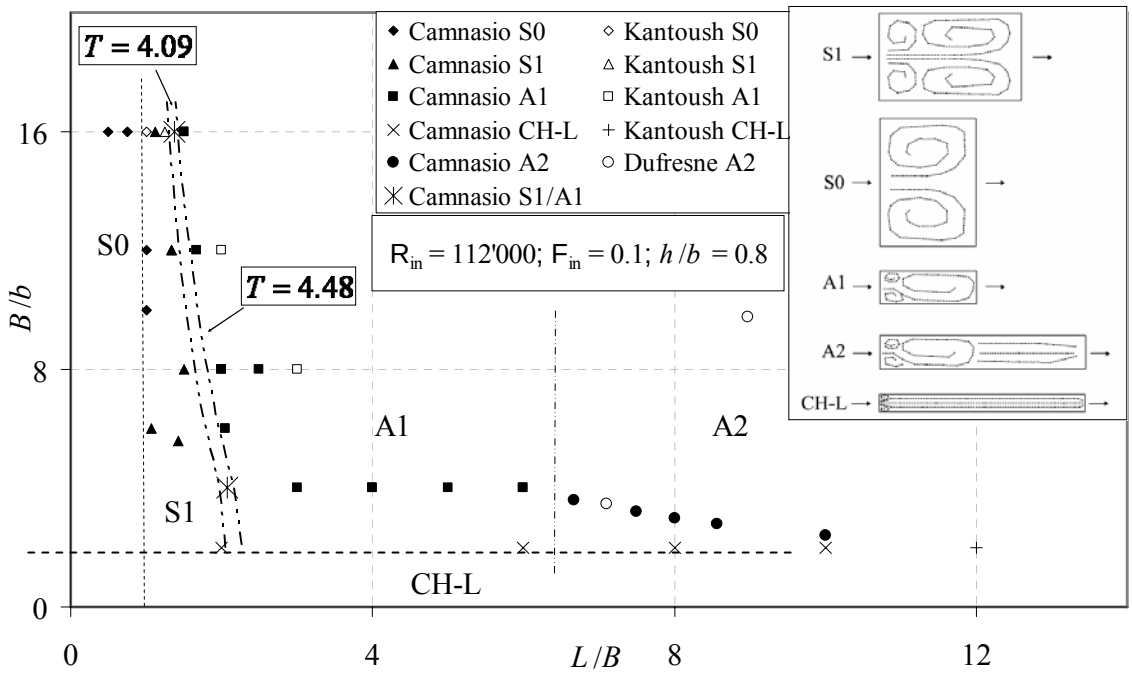

Figure 4. 2 - Classification of symmetrical (S0 and S1), asymmetrical (A1 and A2), unstable (A1/S1) and channel-like (CH-L) flow patterns resulting from EPFL tests by Kantoush (2008) and Camnasio (present study), and from Dufresne *et al.* (2010a) under identical test conditions for R_{in} = 112,000, F_{in} = 0.10 and h/b = 0.8

Maps of the average velocity vectors were produced for all the observed types of flow patterns (an example of the produced velocity maps is given in Figure 4. 3). The time- and depth-averaged local horizontal velocity $V = (u^2+v^2)^{1/2}$, calculated by interpolation of the UVP data, has been normalized by the theoretical reservoir (subscript res) plug-flow velocity $V_{res} = Q/(Bh)$, obtaining the non-dimensional (subscript nd) velocity $V_{nd} = V/V_{res}$. About V_{res}, it is a reference velocity used for normalization and it represents the theoretical mean velocity in the reservoir in the basic hypothesis of a one dimensional motion of the water across the entire reservoir cross section.

At the reservoir inlet, the inflow jet has an average velocity V_{in} = 0.14 m/s equal to that of the inlet channel. For asymmetric flow fields, the velocity of the main jet decreases rapidly as it moves along the reservoir and spreads out (Figure 4. 3a), reaching values of ~80 mm/s in the downstream part of the main jet. In contrast, for symmetric flow fields, especially for S0 flow (Figure 4. 3c), the jet diffusion is smaller, and the velocity remains nearly constant and high (~120 mm/s) along the main jet, with high velocity gradients between the main jet and the recirculation zones.

For all cases, the recirculation core is characterized by velocities of the order of ~10 mm/s. For flow fields A1, S0 and S1, the velocities are near to the theoretical average velocity V_{res} ($V_{nd} \approx 1$) in the core of the eddies, while velocities are more than ten times higher than V_{res} along the main jet. However, an approximately uniform velocity distribution over the entire cross-section (i.e. a plug-flow condition) results for the A2 flow pattern (Figure 4. 3d), beyond an initial asymmetry of the main jet at the reservoir entrance.

It is concluded that a stable symmetric flow field exists only for sufficiently short reservoirs ($L/B <$ 1.5÷2, depending on B/b, according to the critical threshold of the shape parameter). For a fixed reservoir width, the flow field changes from asymmetrical A1 to symmetrical S1 and then to S0 as the reservoir length is reduced. In other words, a reservoir length reduction leads the flow pattern towards symmetry. The flow field symmetry is also influenced by the proximity of the lateral walls to the main jet: for a reservoir length characterized by symmetric flow fields S1 or S0 at large reservoir width, it changes from symmetric to asymmetric A1 as the reservoir is narrowed. Moving the lateral walls closer to the main jet has thus a destabilising effect on the flow field, in agreement with the Coanda effect (Chiang et al. 2000, Sobey and Drazin 1986, Wille and Fernholz 1965). If the reservoir is narrowed, the symmetric flow pattern becomes first unstable and then definitely asymmetric. A lateral wall proximity therefore can prevail the stabilizing effect due to the closeness of the outlet to the inlet, which would favour flow pattern symmetry. If the reduction of reservoir width is taken to extremes, the flow field regains symmetry (A2 flow field and then channel-like flow) but now the reservoir flow tends to one-dimensional channel flow, with uniform cross-sectional velocity distribution and without large recirculation zones.

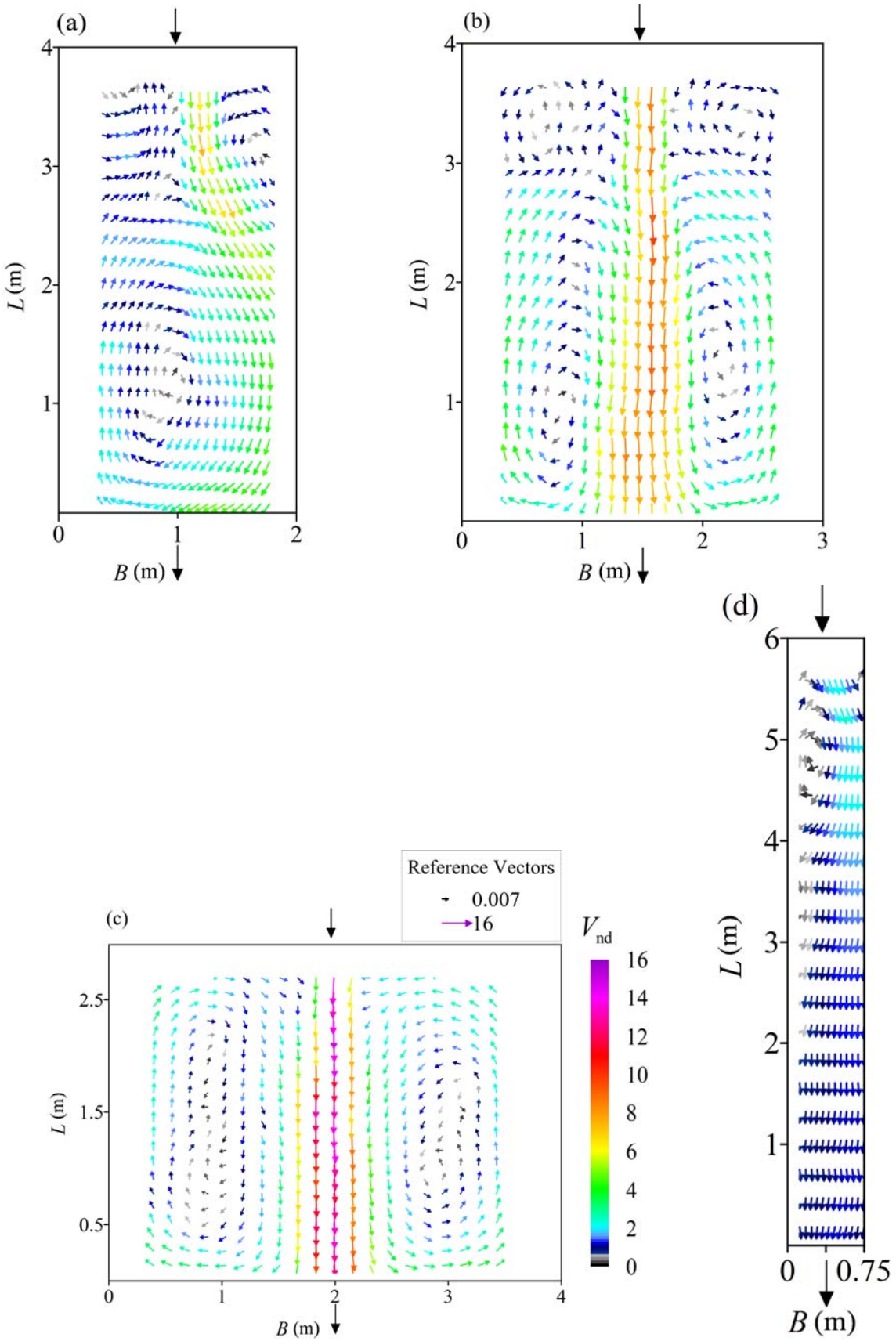

Figure 4. 3 - Examples of velocity maps. Normalized velocities $V_{nd} = V/V_{res}$ for various flow patterns types and different reservoir geometry (a) A1: L/B =2, B/b =8, V_{res}= 17.5 mm/s, (b) S1: L/B = 1.33, B/b = 12, V_{res}=11.6 mm/s, (c) S0: L/B = 0.75, B/b = 16, V_{res}= 8.7 mm/s (d) A2: L/B = 8, B/b =3, V_{res}= 46 mm/s

4.1.2 Comparison with recent experimental studies

As it has been already cited, M. Dufresne recently performed experiments at Liège University (ULg) using an experimental facility extremely similar to the one of EPFL. His aim also was to investigate the typology of flow fields developing in rectangular shallow reservoirs, focusing his attention on the measure of reattachment lengths.

The experimental facility at Liège University has a maximum length L = 7 m and a maximum width B = 0.985 m. The width b of the inlet channel also varies between 0.08 m and 0.485 m.

So, a useful and profitable comparison and mutual integration between the experimental results obtained by the 2 different experimental facilities is possible.

In Figure 4. 4 the EPFL results and these of Dufresne et al. (2010a) are compared. Both studies concerned flow-field typology in rectangular shallow reservoirs with symmetrical inlets and outlets, and the authors partly investigated the same geometrical domain. While velocity was measured over the entire reservoir at EPFL, allowing to define streamlines and average velocities, Dufresne et al. focused on the variability of the reattachment length. A classification of the possible flow patterns was also given, by suggesting the cited criterion to distinguish between symmetrical and asymmetrical flow patterns (T parameter). The geometric configurations tested in the framework of this thesis cover a wide range of combinations of reservoir length-to-width ratio and expansion ratio, extending the range of geometries tested by Kantoush, while Dufresne et al.'s tests mainly analysed the region of transition between asymmetric and symmetric flow fields for $2 < B/b < 4$ and $1 < L/B < 3$. Furthermore, the latter also performed a sensitivity analysis of the non-dimensional parameters h/B, R_{in} and F_{in}. Therefore, not all the data shown in Figure 4. 4 correspond to the same values of h/B, R_{in} and $\mathsf{F}_{in.}$

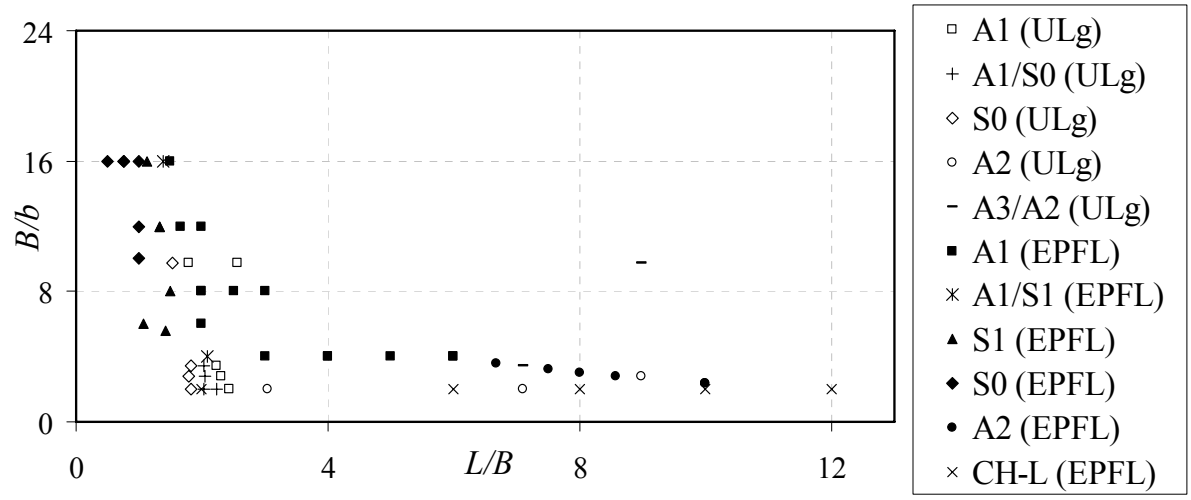

Figure 4. 4 Overview of tests performed at EPFL (present study and Kantoush 2008) and by Dufresne *et al.* (2010a), resulting in symmetrical (S0 and S1), asymmetrical (A1, A2 and A3), and channel-like (CH-L) flow patterns

The geometrical (h/b or h/B) and hydraulic (R_{in} and F_{in}) parameters influence the flow-field typology. For example, Dufresne et al. (2010a) found that the flow field changes from A2 to A3 if $h/B < 0.1$. Their A3 type is similar to the A2 flow field but it is characterized by a further recirculation zone in the downstream reservoir portion. To analyse exclusively the effect of length-to-width and expansion ratios, only tests conducted under identical hydraulic conditions and h/b are plotted in Figure 4. 2. Note from Figure 4. 4 that the transition region from asymmetric to symmetric flows occurs if $1.5 < L/B < 2.2$, depending on the expansion ratio, though Dufresne *et al.*'s tests neither had the same hydraulic conditions, nor the same h/b ratio. The critical values of T proposed by Dufresne *et al.* (2010a) for the transitional zone are confirmed by the present tests. Further, these experiments also show a channel-like flow CH-L independent of the length-to-width ratio at $B/b = 2$, in agreement with Abbott and Kline (1962). In contrast, Dufresne et al. (2010a) found for $B/b = 2.031$ different flow patterns (S0, A1, A2) depending on the length-to-width ratio. This discrepancy may be due to the different hydraulic conditions at $B/b \sim 2$, namely $F_{in} = 0.2$ in Dufresne et al., while $F_{in} = 0.1$ in EPFL experiments.

Table 4. 1– Dimensional parameters of the two experimental campaigns

	Dufresne's experiments	**Camnasio's experiments**
Q [l/s]	1.6 ÷ 78.9	7
h [m]	0.05 ÷ 0.4	0.2
L [m]	1.2 ÷ 7	1 ÷ 6
B [m]	0.78 ÷ 0.985	0.5 ÷ 4
b [m]	0.08 ÷ 0.485	0.25

Table 4. 2– Range of the non dimensional parameters analysed in the experiments

Non dimensional parameter	**Investigated values in Dufresne's experiments at ULg**	**Investigated values in Camnasio's experiments at EPFL**
$\frac{L}{B}$	1.538 ÷ 8.974	0.5 ÷ 12
$\frac{B}{b}$	2.031 ÷ 9.75	2 ÷ 16
$\frac{h}{B}$	0.05 ÷ 0.509	0.05 ÷ 0.4
$\frac{h}{b}$	0.103 ÷ 4.963	0.8
$\frac{L}{b}$	3.711 ÷ 87.5	4 ÷ 24
$Fr_{in} = \frac{U}{\sqrt{g \cdot h}}$	0.05 ÷ 0.418	0.1
$\mathrm{Re}_{in} = \frac{4 \cdot \rho \cdot U \cdot h}{\mu}$	4860 ÷ 61723	112000

It is important to note once again that, as it results from Table 4. 2, the experiments of Camnasio at EPFL were performed at a fixed R_{in} and F_{in} and also at a fixed *h/b* ratio. Further research would be

necessary in the future in order to analyse more systematically the influence of h/b, R_{in} , F_{in} on the flow field, because it could be the cause of the differences found by the authors for some reservoir configurations; furthermore, it could lead, as it will be presented in chapter 7, to new types of flow patterns, different from those analyzed up to now.

4.1.3 Conclusions

Average velocity fields and streamlines (see the attached dvd for the view of the complete set of experimental results) for a wide range of rectangular shallow reservoirs were obtained. In agreement with previous works, different types of flow patterns were identified, including channel-like flow, two symmetric flow patterns characterized by two or four large eddies, and two asymmetrical flow patterns. Their development is due to the combined effect of reservoir expansion and length-to-width ratios. Therefore, a flow pattern corresponding to a certain reservoir configuration can be predicted on the basis of the values of these two non-dimensional parameters, at fixed hydraulic conditions. Average velocity fields indicate large gradients between the main jet and the recirculation zones for all flow patterns, except for the reservoir configurations which tend to the one-dimensional channel. The agreement between the present results and these of Dufresne et al. (2010a) confirms the validity of the performed tests strengthening confidence in the results, as they emerge from two independent facilities.

4.2. Turbulence analysis

4.2.1 Turbulent and average kinetic energy

Since the study of turbulence is fundamental to understand, for example, the mixing processes in reservoirs or the interaction between water and sediments entering in a reservoir, turbulence statistics were calculated based on the measurements of the instantaneous velocity *V(0.4h)* by UVP for 4 reservoir geometries (Table 4. 3), chosen as reference because each one is representative of one type of flow pattern.

Table 4. 3–Four reference reservoir configuration and classification of their respective flow pattern type.

L [m]	3	4	4	6
B [m]	4	3	2	0.75
Flow pattern type	S0	S1	A1	A2

Each one of the two instantaneous horizontal velocity component, ***u*** and ***v***, obtained by UVP measurements, can be decomposed in the following way: ***u*** = $u + u'$ and ***v*** = $v + v'$, where u and v are the time-averaged quantities, while u' and v' are the fluctuating components of velocity due to turbulence.

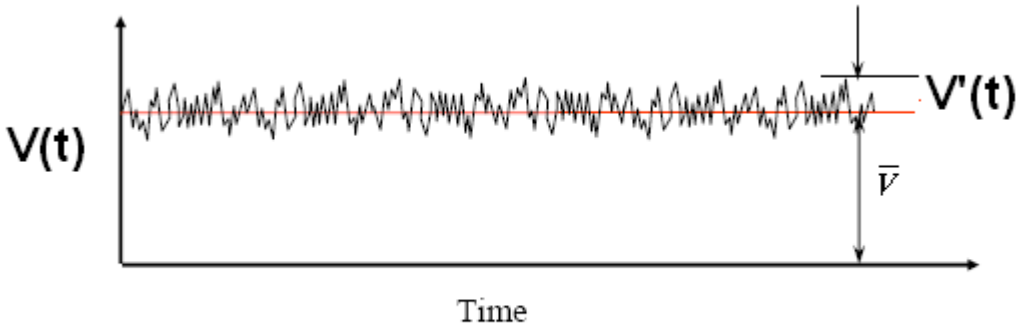

Figure 1 – Example of turbulent signal of V(t) velocity, where $\overline{V}$ is the time averaged velocity and V'(t) is the fluctuating component

Therefore, it is possible to define the turbulent kinetic energy k for unitary mass:

$$k = 0.5 \cdot (\overline{u'^2} + \overline{v'^2}) \qquad [m^2/s^2] \qquad (4.1)$$

neglecting the small contribution which would be given by the vertical velocity fluctuating component *w'* .

In the present case, the turbulent kinetic energy *k* has been then normalized to the kinetic energy per unit mass E_k, which is associated to the average velocity $\overline{V}$ in every measurement point of the reservoir:

$E_k = 0.5 \cdot \overline{V}^2$ [m^2/s^2] (4.2)

In this way, the normalized turbulent kinetic energy k/E_k can be considered as an indicator of the relevance of the fluctuating velocity component, that is to say of turbulence, with respect to the average velocity field.

The maps of the normalized turbulent kinetic energy k/E_k for different types of flow patterns are shown in Figure 4. 5. It can be seen that the highest values of k/E_k are always located in correspondence of the core of the eddies and the maximum value is about 1.4. On the contrary, along the main jet and in the zones of the reservoir where a uniform distribution of velocity is present (Figure 4. 5d - downstream), $k/E_k \leq 0.1$. This facts mean that along the main jet the velocity vector is quite constant during time, with only small fluctuations, while in the recirculation zones the velocity vectors are subjected to a relatively significant random variation of their direction, if compared to the low average velocity of these zones.

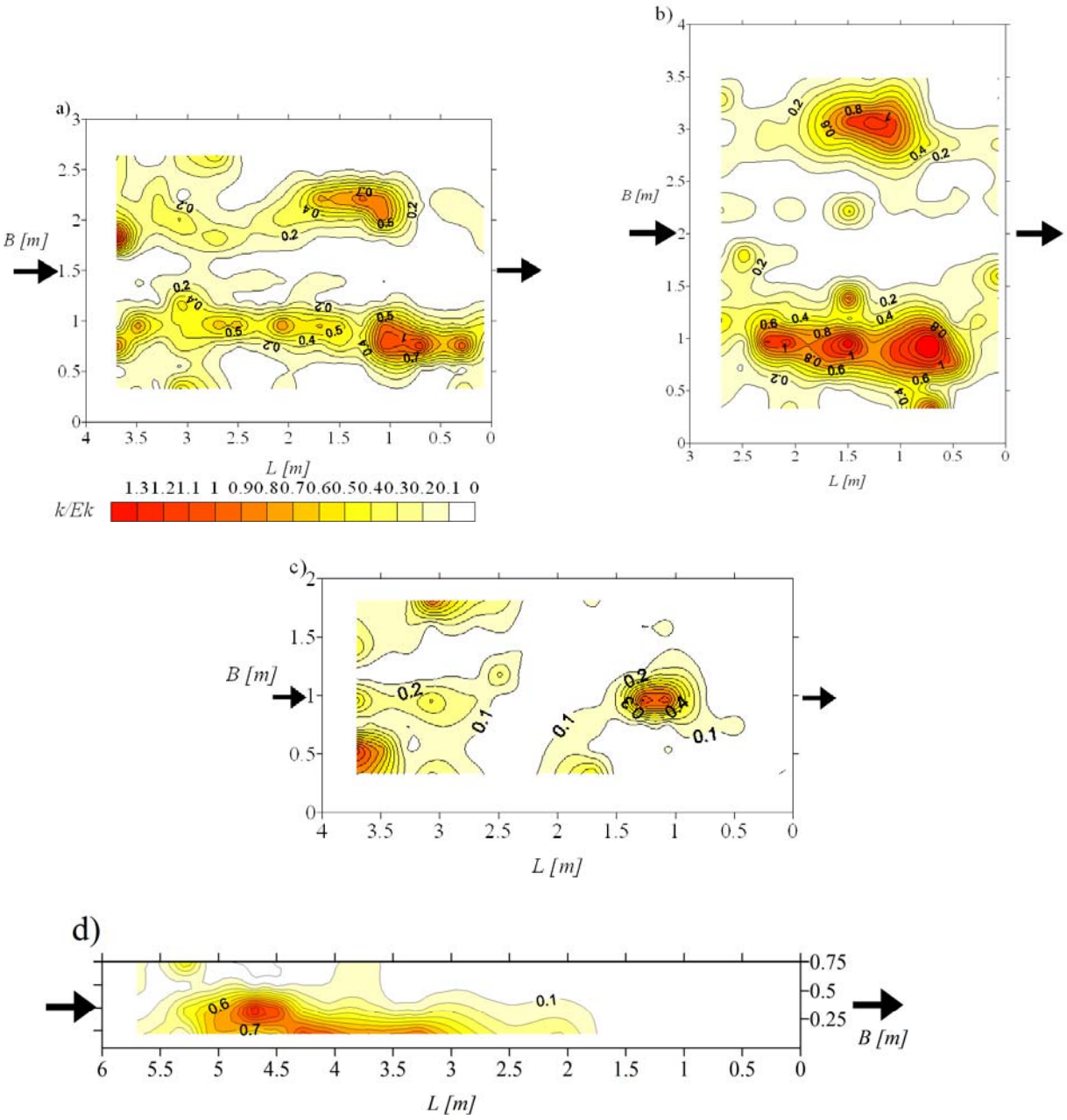

Figure 4. 5 – Turbulent kinetic energy *k* normalized to the local average kinetic energy E_k for the different types of flow patterns according to the classification of Camnasio et al. (2011): a) *L* = 4 m *B* = 3 m , 4 eddies symmetric flow pattern S1 – b) *L* = 3 m *B* = 4 m, 2 eddies symmetric flow pattern S0 – c) *L* = 4 m *B* = 2 m, asymmetric flow pattern A1 – d) *L* = 6 m *B* = 0.75 m, asymmetric flow pattern A2.

4.2.2 Reynolds shear stresses

Starting from the available UVP measurements, it is possible to obtain the Reynolds Shear Stresses (RSS) $\tau_{ij} = -\rho \cdot \overline{\boldsymbol{u}_i' \cdot \boldsymbol{u}_j'}$. In particular, in this case the unitary mass Reynolds Shear Stresses $|\overline{u'v'}|$ were calculated in every measurement point of the reservoir and normalized to $\overline{V}^2$.

The resulting maps for the 4 reference reservoir configurations are shown in Figure 4. 6. The only possible observation is that also in this case the highest values of Reynolds Shear Stresses are located in the centre of the re-circulation zones, since, as for turbulent kinetic energy, where velocity are small the fluctuating component have a significant relevance.

Anyway, in order to carry out a more reliable analysis on this type of phenomenon, it would be necessary to have velocity signals with a longer temporal duration, in the way to be able to calculate more accurate statistics.

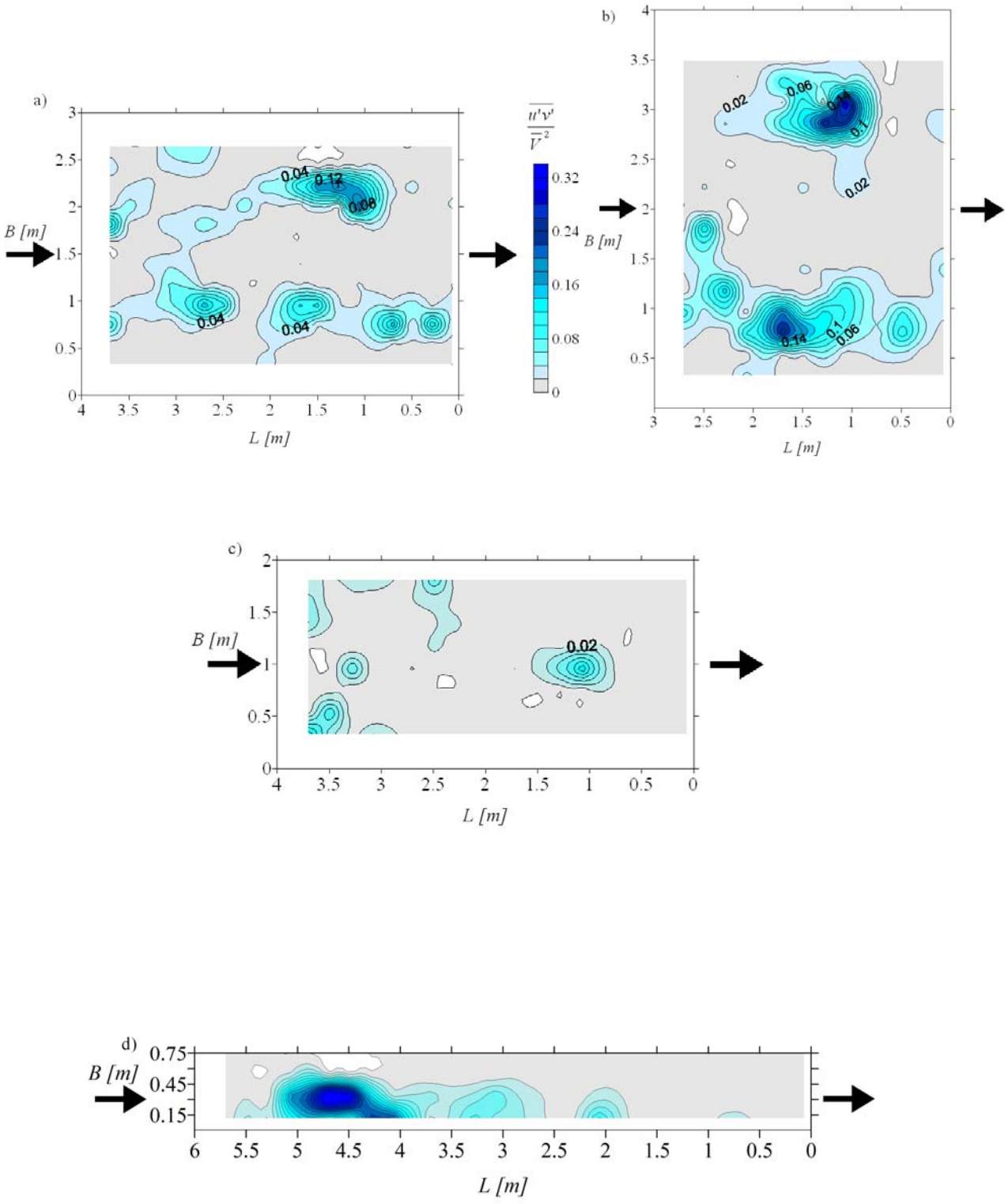

Figure 4. 6 – Absolute value of the Reynolds stresses normalized to $\overline{V}^2$ for the 4 reference reservoir configurations. a) *L* = 4 m *B* = 3 m , 4 eddies symmetric flow pattern S1 – b) *L* = 3 m *B* = 4 m, 2 eddies symmetric flow pattern S0 – c) *L* = 4 m *B* = 2 m, asymmetric flow pattern A1 – d) *L* = 6 m *B* = 0.75 m, asymmetric flow pattern A2.

4.3. Reservoir kinetic energy

The local average kinetic energy E_k was integrated numerically on the entire reservoir surface A, in order to obtain an index associated to every geometric configuration of the reservoir, E_{k_tot}, which represents the global kinetic energy content of the measured average velocity field:

$$E_{k\_tot} = \int_A E_k dA \ [\mathrm{m^4/s^2}] \qquad (4.3)$$

Then, this global value E_{k_tot} was divided by the reservoir surface, in order to obtain a specific value, E_{k_unit} [m^2/s^2], representing the average kinetic energy content of the unitary surface for every reservoir configuration. The aim was to analyse if it exist a correlation between the specific kinetic energy content E_{k_unit} and the type of flow pattern developing in the reservoir.

The calculated quantities for every reservoir configuration in which UVP velocity measurements were carried out, are shown in Table 4.4.

Table 4. 4 – Reservoir kinetic energy analysis for reservoir configurations tested by UVP.

L [m]	B [m]	Type of flow pattern	E_{k_tot} [m^4/s^2]	Area A [m^2]	E_{k_unit} [m^2/s^2]	E_{k_PF} [m2/s2]	E_{k_unit}/E_{k_PF} [-]
6	4	A1	0.015	17.16	0.0009	3.83E-05	23.51
5.8	4	S1	0.015	17.16	0.0009	3.83E-05	23.51
5.3	4	S1	0.014	15.42	0.0009	3.83E-05	23.51
5	4	S1	0.012	14.63	0.0008	3.83E-05	20.90
3	4	S0	0.008	8.31	0.0009	3.83E-05	23.51
4	3	S1	0.01	8.31	0.0012	6.81E-05	17.63
4	2	A1	0.007	5.37	0.0012	1.53E-04	7.84
4	1	A1	0.005	2.29	0.0023	6.13E-04	3.76
6	1	A1	0.006	3.54	0.0018	6.13E-04	2.94
6	0.75	A2	0.004	2.36	0.0016	1.09E-03	1.47
6	0.6	A2	0.006	2.36	0.0026	1.70E-03	1.53

Nevertheless, the analysis of the results shows that a correlation between flow pattern type and E_{k_unit} doesn't exist; on the contrary, a relationship between E_{k_unit} and reservoir size con be found. In fact, it appears that small reservoirs, with a surface smaller than 5 m^2, are characterized by an average specific kinetic energy content (≈ 0.002 m^2/s^2) that is higher (generally the double) than the energy content of the larger reservoirs (A > 5 m^2; E_{k_unit} = 0.001

m^2/s^2); in fact, the water in "small" reservoirs is characterized on average by higher velocities, while for "large" reservoirs the main part of the reservoir is occupied by almost still water.

In order to compare the specific kinetic energy content of the reservoir with the specific energy content that would exist in the theoretic case of a plug flow, E_{k_unit} has been normalized to the local kinetic energy correspondent to a plug flow condition E_{k_PF}:

$$E_{k\_PF} = 0.5 \cdot V_{res}^{\ 2} \qquad (4.4)$$

The values of the non-dimensional index $E_{k\_ND} = E_{k\_unit} / E_{k\_PF}$ are indicated in Table 4.4; it can be observed that the value of E_{k_ND} tends to one, as the flow pattern tends to the channel-like flow, that is to say for the A2 flow patterns cases.

In the end of this analysis, a relationship between the area of the reservoir and E_{k_ND} has been searched. The experimental points resulted to be quite well interpolated (R^2 = 0.899) by a logarithmic law, as shown in Figure 4. 7.

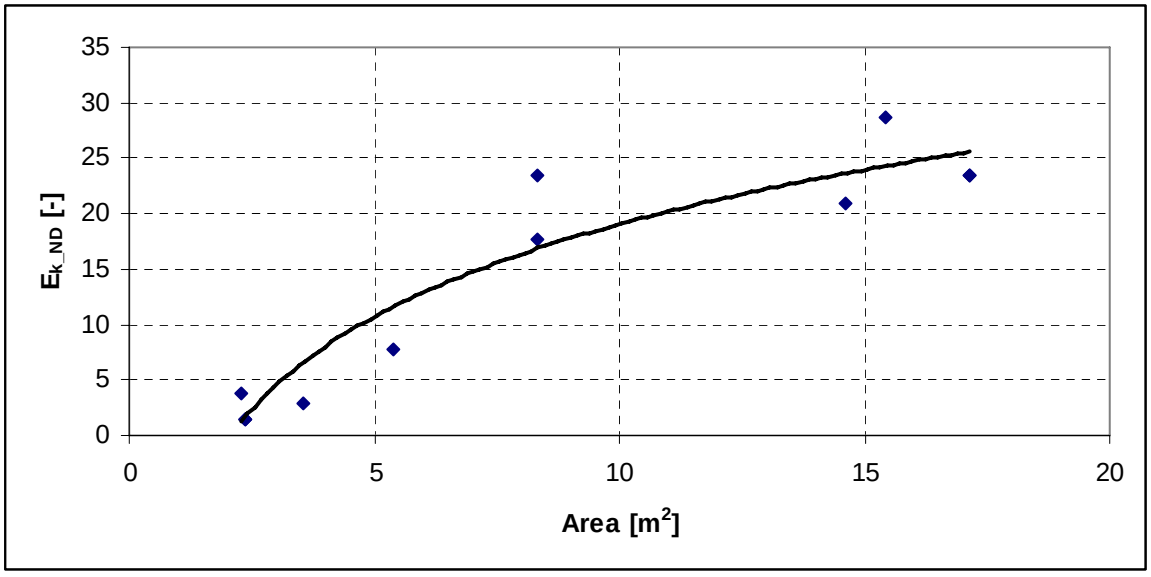

Figure 4. 7 – Logarithmic relationship between reservoir surface *A* and non-dimensional unitary kinetic energy E_{k_ND}.

The formulation of the logarithmic fitting line is:

$$E_{k\_ND} = 12.07 \cdot \ln(A) - 8.735 \qquad (4.5)$$

Thanks to this relationship, for a given reservoir surface, the E_{k_ND} index can be obtained; then, after the calculation of the theoretic plug flow velocity V_{res} the unitary kinetic energy content

can be obtained ($E_{k\_unit} = E_{k\_PF} \cdot E_{k\_ND}$). If this index is close to unit, it means that the reservoir is near to the plug flow condition, without the presence of dead water zones. However, more reservoir configurations should be tested in order to confirm the logarithmic relationship here proposed.

4.4. Momentum of asymmetry

4.4.1 Transition from S1 to A1

As it has been underlined in the paragraph 4.1.1, the transition from the symmetric flow pattern S1 to the asymmetric flow pattern A1 doesn't occur abruptly at a fixed length, but on the contrary it exists an instability zone where it is possible the development of both the flow patterns.

Experimental and numerical results showed that it doesn't exist a unique critical length of transition, since the transition between the two regions is characterized by a quite narrow band of lengths for which a phenomenon of bifurcation takes place (Dewals et al., 2008; Dufresne et al., 2010a; Camnasio et al., 2011): for the same reservoir length L, two solutions to the Navier-Stokes equations exist, one corresponding to a symmetric flow pattern, the other to an asymmetric flow pattern. Furthermore, the flow patterns existing in this zone are unstable, in the sense that a small external perturbation can lead the symmetric flow pattern to evolve in the asymmetric one.

For example, the transition between the asymmetrical A1 and the symmetrical S1 flow pattern occurs, if we considered a fixed width B = 4 m, at a length L between 5 m and 6 m; therefore, here it has been chosen to focus on the study of these reservoir configurations with varying length, in particular L = 4.5 m ÷ 6 m, with the purpose to analyse in detail the characteristics of this transitional zone.

In order to perform this study, as proposed by Dewals et al. (2008), the global non-dimensional moment M has been chosen as a synthetic indicator of the asymmetry of the flow field:

$$M = \frac{1}{L} \cdot \int_0^L |m(x)| dx \qquad (4.6)$$

where *m(x)* is the non-dimensional local moment of asymmetry, calculated at each reservoir cross section, *x* being the distance from the upstream reservoir side, and *y* its orthogonal coordinate:

$$m(x) = \frac{1}{B} \cdot \int_{-B/2}^{B/2} \frac{u(x,y) - V_{res}}{V_{res}} \cdot \frac{2y}{B} dy . \qquad (4.7)$$

The moment *M* is 0 for symmetrical reservoir configurations, while its value increases with the increase of asymmetry in the velocity field.

As far as concern the laboratory experiments, the experimental data which were available before the present study concerned only reservoir lengths of 4 - 5 and 6 m (Dewals et al., 2008) at a fixed width B = 4 m; on the contrary, the experiments here presented analysed additional reservoir configurations with lengths L = 4.5 - 4.8 – 5.2 - 5.3 – 5.5 and 5.8 m which are included in the critical zone of instability. The corresponding global moment of asymmetry *M*, calculated on the basis of the performed UVP velocity measurements, are represented in Figure 4. 8.

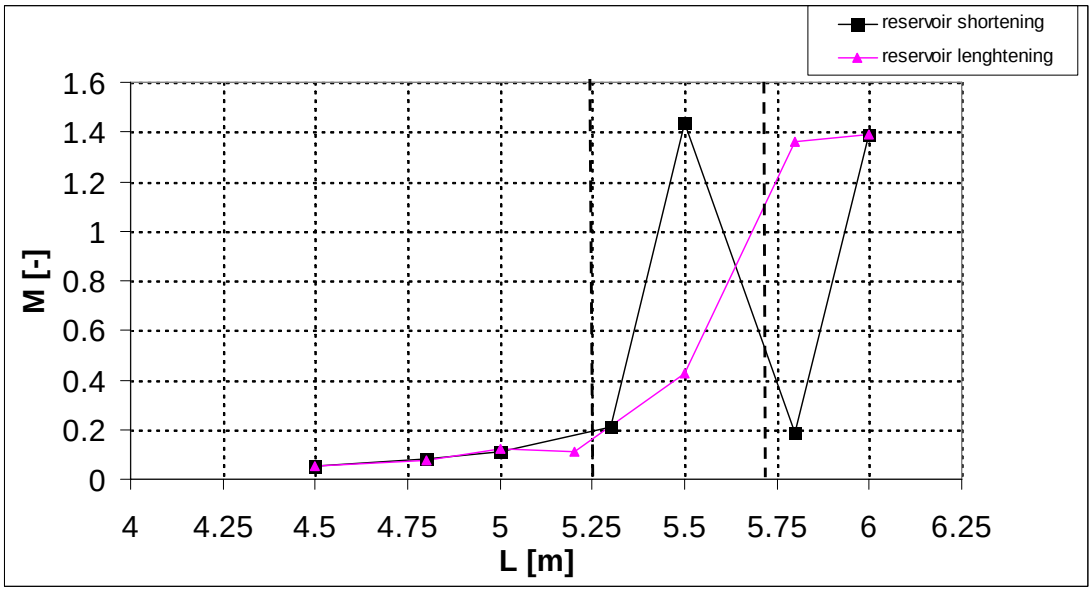

Figure 4. 8 – Global moment of asymmetry *M* calculated for the experimentally tested reservoir configurations, as a function of reservoir length *L*

From these experiments, it was possible to define a region of flow pattern instability, in which the two types of flow patterns are both possible, and they are very sensitive to external small

perturbations. In fact, as it can be seen in Figure 4. 8, for reservoir lengths between 5.3 m < L < 6 m, the velocity field is characterized by two possible values of the moment of asymmetry, one corresponding to a symmetrical flow pattern (and therefore close to zero), the other corresponding to an asymmetrical flow pattern.

Numerical simulations investigating the zone of instability with a reservoir width of 4 m had been already carried out at Liège University. They were performed by the 2D depth-averaged code WOLF2D, for reservoir lengths in the range 4.5 m – 6 m, using an algebraic model, the Fisher model, as turbulence closure (for further details on the numerical model, see chapter 5).

The simulations, whose results (expressed by the global moment of asymmetry M) are represented in Figure 4. 9, showed the existence of an "hysteresis" phenomenon, that is to say an interval of reservoir lengths for which the developing flow field depends on the initial conditions of the simulation. If simulations are performed starting from a reservoir length L = 6 m, corresponding to a deviated jet, and then the length is progressively decreased (so that the successive simulation starts from an already deviated flow pattern which is utilized as initial condition for the successive simulation), the flow pattern remains asymmetrical till a reservoir length L = 4.75 m. On the contrary, if the first simulation is performed for a reservoir width B = 4 m, and then the successive simulations are performed by progressively lengthening the reservoir (so that the second simulation starts from a initially symmetrical flow pattern), the symmetry is maintained up to a length L = 5.85 m. So the total width of the instability zone, according to numerical simulations, is 1.1 m. In conclusion, when the initial flow pattern is asymmetric, reservoir length must be very small to force the flow pattern to symmetry. On the contrary, when the initial condition is symmetric, a very long length is necessary to allow the instability of the flow pattern to lead to asymmetry.

These numerical results indicate that the flow pattern calculated by the numerical model with a Fisher turbulence closure is very sensitive to the initial condition in proximity of the flow pattern transition zone.

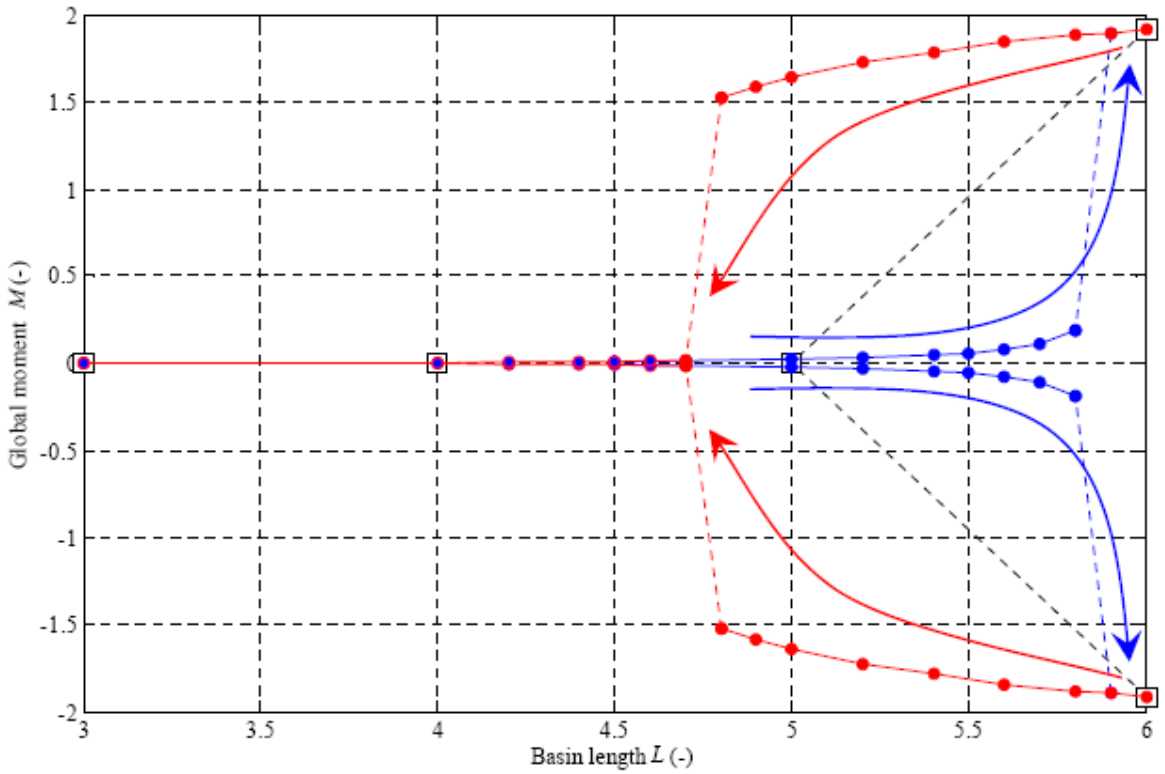

Figure 4. 9 – Phenomenon of hysteresis found in the simulations by WOLF2D – turbulence closure: Fisher model

In order to verify if the numerically found hysteresis phenomenon was confirmed by physical evidence, experiments were performed by progressively lengthening/shortening the reservoir, and then measuring the velocity field of every reservoir configuration. This experimental procedure was chosen in order to see if the initial condition of the flow, asymmetric or symmetric, could effectively influence the final state of the flow field for a given reservoir configuration. Nevertheless, as it can be observed in Figure 4. 8, experiments didn't assess the existence of the numerically found hysteresis phenomenon. Every experimental test is a "standing alone", since there are a lot of external disturbances which can lead to the formation of a deviated jet; in the instability region an asymmetrical or symmetrical flow pattern can develop indifferently, not depending on the initial condition of the experiment.

Moreover, the performed experiments showed that the critical region of bifurcation of Navier-Stokes equations takes place for a range of lengths narrower than the one resulting from numerical simulations: in fact, the instability zone resulting from the experiments has a width of about 50 cm

in correspondence of B = 4 m, which is consistent with the width of the transitional zone according to the non-dimensional T parameter.

In Figure 4. 10, the local *m(y)* moment of asymmetry calculated for all the experimentally tested reservoir configurations is shown. It has to be noted that the experimental values of moment are not exactly zero even for symmetrical flow patterns due to the experimental uncertainties.

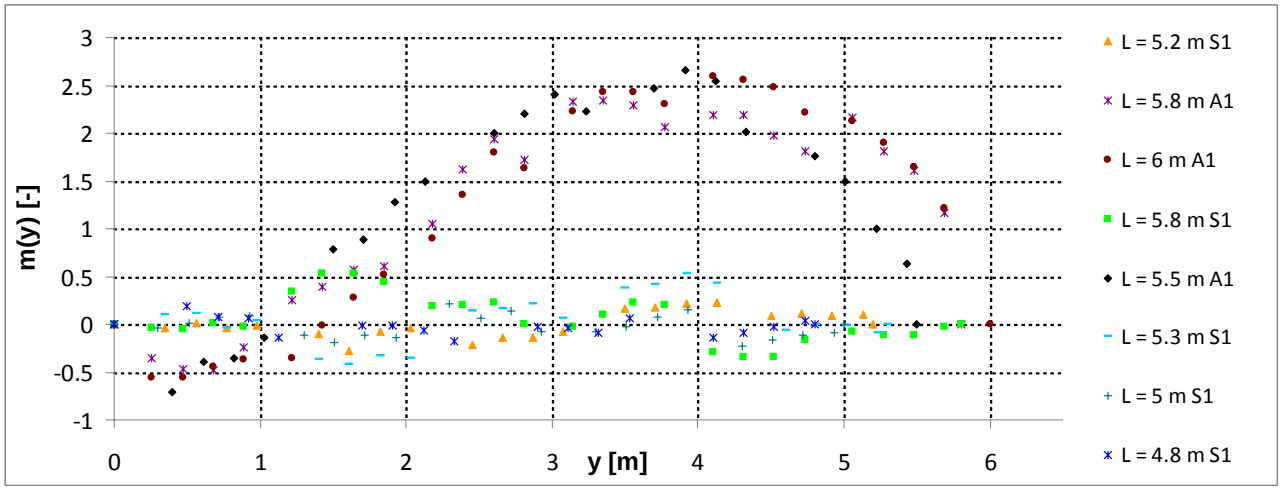

Figure 4. 10 – Local moment *m(y)* for different experimentally tested reservoir configurations (*B* = 4 m and *L* = 4.8 – 5 – 5.2 – 5.3 – 5.5 – 5.8 – 6 m)

4.4.2 Transition from CH-L to A1 or A2

Also the transition from the channel-like flow CH-L to the asymmetric flow field A1 or A2 has been investigated in detail, in order to find the critical expansion ratio at which the transition occurs. In fact, from the experimental data available up to now, only the expansion ratio was found to influence the transition of the flow pattern to a channel-like flow, without any dependence from the length-to-width ratio.

A fixed reservoir length L = 6 m was chosen (similarly to Dewals et al., 2008) and the width B of the reservoir was varied. Since the experimental results of Kantoush (2008) and Camnasio et al. (2011) showed that for B = 1 m the flow pattern is asymmetric A1, while at B = 0.5 m channel-like flow CH-L exists, different reservoir widths were tested in this critical range: B = 0.5 - 0.6 – 0.75 - 1 m. Experimental results showed that the channel-like flow develops only in correspondence of B

= 0.5 m, while for all the other configuration the flow pattern is asymmetrical: flow pattern A1 for B = 1 m and flow pattern A2 for B = 0.6 m and 0.75 m.

The resulting values of the global moment of asymmetry M for the tested configurations are shown in Figure 4. 11.

On the other hand, from Figure 4. 12b it can be seen that, for the configurations characterized by an A2 flow field, the local moment is significantly different from 0 only in the upstream part of the reservoir, where the deviation of the jet occurs, while in the downstream part of the reservoir the local moment is nearly 0, because velocity are approximately uniformly distributed on the entire cross section. About the global moment, for these configurations its value is significantly lower (< 0.5) than for the A1 flow field configurations, as it results from Figure 4. 11.

In has to be underlined that in this case nor the experimental tests, nor the numerical simulations (performed by the numerical code WOLF2D), have shown the possibility of co-existence of more than one solution for a fixed reservoir width.

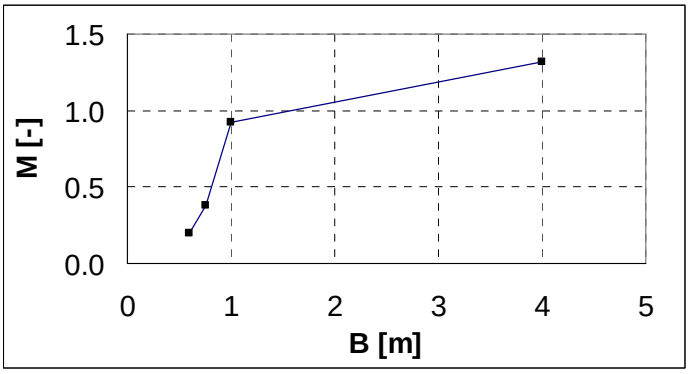

Figure 4. 11 – Experimental values of the global moment of asymmetry for the configuration with varying width B = 0.6 – 0.75 – 1 – 4 m and fixed length L = 6 m.

a)

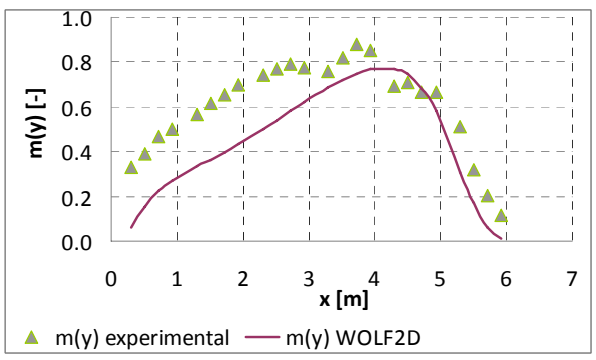

b)

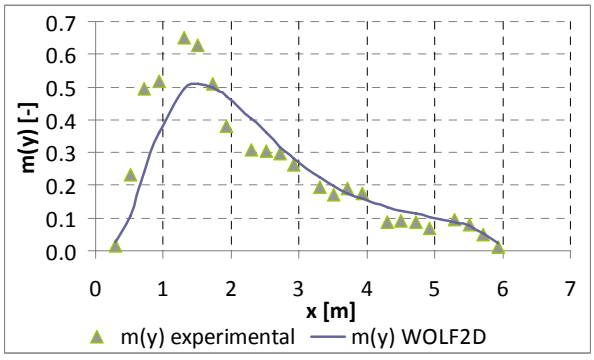

Figure 4. 12 – Local moment for the reservoir configurations a) B = 1 m b) B = 0.75 m;

4.4.3 R and T parameters

The *R* shape parameter proposed by Dewals et al. (2008) as an indicator of flow pattern asymmetry/symmetry was calculated for all the tested configurations. This parameter is an empirical combination of the expansion ratio and of the length-to-width ratio ($R \approx B/b \times (L/B)^{0.89}$), coming from the fitting of the experimental data previously available. Based on these data, a threshold *Rc* was identified: for $Rc < 19$ the flow field was symmetric, as far as concerned the previously available data. Nevertheless, the authors stated that a wider set of experiments was necessary to generalize this result. In fact, the critical threshold *Rc* was not confirmed by the experiments here presented: in fact, the new experiments, carried out on a much wider set of combinations between expansion ratio and length-to-width ratio, showed that the critical value *Rc* doesn't correctly distinguish between a symmetrical flow pattern and an asymmetrical one, as it can be seen in Table 4. 5a) and b). This tables in fact show that some reservoir configuration (4 x 1 m, 4 x 2 m, 3 x 1 m) can be characterized by an asymmetrical flow pattern (type A1 or A2) even if the corresponding *R* parameter ($R \approx 14 - 10$) is much below the critical threshold identified by previous experiments. Also the configurations 5x3 m 5x2m 5x1 m present asymmetrical flow patterns even if their *R* parameter is below the critical value *Rc*. On the contrary, for the configuration 5x4 m the experimentally found flow field is symmetrical even if its *R* parameter is slightly higher than the critical threshold *Rc*.

Table 4. 5 –a) Flow pattern type corresponding to the tested reservoir configurations b) *R* parameter, calculated according to Dewals et al. (2008), for the same reservoir configurations

a)

		L [m]			
		6	5	4	3
B [m]	4	A1	**S1**	S0	S0
	3	A1	**A1**	S1	S0
	2	A1	**A1**	**A1**	S1
	1	A2	**A2**	**A2**	**A1**
	0.5	CH-L	CH-L	CH-L	CH-L

b)

		L [m]			
		6	5	4	3
B [m]	4	23.0	**19.5**	16.0	12.4
	3	22.2	**18.9**	15.5	12.0
	2	21.3	**18.1**	**14.8**	11.5
	1	19.7	**16.8**	**13.7**	**10.6**
	0.5	18.3	15.5	12.7	9.9

In conclusion, the formulation suited to represent the transition between a symmetric flow pattern S1 and an asymmetric flow pattern A1 are the relationship proposed by Dufresne et al. (2010a) and confirmed by Camnasio et al. (2011). In fact, according to these authors, the already cited non-

dimensional parameter $T = L/[(B-b)^{0.6} \cdot b^{0.4}]$ was proposed to delimitate the transitional zone of instability between the two types of flow pattern, and this criterion well interprets all the experimental data available up to now, which have been collected in different experimental campaign, by different authors and working on different experimental facilities.

4.5. Influence of the location of the inlet and outlet channel on the flow field and on sediments deposits

All the tests presented in the previous paragraphs concerned reservoir geometries having the inlet channel placed at the middle of the upstream edge, just in front of the outlet channel, placed at the middle of the downstream edge. On the contrary, now the results about the study of the influence of an asymmetric position of the inlet and of the outlet channels on flow patterns and on sediments deposits are presented. For further details about the analyzed reservoir configurations and the tests procedures see chapter 3.4.2.

4.5.1 Velocity fields

Velocities were measured by UVP first during clear water tests, then during tests with sediments supplying, in order to investigate the possible influence of suspended load and/or of sediments deposits on the flow patterns. Vectorial velocity maps were produced for all the tested reservoir configurations. The time-averaged local horizontal velocity $V = \sqrt{u^2 + v^2}$ at every measurement point was normalized to the average theoretical plug flow velocity $V_{res} = Q/(B \cdot h) = 8.75$ mm/s (Oca et al., 2004) assuming the basic hypothesis of a one-dimensional motion of the whole discharge Q through the cross section $B \cdot h$. Figure 4. 13 shows the distribution of the normalized average horizontal velocities $V_{nd} = V / V_{res}$ in the entire reservoir for the performed experiments.

For all the tested configurations the velocities along the main jet have a minimum in the order of 100 - 120 mm/s in the downstream part of the reservoir, while in the centre of the recirculation zones, velocity reaches a minimum of about 10 - 20 mm/s. Figure 4. 13a) b) c) d) correspond to the flow patterns measured after 4 hours of sediments supplying. Figure 4. 13 e) shows the flow pattern found for the L-R configuration during tests with clear water. Only for this reservoir configuration the flow pattern which developed during tests with suspended sediments is different from the one developing during clear water tests.

In the basic symmetrical geometry (Figure 4. 13 a) C – C the four eddies flow pattern is symmetric S1 , even if the two upstream eddies are very small. Only one of these eddies is visible, so the flow pattern can be considered as a transition between the S1 flow field and the S0 flow field, characterized by only one eddy on each side of the reservoir, which develops if $L/B \leq 1$, as already explained in paragraph 4.1.1. A local increase of velocity in the main jet can be clearly seen in Figure 4. 13 and it is due to the presence of bed forms (see Figure 4. 14a) which locally reduce the available cross section, causing an increase of velocity.

In the configuration L– L the main jet is deflected towards the nearer side wall, it flows along it and then goes out through the outlet channel. A big re-circulation zone develops in the remaining part of the reservoir (Figure 4. 13b). The deflection of the jet towards the lateral wall could be attributed to the “Coanda effect” (Wille and Fernholz, 1965). Another clear example of the deviating effect of a lateral wall on a free surface water jet can be found in Lalli et al. (2004).

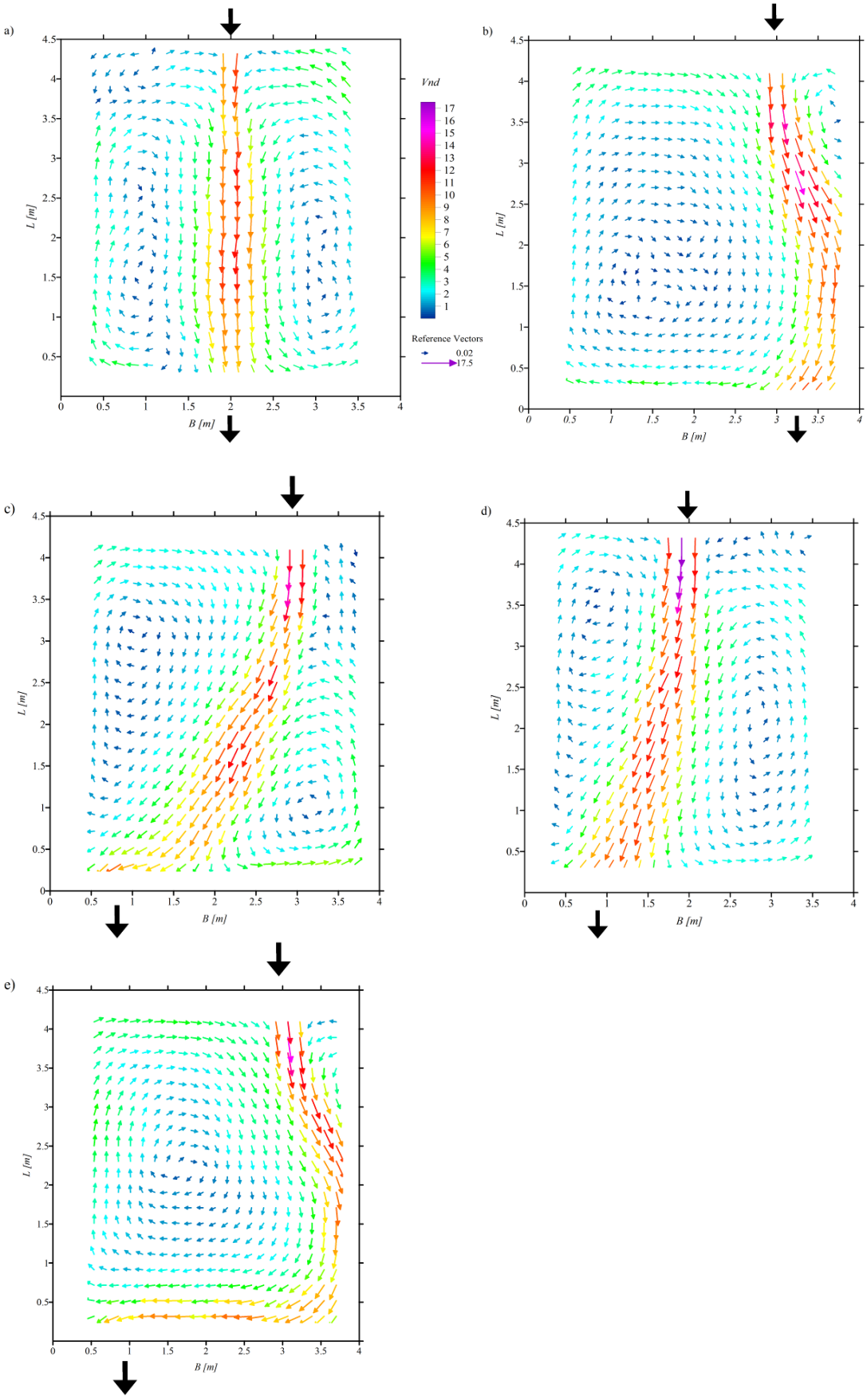

Figure 4. 13 – Normalized velocity vectors maps (V_{res}= 8.75 mm/s) obtained for the four tested configurations a) C – C b) L – L c) L – R(0) d) C - R e) L – R(1) flow pattern for tests with clear water; Re_{in} = 112'000 Fr_{in} =0.1 h/b= 0.8

For the configuration L– R, the flow patterns measured at the end of the test with suspended load (Figure 4. 13c : L – R(0), with zero reattachment points of the jet on the lateral wall) is significantly different from the flow patterns measured during clear water test (Figure 4. 13e: L– R(1), with one reattachment point on the lateral wall). When the bottom of the reservoir is clean, the main jet is deflected towards the nearer lateral wall where it has a reattachment point. Then it follows the wall and finally it goes along the downstream wall towards the exit. Only a large recirculation zone develops in the main part of the reservoir. On the contrary, after only about 30' of sediments supply, the main water jet goes more directly towards the outlet channel as shown in Figure 4. 13c. The jet impinges on the downstream wall at a distance of about 0.9 m from the axis of the outlet channel, then it splits in two and two eddies of different size rotating in opposite directions are formed. It can be excluded that the sediments after only half an hour can create a deposit able to deviate the jet, since the thickness of sediments deposits at that time is only 3 - 4 mm; furthermore, in the other experiments, the sediments deposits thickness is not able to change the direction of the main jet. On the contrary, for this reservoir configuration, after this sudden change of flow pattern, the velocity field remained stable during the remaining duration of the experiment.

Even when the flow was stopped after two hours, in order to take the first measurement of sediments deposits by laser, and then the pump was started again, the flow pattern immediately develops in the form represented in Figure 4. 13c. Of course, the flow field corresponding to clear water conditions, was measured more than once, starting by still water conditions, in the way to assess that the flow pattern of Figure 4. 13e is a stable condition characterizing that particular geometry, in case of clear bottom.

An explanation could be that the roughness formed by the sediments deposits allows the jet to roll over it and to go more directly towards the outlet channel; the influence of the bottom roughness opposes to the "Coanda force" that tries to deflect the jet toward the near wall.

This result shows that not only the velocity flow field strongly affect the distribution of sediments deposits, but also, in some cases, the presence of sediments, creating a time evolving bottom

roughness, can affect and change the flow patterns, giving raise to a feedback of sediments on the flow field.

For the L-R configuration, from clear-water experiments it results that the flow pattern with two recirculation zones L– R(0) is unstable. Any small perturbation in the flow leads to the formation of the L– R(1) flow pattern, which is indeed stable. On the contrary, for tests with sediment supplying, the stable flow pattern was the L– R(0) type . Numerical simulations with WOLF 2D, presented hereafter, allowed to investigate whether this change is due to the increase in bottom roughness caused by sediments deposits or more probably to a turbulence damping effect caused by suspended load, as it will be explained in chapter 6.

In the intermediate configuration C –R (Figure 4. 13d) the jet is deflected towards the exit, without reattachment points on the lateral walls. In this case, the main jet can reach directly the exit of the reservoir, without impinging on the downstream wall, like for the L –R(0). Two eddies of different size develop at both sides of the main jet. This type of flow pattern is stable, in the sense that even if the flow is disturbed, the two recirculation zones remain.

4.5.2 Sediments deposits

The maps of sediments deposits thickness s, normalized to reservoir water depth h, after 4 hours of sediment supplying are shown in Figure 4. 14.

From the comparison between the velocity maps and the corresponding sediments deposits maps, it is clear that the higher deposits thickness is located along the main jet path. It means that the jet velocity is not sufficient to keep the larger sediment particles in suspension, so they settle along the path. Their sedimentation gives rise to bed forms, clearly visible from the sediment thickness peaks recorded by the laser. These peaks in the bed forms are in good agreement with the peaks of velocity recorded by UVP after 4 hours of experiment: where sediments thickness is higher, there is a local increase of velocity, due to the reduced cross section. The maximum height of sediments deposits is about 40 mm. On the contrary, in the recirculation zones the sediments thickness is much

smaller, with values of about 5 mm at the centre of the eddies. This fact means that the water-sediments mixture exchange between the main jet and the recirculation zones is relatively low. Only few sediments are driven into the recirculation zones by turbulent mixing between the main jet and the recirculation zones. Moreover, the main part of the sediments can settle down before reaching the core of the eddies.

This result is different if compared to the tests with sediments carried out by Dufresne et al. (2010b) and Stovin and Saul (1994). In these cases, the sediments tend to deposit in the core of the eddies, where velocities are lower. Nevertheless, the location of sediments deposits strictly depends on the experimental combination of transport capacity (hydraulic parameters, sediments characteristics and consequent critical bed shear stress) and sediments supplying rate. For example, in the experiments of Dufresne et al. (2010b), the main mechanism of transport of the solid material was bed load. The transport capacity along the main inflowing jet was higher than the sediment supply, so the material could not deposit along the main jet, while it settled down in the core of the eddies, where velocity, and consequently bed shear stress, were lower.

On the contrary, the present experiments showed that the dominant process in the reservoir is deposition of the inflowing suspended load, without any significant re-suspension or bed transport. The reason is that the inflowing solid discharge is much higher than the transport capacity of the flow (see paragraph 3.4.2).

An interesting development of this investigation could be the analysis of the flow field developing in a configuration having the inlet channel at the centre of the upstream side, while the outlet channel placed near a corner of the downstream side. According to the used symbols, it would be called SX – C. In fact, even if this configuration would have the same degree of asymmetry (between the position of the two channels) of the d) C – DX configuration, it cannot be said a priori if the flow pattern is similar to the C – DX configuration (with the main jet linking directly the inlet with the outlet, following the shortest path through the reservoir) or if it takes the shape of the SX – DX configuration with clear bottom (that is to say, a main jet deflected towards the nearer wall). In

other words, maybe the proximity of the lateral wall could have an influence on the flow field, governing the kind of flow field, instead of the degree of asymmetry in the location of the channels.

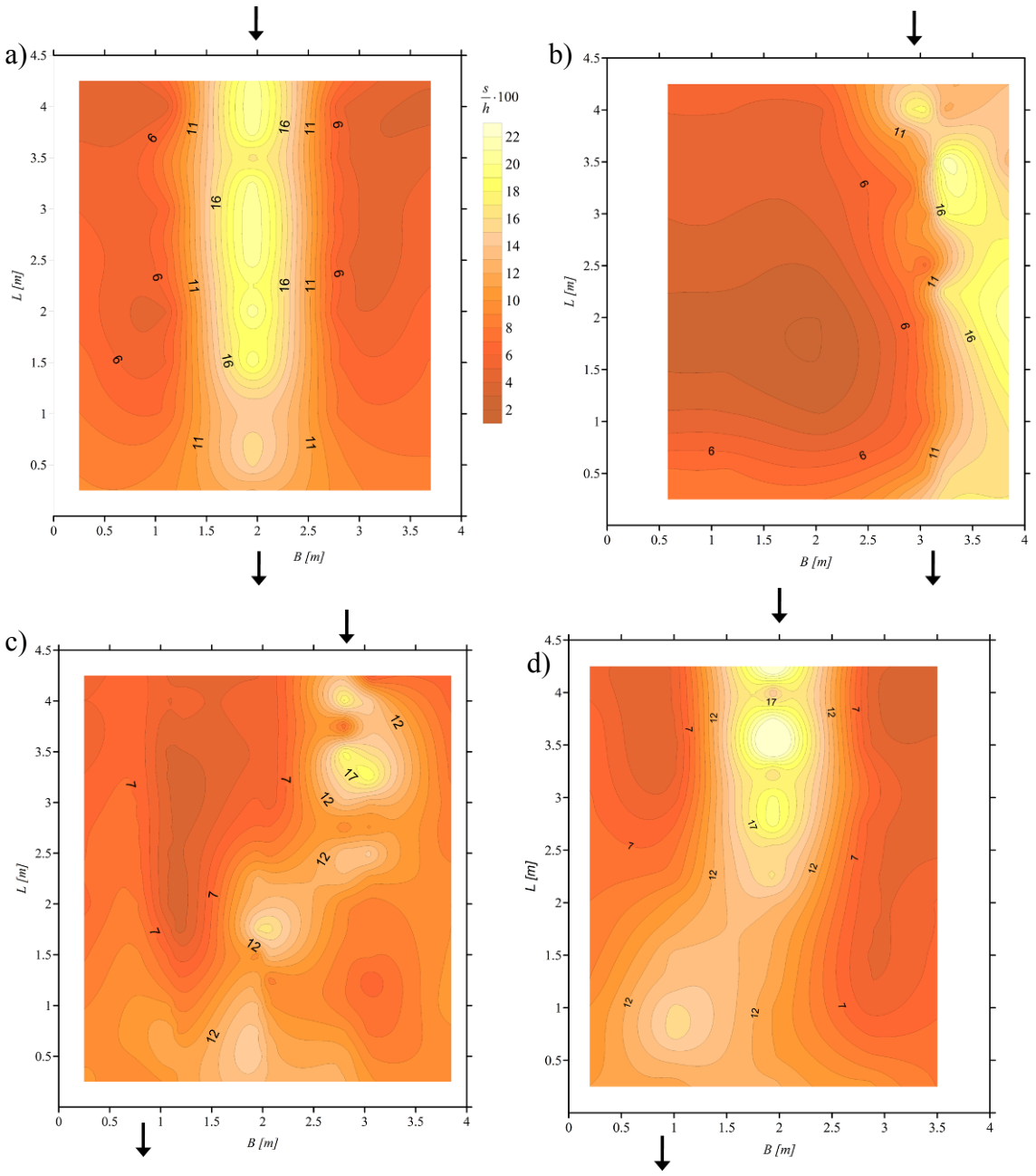

Figure 4. 14 – Sediments thickness on reservoir bottom normalized to water depth after 4 hours of experiments a) C -C b) L - L c) L – R d) C –R.

4.5.3 Trapping efficiency

As already said, the tests with different locations of the inlet and outlet channel and sediments supplying were carried out mainly with the purpose to asses if the position of the channels influences the trapping efficiency *TE* of the reservoir.

Trapping efficiency is defined as the ratio between the volume of sediments trapped in the reservoir and the total sediments volume inflowing in the reservoir in a given time interval. In general it is a time evolving quantity, because for a reservoir subjected to a constant inflow and outflow, which is progressively being filled up with settling sediments, *TE* decreases with time. This is caused by the reduction in the available reservoir volume, which increases the average velocity in the reservoir, and consequently it is possible that more solid particles are kept in suspension. Then, if velocity reaches a value able to re-suspend deposited particles, an equilibrium condition is achieved between the quantity of re-suspended and settling particles.

In the present case, trapping efficiency was calculated for every of the 4 tested reservoir configurations after 2 and 4 hour of experiments and it showed to keep a constant value: this means that the reservoir is in a phase during which it gets filled up progressively by sediments at a constant rate. In fact, the dominant process in the reservoir during the tests is deposition, without significant erosion nor re-suspension of particles.

Two methods were used to calculate trapping efficiency, leading to two values TE_1 and TE_2:

- TE_1 was calculated on the basis of the difference between the inflowing solid concentration $C_{in}(t)$ and the outflowing solid concentration $C_{out}(t)$ recorded by the turbidity-meters during the whole duration t of the experiment, as already said in paragraph 3.3.3, according to the formulation 3.11.
- TE_2 was calculated on the basis of laser sediments deposits thickness measurements. First, sediments deposits thickness was integrated on the entire reservoir bottom, in order to obtain the volume of deposited sediments W_{dep}. Then, this volume was converted into sediments deposits weight by the bulk density of sediments deposits (ρ_{dep} = 300 kg/m^3), obtained by

sampling of undisturbed deposits samples. In the end, the weight of the deposited sediments can be compared with the total solid weight inflowing in the reservoir (200 kg) during 4 hours of experiments:

$$TE_2 = \frac{W_{dep} \cdot \rho_{dep}}{Q_s \cdot 4 \cdot 3600} \qquad (4.8)$$

It has to be underlined that sediments deposits in undisturbed conditions on the bottom of the reservoir, when it is still filled by water, are characterized by a bulk density ρ_{dep} strongly different from the bulk density of dry sediments, since undisturbed deposited sediments can have a high water content, up to 80 % (Koelzer and Lara, 1958). Samples of undisturbed sediments deposits were taken and weighted; then, they were dried and weighted again, in order to find the solid content in a given volume of deposits.

Table 4. 6 – Trapping efficiencies calculated for the tested reservoir configurations. TE_1 = trapping efficiency from turbidity-meters measurements. TE_2 = trapping efficiency from sediments deposit thickness measurements.

	TE_1	TE_2
a) C-C	0.67	0.62
b) L-L	0.54	0.5
c) L-R	0.56	0.58
d) C-R	0.58	0.62

From the data presented in Table 4. 6, it results that the location of the channels has not a significant influence on trapping efficiency for the tested duration. The differences between the calculated quantities can be attributed mainly to the large measurements uncertainties. Nevertheless, it seems that the higher trapping efficiency is associated to the C-C configuration, while the L– L configuration is characterized by the lower trapping efficiency.

4.5.4 Conclusions

Velocity fields in clear water conditions and during tests with an inflowing suspended load were measured by UVP for four rectangular reservoir geometries having different locations of inlet and outlet channels. The pattern of the main inflowing jet and the presence of large scale horizontal turbulent structures were identified. Sediments deposits thickness after 2 and 4 hours of suspended sediments supplying were measured by a laser technique. The experimental conditions correspond to R_{in} = 112'000, F_{in} = 0.1 and to a non-dimensional depth h/b = 0.8. Sediments mainly settle along the path of the main water jet, while only a small amount of sediments settle in the recirculation zones. It has been possible to observe that sediment deposits location strongly depends not only on the flow patterns, but also that in some cases an increased bottom roughness, or, more probably, the simple presence of suspended load can modify the flow field.

The trapping efficiency seems not to be much influenced by inlet and outlet position (TE = 0.5 ÷ 0.65) for the utilized crushed walnut shells. Nevertheless, sediments characteristics, combined with the experimental hydraulic conditions and the sediment supply rate, strongly influence the distribution of sediments deposits.

CHAPTER 5

NUMERICAL MODELLING

Simulations of the flow patterns for the reservoir configurations which had been experimentally studied, have been carried out by the numerical model WOLF2D. This model has been developed for years at Liège University (ULg) by the H.A.C.H. (Applied Hydrodynamics and Hydraulic Constructions Group) research group and it has already been successfully applied to solve many problems, in the field of applied engineering projects and of scientific research. WOLF2D is still developing, by the addition of new features and functions; for example, in the framework of this thesis a new module to simulate suspended sediments transport and deposition was implemented, adding equations for the evolution of the mobile bottom, a transport capacity law, a settling velocity law and a transport equation for suspended sediments.

5.1. The numerical model

5.1.1 Fundamental equations

The academic code WOLF 2D developed at University of Liege WOLF2D is a depth-averaged model, well suited to represent shallow waters problems, that is to say situations in which the vertical velocity component is negligible with respect to the horizontal ones. The model solves the shallow-water equations, the so called De Saint-Venant equations, for momentum conservation and the continuity equation for mass conservation:

- Mass-conservation equation: $\frac{\partial h}{\partial t}+\frac{\partial uh}{\partial x}+\frac{\partial vh}{\partial y}=0$ (5.1)

- Momentum equation in the *x* direction:

$$\frac{\partial uh}{\partial t}+\frac{\partial u^2 h}{\partial x}+\frac{\partial uvh}{\partial y}+\frac{g}{2}\frac{\partial h^2}{\partial x}=-gh\frac{\partial z_b}{\partial x}+ghJ_x+\frac{\partial h\overline{\tau_{xx}}}{\partial x}+\frac{\partial h\overline{\tau_{xy}}}{\partial y} \qquad (5.2)$$

- Momentum equation in the *y* direction:

$$\frac{\partial vh}{\partial t}+\frac{\partial uvh}{\partial x}+\frac{\partial v^2 h}{\partial y}+\frac{g}{2}\frac{\partial h^2}{\partial y}=-gh\frac{\partial z_b}{\partial y}+ghJ_y+\frac{\partial h\overline{\tau_{yx}}}{\partial x}+\frac{\partial h\overline{\tau_{yy}}}{\partial y} \qquad (5.3)$$

Where: h = water depth;

t = time;

x, y = horizontal coordinates, transversal and longitudinal;

g = acceleration of gravity;

z_b = elevation of the bottom from a zero reference level;

J_i = component of the friction slope along the i direction;

τ_{ij} = tangential stresses;

u, v = average velocity components.

It must be remembered that the velocity u, v are depth averaged velocity which derive from the so called Reynolds decomposition, as shown in the paragraph 4.2.1.

Due to this averaging method the equations (5.1 – 5.3) are called RANS equations, that is to say Reynolds-averaged Navier Stokes equations. In fact, these equations derive from the integration along the vertical direction z of the Navier-Stokes equations for an incompressible fluid.

The turbulent stresses τ_{xy}, τ_{xx}, τ_{yy}, are expressed following the Boussinesq's approximation (which links the turbulent stresses to the average velocities of the fluid, by means of the turbulent viscosity ν_T) transposed for a depth-averaged model:

$$\frac{\partial h\overline{\tau_{xx}}}{\partial x}+\frac{\partial h\overline{\tau_{xy}}}{\partial y}=\frac{\partial}{\partial x}\left[h(\nu+\nu_T)\left(\frac{\partial u}{\partial x}-\frac{\partial v}{\partial y}\right)\right]+\frac{\partial}{\partial y}\left[h(\nu+\nu_T)\left(\frac{\partial v}{\partial x}+\frac{\partial u}{\partial y}\right)\right] \qquad (5.6)$$

$$\frac{\partial h\overline{\tau_{yx}}}{\partial x}+\frac{\partial h\overline{\tau_{yy}}}{\partial y}=\frac{\partial}{\partial y}\left[h(\nu+\nu_T)\left(\frac{\partial v}{\partial y}-\frac{\partial u}{\partial x}\right)\right]+\frac{\partial}{\partial x}\left[h(\nu+\nu_T)\left(\frac{\partial v}{\partial x}+\frac{\partial u}{\partial y}\right)\right] \qquad (5.7)$$

These expression for the turbulent stresses introduces a new unknown of the problem: the eddy viscosity ν_T, which must be defined adopting a specific turbulence closure model. For the

evaluation of the eddy viscosity ν_T, two different approaches have been compared in this study: the Fisher model and the *k-ε* model, in the modified version implemented in WOLF2D.

5.1.2 Turbulence closure 1: the Fisher model

The Fisher model is a simple algebraic turbulence closure, also called as zero-equation model. The eddy viscosity is simply defined as:

$$\nu_T = \alpha\, h\, U^*, \qquad (5.8)$$

where $U^* = \sqrt{\frac{\tau_w}{\rho}}$ (5.9)

is the friction velocity, due to the tangential stress on the bottom τ_w, while α is an empirical coefficient whose values are in the range 0.5 – 2. For the present work, the coefficient $\alpha = 1$ has been adopted, since previous research in this field had shown that this was the more suited value (Dewals et al., 2008).

5.1.3 Turbulence closure 2: the WOLF2D k-ε model

Second, a two equations turbulence model, the depth-integrated *k-ε* model, with two different length-scales accounting for vertical and for horizontal turbulence mixing has been applied in the simulations, as developed by Erpicum (Erpicum et al., 2009). This model is based on the classical three dimensional *k-ε* model of Launder and Spalding, but it has been modified in order to adapt to shallow water flows.

The *k-ε* model is normally formed by two transport equation, one for the turbulent kinetic energy *k*, and one for the rate of viscous dissipation *ε*, which are solved together with the continuity equations and the momentum equations of the flow at every time step.

It must be underlined that in the depth integrated *k-ε* model implemented in WOLF2D, a depth integrated turbulent kinetic energy for large scale turbulence appears:

$$k' = \frac{\overline{u'u'h} + \overline{v'v'h}}{2} \qquad (5.10)$$

instead of the classical turbulent kinetic energy

$$k = \frac{\overline{u'u'} + \overline{v'v'}}{2} \qquad (5.11).$$

Also the energy dissipation is depth integrated, and it assumes the form

$$\varepsilon' = \nu * \left[\overline{(\frac{\partial \boldsymbol{u'h}}{\partial \boldsymbol{x}})^2} + \overline{(\frac{\partial \boldsymbol{v'h}}{\partial \boldsymbol{y}})^2} + \overline{(\frac{\partial \boldsymbol{u'h}}{\partial \boldsymbol{y}})^2} + \overline{(\frac{\partial \boldsymbol{v'h}}{\partial \boldsymbol{x}})^2} \right] \qquad (5.12)$$

The global eddy viscosity ν^* that appears in the equation, is given by the sum between the molecular eddy viscosity of the fluid ν, that is responsible for the molecular dissipation, and the three dimensional eddy viscosity $\nu_{T,3D}$, which models the effect of dissipation caused by the small scale isotropic turbulence. This effect is linked to the friction velocity, since the small scale turbulence is actually generated by wall friction, as it can be seen in Equation (5.14).

$$\nu^* = \nu + \nu_{T,3D} \qquad (5.13)$$

$$\nu_{T,3D} = c_\nu h U^*, c_\nu = 0.08 \qquad (5.14)$$

So, the two additional transport equations are the following:

- Transport equation for *k'*:

$$\frac{\partial k'}{\partial t} + \frac{\partial uk'}{\partial x} + \frac{\partial vk'}{\partial y} = \frac{\nu *}{h}\frac{\partial^2 k' h}{\partial x^2} + \frac{\nu *}{h}\frac{\partial^2 k' h}{\partial y^2} + \frac{\partial}{\partial x}\left[\frac{\nu_{T,2D}}{\sigma_k}\frac{\partial k'}{\partial x}\right] + \frac{\partial}{\partial y}\left[\frac{\nu_{T,2D}}{\sigma_k}\frac{\partial k'}{\partial y}\right] - k'\frac{\partial u}{\partial x} - k'\frac{\partial v}{\partial y} + P' - F' - \frac{\varepsilon'}{h} \qquad (5.15)$$

- Transport equation for ε':

$$\frac{\partial \varepsilon'}{\partial t} + \frac{\partial u\varepsilon'}{\partial x} + \frac{\partial v\varepsilon'}{\partial y} = \frac{\nu *}{h}\frac{\partial^2 \varepsilon' h}{\partial x^2} + \frac{\nu *}{h}\frac{\partial^2 \varepsilon' h}{\partial y^2} + \frac{\partial}{\partial x}\left[\frac{\nu_{T,2D}}{\sigma_\varepsilon}\frac{\partial \varepsilon'}{\partial x}\right] + \frac{\partial}{\partial y}\left[\frac{\nu_{T,2D}}{\sigma_\varepsilon}\frac{\partial \varepsilon'}{\partial y}\right] + c_{1\varepsilon}\frac{\varepsilon'}{k'}\left[P' - (1 - c_{3\varepsilon})F'\right] - c_{2\varepsilon}\frac{\varepsilon'^2}{hk'} \qquad (5.16)$$

where the term concerning the production of the large scale horizontal turbulence *P'* and the term concerning the effect of wall friction *F'* (the Manning's friction law is applied) are given by the following expressions:

$$P' = \nu_{T,2D}\left[\left(\frac{\partial uh}{\partial x} - \frac{\partial vh}{\partial y}\right)\left(\frac{\partial u}{\partial x} - \frac{\partial v}{\partial y}\right) + \left(\frac{\partial uh}{\partial y} + \frac{\partial vh}{\partial x}\right)\left(\frac{\partial u}{\partial y} + \frac{\partial v}{\partial x}\right)\right] \qquad (5.17)$$

$$F' = \frac{gn^2}{h^{4/3}}\left[3k'\sqrt{u^2+v^2} - \nu_{T,2D}\frac{\left(\frac{\partial uh}{\partial x}-\frac{\partial vh}{\partial y}\right)\left(u^2-v^2\right)+2\left(\frac{\partial uh}{\partial y}+\frac{\partial vh}{\partial x}\right)uv}{\sqrt{u^2+v^2}}\right] \qquad (5.18)$$

where *n* is the Manning roughness coefficient.

The *P'* term is linked to the gradients of horizontal velocity and to the two dimensional eddy viscosity of the large scale structures $\nu_{T,2D.}$

The *F'* term is opposed to the turbulence production term (sign minus in the equation), so it contributes to the turbulence dissipation and has a stabilizing effect on the horizontal turbulence.

The two dimensional large scale eddy viscosity $\nu_{T,2D}$, which appears in (5.17) is defined as:

$$\nu_{T,2D} = c_\mu \frac{k'^2}{\varepsilon'} \qquad (5.19)$$

where c_μ is an empirical coefficient, for which the value $c_\mu = 0.09$ has been adopted in WOLF2D deriving it from the three dimensional reference *k-ε* model of Launder and Spalding (1972).

The values of the other constant which appear in the transport equations have been also adopted from the three dimensional k-ε model, though rigorously these values would have required a specific calibration for the new model. Anyway, these values have been confirmed by numerous authors and they can be considered with sufficient confidence universally valid. The implemented values of the constants are: $\sigma_k = 1$, $\sigma_\varepsilon = 1.3$, $c_{1\varepsilon} = 1.44$, $c_{2\varepsilon} = 1.92$, $c_{3\varepsilon} = 0.8$.

In the end, the momentum equations, when applying the *k-ε* model resumed here above, present this final form:

Momentum in the x direction:

$$\underbrace{\frac{\partial uh}{\partial t}}_{1}+\underbrace{\frac{\partial u^2h}{\partial x}+\frac{\partial uvh}{\partial y}}_{2}+\underbrace{\frac{g}{2}\frac{\partial h^2}{\partial x}}_{3}=\underbrace{-gh\frac{\partial z_b}{\partial x}}_{4}+\underbrace{\nu*\frac{\partial^2 uh}{\partial x^2}+\nu*\frac{\partial^2 uh}{\partial y^2}}_{5}\underbrace{-F_x}_{6}+$$
$$\underbrace{+\frac{\partial}{\partial x}\left[\nu_{T,2D}\left(\frac{\partial uh}{\partial x}-\frac{\partial vh}{\partial y}\right)-k'\right]+\frac{\partial}{\partial y}\left[\nu_{T,2D}\left(\frac{\partial uh}{\partial y}+\frac{\partial vh}{\partial x}\right)\right]}_{7} \qquad (5.20)$$

Momentum in the y direction:

$$\underbrace{\frac{\partial vh}{\partial t}}_{1}+\underbrace{\frac{\partial v^2 h}{\partial y}+\frac{\partial uvh}{\partial x}}_{2}+\underbrace{\frac{g}{2}\frac{\partial h^2}{\partial y}}_{3}=\underbrace{-gh\frac{\partial z_b}{\partial y}}_{4}+\underbrace{\nu*\frac{\partial^2 vh}{\partial y^2}+\nu*\frac{\partial^2 vh}{\partial x^2}}_{5}-\underbrace{F_y}_{6}+$$
$$\underbrace{+\frac{\partial}{\partial y}\left[\nu_{T,2D}\left(\frac{\partial vh}{\partial y}-\frac{\partial uh}{\partial x}\right)-k'\right]+\frac{\partial}{\partial x}\left[\nu_{T,2D}\left(\frac{\partial uh}{\partial y}+\frac{\partial vh}{\partial x}\right)\right]}_{7} \quad (5.21)$$

where:

1. is the unsteady term;
2. represents the advection term;
3. is the term which represents the spatial variation of the water depth;
4. is the term linked to the bottom spatial variation;
5. is the term that represents the effect of the viscous stresses and the stresses due to the isotropic small scale turbulence;
6. represents the friction term, whose components F_x and F_y can be expressed, according to the Manning's law, in this way:

$$ghJ_x = F_x = \frac{gn^2}{h^{1/3}}u\sqrt{u^2+v^2} \quad (5.22)$$

$$ghJ_y = F_y = \frac{gn^2}{h^{1/3}}v\sqrt{u^2+v^2} \quad (5.23)$$

7. represents the depth integrated Reynolds stresses linked to the large scale turbulence:

$$\overline{-u'u'h} = \nu_{T,2D}\left(\frac{\partial uh}{\partial x}-\frac{\partial vh}{\partial y}\right)-k' \quad (5.24)$$

$$\overline{-v'v'h} = \nu_{T,2D}\left(\frac{\partial vh}{\partial y}-\frac{\partial uh}{\partial x}\right)-k' \quad (5.25)$$

$$\overline{-u'v'h} = \overline{-v'u'h} = \nu_{T,2D}\left(\frac{\partial uh}{\partial y}+\frac{\partial vh}{\partial x}\right) \quad (5.26)$$

5.1.4 Boundary and initial conditions

The upstream boundary condition applied at the beginning of the inlet channel consists in a fixed discharge Q = 7 l/s. To facilitate the rise of the asymmetry in the flow patterns, a small linear perturbation has been applied on the inlet velocity profile: the discharge of the cell in contact with one lateral wall of the inlet channel has a discharge 2% higher than the average discharge, while the cell in contact with the opposite lateral wall has a discharge 2% lower than the average.

The standard upstream boundary condition concerning turbulence for the k-ε model has been adopted from Choi and Garcia (2002) and it is:

$$k_{in} = 10^{-4} \cdot V_{in}^{2} \qquad (5.27)$$

$$\varepsilon_{in} = 10 \cdot \frac{k_{in}^{3/2}}{h} \qquad (5.28)$$

where k_{in} and ε_{in} are the turbulent kinetic energy and the dissipation ratio at the upstream boundary of the inlet channel.

In the simulations a sensitivity analysis of the results on the turbulent boundary condition has been performed, increasing or decreasing the k_{in} value of 2 orders of magnitude, but the resulting velocity fields were not significantly influenced by this variation, except for the very proximity to the inlet channel. For example, in the case of the increased turbulence level, turbulence was immediately dissipated as soon as the water jet entered the reservoir.

In a future, also the empirical constants present in the k-ε model, in particular in the production and dissipation terms, should be modified in order to obtain a significant modification of turbulence intensity inside the reservoir. For the moment, in fact, the constants used in the model are taken from the three-dimensional k-ε model of Launder and Spalding (1972) and they are not been explicitly calibrated for the depth-averaged k-ε model implemented in WOLF.

The downstream boundary condition applied at the outlet channel is generally an imposed water height, which makes possible to have a water level in the reservoir that reproduces the performed laboratory experiments. On the contrary, in the simulations starting from an empty basin, a stage-discharge relationship is implemented, reproducing directly the overflow over the flap gate existing in the experimental setup.

About the initial conditions, some simulations have been performed starting from an empty basin, reproducing in that way the filling of the reservoir. Anyway, normally the simulations have been carried out starting from a basin with water at rest, having the required water depth (h = 0.2 m, in general). Sometimes, in order to help the development of the asymmetry of the flow field, an initial random flow field was given as initial condition, but after some iteration the flow field regained its true shape, guaranteeing the independency of the result from the initial condition.

5.1.5 Summary of the other features of the model

The numerical discretization implemented in WOLF2D relies on a finite volume scheme, applied on multiblock structured grids.

The reconstruction of the variables at cells interfaces is either constant or linear, combined with a slope limiter, leading in the latter case to a second-order spatial accuracy.

The fluxes are computed by a self-developed Flux Vector Splitting (FVS) method, in which the up-winding direction of each flux is simply dictated by the sign of the flow velocity re-constructed at the cell interfaces (Erpicum et al., 2010a). A “Von Neumann” stability analysis has demonstrated that this FVS leads to a stable spatial discretization, while requiring low computational cost. FVS has the advantage of being Froude-independent and of facilitating a satisfactory adequacy with the discretization of the bottom slope term.

The turbulent fluxes are simply evaluated by means of a centred scheme.

The time integration adopted for the simulations performed for this thesis is a 3-step first-order accurate Runge-Kutta algorithm.

A semi-implicit treatment of the bottom friction term was used, without requiring significant additional computational cost.

For the simulations which start from an empty basin, wetting and drying of cells respects the continuity equation at each time step, by an iterative procedure. A grid adaptation technique restricts the simulation domain to the wet cells.

This finite volume scheme has already proven its validity and efficiency for the analysis of flow in shallow reservoirs (Dewals et al., 2008; Dufresne et al., 2011) as well as numerous other applications including complex turbulent flows (Erpicum et al., 2009; Roger et al., 2009) and geophysical flows (Dewals et al. 2011; Ernst et al., 2010; Erpicum et al., 2010a and b).

5.2. The suspended sediments transport module

Numerical simulations with an inflowing suspended load for different reservoir configurations characterized by different positions of the inlet and outlet channel were performed in order to reproduce the thickness of the sediment deposit on the reservoir bottom resulting from experiments carried out for 4 hours with the same inflowing solid discharge (Q_s = 0.014 kg/s – Cv_{inlet}= 0.132%).

The model for suspended solid transport, added to the software WOLF2D, is formed by the following equations:

- Evolution of the bottom:

$$(1-p)\cdot\frac{\partial z}{\partial t} = -(E-D) \qquad (5.29)$$

where E is the erosion, D is the deposition, p is the porosity of the deposited sediments, and the difference E-D, that is the sediments exchange flux, can be expressed in the following way:

$$E - D = \alpha_{adap} v_{ss} (\overline{C} - C_T) \qquad (5.30)$$

- α_{adap} is an adaptation coefficient, for which various empirical expression have been proposed (Wu, 2008), but that, as a first approximation can be considered also as a constant coefficient;
- v_{ss} is the settling velocity as discussed in Chapter 3 and given by the formulation (3.15);
- $\overline{C}$ is the average concentration of suspended solids;
- C_T is the equilibrium concentration of suspended solids, the so called capacity transport of (5.33);

❖ Convection-diffusion of concentration (depth integrated):

$$\frac{\partial h\overline{C}}{\partial t}+\frac{\partial hu\overline{C}}{\partial x}+\frac{\partial hv\overline{C}}{\partial y}=\frac{\partial(h\varepsilon_s\frac{\partial C}{\partial x})}{\partial x}+\frac{\partial(h\varepsilon_s\frac{\partial C}{\partial y})}{\partial y}+E-D \qquad (5.31)$$

where ε_s is the diffusivity of the sediments that is calculated in the model in this way:

$$\varepsilon_s=\alpha_s\cdot\boldsymbol{h}\cdot\boldsymbol{U}^*, \qquad (5.32)$$

where α_s is the turbulent coefficient for sediments, which is empirically calibrated, in analogy with the turbulent coefficient for the fluid of the Fisher model (paragraph 5.1.2).

❖ Capacity transport law (Celik and Rodi, 1991): $C_T=\beta\cdot\frac{\tau_w}{(\rho_s-\rho)\cdot g\cdot h}\cdot\frac{V}{v_{ss}}$ (5.33)

where β is an empirical coefficient (value suggested by Celik and Rodi: 0.034), V is the velocity of the flow in the cell, τ_w is the wall friction ($\tau_w = 0.5*c_f*\rho*V^2$).

This suspended sediments transport module has been tested in the framework of this thesis, trying to reproduce the sediments deposits thickness on the bottom of the experimental reservoir of EPFL, after 4 hours of sediments supplying. The results of the first preliminary simulation, by which the sensitivity of the model to the variation of its parameters have been investigated, are referred in Chapter 6.

CHAPTER 6

RESULTS OF THE SIMULATIONS

The first part of this chapter is dedicated to verify that the numerical model is able to reproduce the flow patterns found in the experiments for the different tested geometrical and hydraulic boundary conditions, obtaining in this way a further validation of the numerical code. The turbulence closure model adopted for these simulation has been the depth-averaged k-ε model available in WOLF2D, since it leads to results closer to the experimental ones. The reservoir kinetic energy, a global index developed expressly in the framework of this thesis (see Chapter 4), has been adopted to evaluate the performance of the turbulence model in reproducing the experimental results.

Then, the flow fields developing for other reservoir configurations and hydraulic conditions, yet not tested experimentally, were simulated, in order to extend the domain of investigation.

Simulations with suspended sediments entering the reservoir were also carried out, after the verification that the model was able to reproduce the flow patterns found in the experiments with asymmetric inlet and outlet position and clear water. Then, the aim of the simulations with suspended load was to test the ability of the new implemented suspended sediments transport module to reproduce the distribution of the deposits on reservoir bottom found in the experiments and, finally, the global trapping efficiency of the reservoir.

6.1. Flow patterns in rectangular shallow reservoirs

6.1.1 Qualitative comparison

First of all, it has been checked that the flow patterns types observed in the physical experiments correspond qualitatively to the numerically simulated flow fields.

The flow patterns types found in the experiments and the correspondent simulated flow patterns types are indicated in Table 6.1. The numerical model, with the depth-integrated k-ε turbulence

closure, generally succeeded well in reproducing the same flow field type of the experiments, except for the S1 flow fields. In fact, the numerical model produces, for the tested reservoir configurations, only S0 flow fields; it means that the numerical model is not able to reproduce the two small upstream eddies, which in fact are characterized by very small velocities, but whose presence is well assessed in the experiments. Moreover, the k-ε model forecasts an A2 flow field for the 6x1m reservoir, while experiments showed the existence of an A1 flow pattern: anyway, this fact can be justified by the proximity of this configuration to the transition between the A1 and the A2 flow pattern. Another similar problem happens with the largest configuration, that is the 6x4m reservoir: also in this case, the k-ε model forecasts an S0 flow field, while experiments had shown that for this reservoir configuration the asymmetric flow field A1 is the stable solution. Also in this case, the problem is the proximity to the transitional zone. In fact, it has been assessed that, for reservoir configurations having length L = 7 m and B = 4 m the flow field developing in the WOLF2D simulations is A1, as from experimental evidence. So, it means that in the actual k-ε model the band which identifies the transitional zone (see Figure 6. 6) is probably slightly translated towards the right. In a future, maybe the modification of the empirical constants of the depth-averaged k-ε model could lead to results closer to the experimental findings.

6.1.2 Velocity profile comparison

Besides of a qualitative observation of the streamlines concerning the experiments and the numerical simulations a more detailed comparison between the velocity fields forecast by the k-ε model of WOLF2D and the experimental results, was made by analysing the differences between the longitudinal velocity profiles in different cross-sections of the reservoir. An example of the comparison between these velocity profiles is given in Figure 6. 1, on the 4 reservoir configurations chosen as reference of the 4 main types of flow patterns observed; as it can be seen from Figure 6. 1 the correspondence between experimental and numerical results is in general satisfactory.

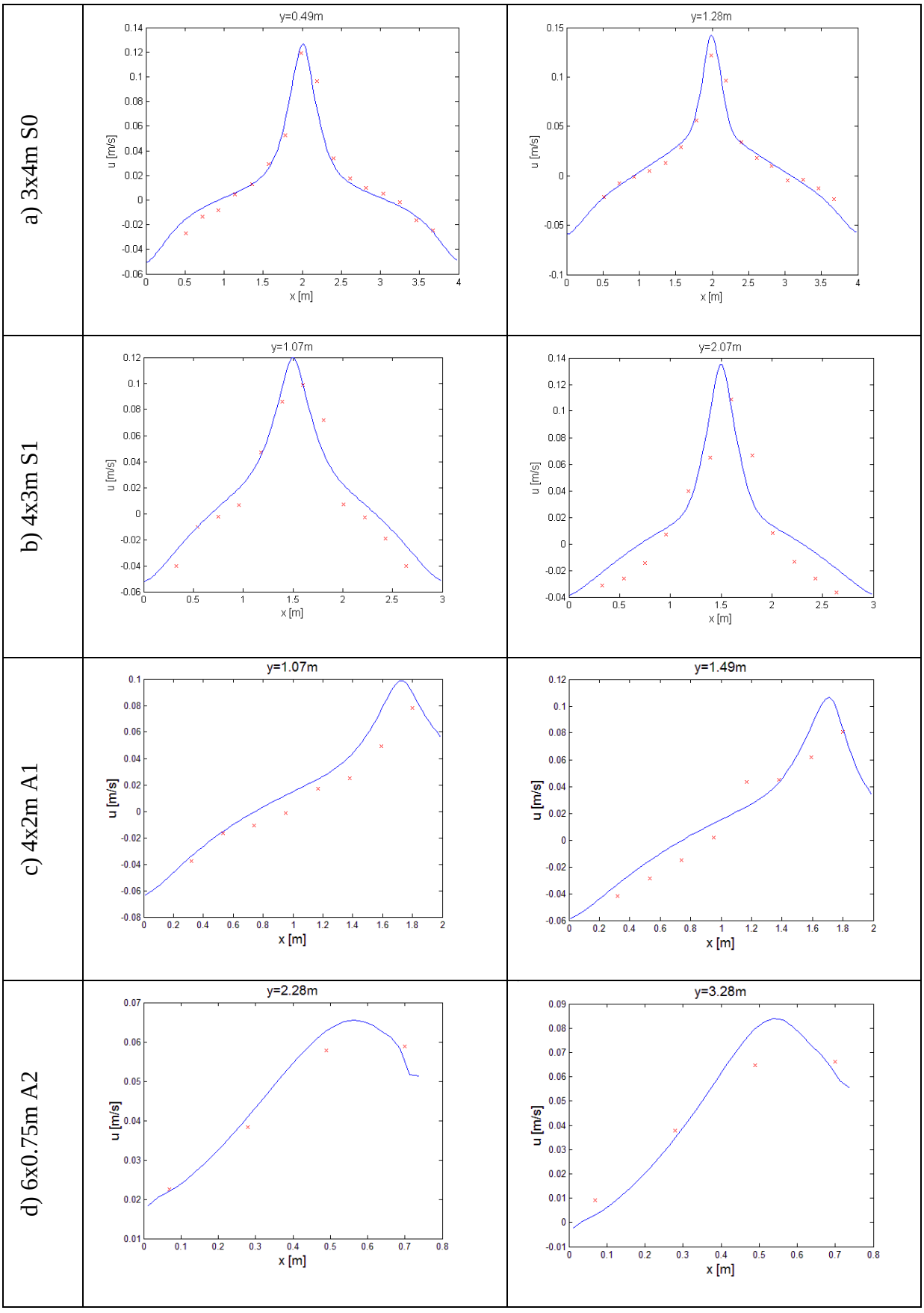

Figure 6. 1- Velocity profiles at different cross-sections of the reservoir. Blue line: numerical results; red points : experimental results.

6.1.3 Reservoir kinetic energy comparison

The calculated quantities for every tested reservoir configuration, concerning the experimental tests and the numerical simulations are shown in Table 6.1.

Table 6. 1 – Global value of total kinetic energy, experimental and numerical, and specific value of kinetic energy for unit area, E_{k_unit}

L [m]	B [m]	Experimental flow pattern	Simulated Flow Pattern	E_{k_tot} [m^4/s^2]	$E_{k\_tot\_k\text{-}\varepsilon}$ [m^4/s^2]	ΔE_{k_tot} [%]
6	4	A1	S0	0.015	0.0153	2
5.8	4	S1	S0	0.014	0.013	-14
5.8	4	A1	S0	0.015	-	-
5.3	4	S1	S0	0.014	0.0132	-6
5	4	S1	S0	0.012	0.0118	-2
3	4	S0	S0	0.008	0.0089	11
4	3	S1	S0	0.01	0.0093	-7
4	2	A1	A1	0.007	0.0081	16
4	1	A1	A1	0.005	0.0039	-22
6	1	A1	A2	0.006	0.0068	13
6	0.75	A2	A2	0.0049	0.0063	29
6	0.6	A2	A2	0.006	0.0063	5

The percentage deviation between the two values of total energy content (the experimental one and the numerical one), normalized to the experimental value $E_{k\_tot,}$ was calculated, in order to assess the global capability of the model to reproduce the velocity field of the reservoir, according to the following equation:

$$\Delta E_{k\_tot} = \frac{E_{k\_tot\_k-\varepsilon} - E_{k\_tot}}{E_{k\_tot}} \cdot 100 \qquad (6.1)$$

From Table 6.1 it can be seen that the discrepancy between the energetic content calculated by WOLF2D and the energetic content deriving from experiments is on average about 10%. In some cases the correspondence is very good, 2%, and only one case (reservoir 6x0.75m) reaches nearly a difference of 30% between numerical and experimental results.

It must be noted that the analysis of the total kinetic energy reservoir content has been used to evaluate which turbulence closure was the one which reproduce in the best way the experimental results. According to the calculated values of total reservoir kinetic energy, the k-

ε model revealed to be much more suited to represent the experimental results (see Figure 6. 2). In fact, also if we consider qualitatively the velocity maps produced by both the turbulence models (Figure 6. 3), we can observe that the Fisher model forecasts a much wider diffusion of the jet with respect to the flow field forecast by the k-ε model.

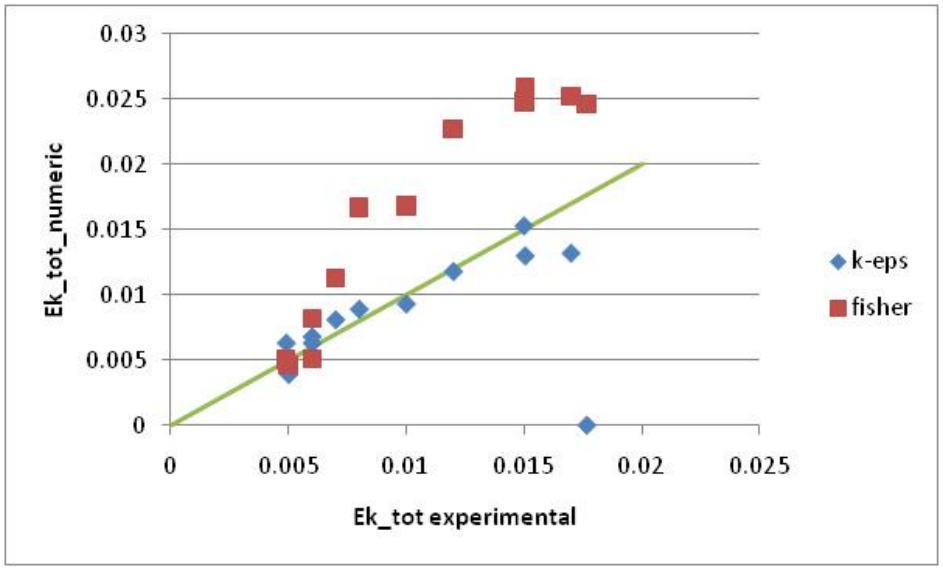

Figure 6. 2– Comparison between the total kinetic energy calculated by the k-ε model and by the Fisher model

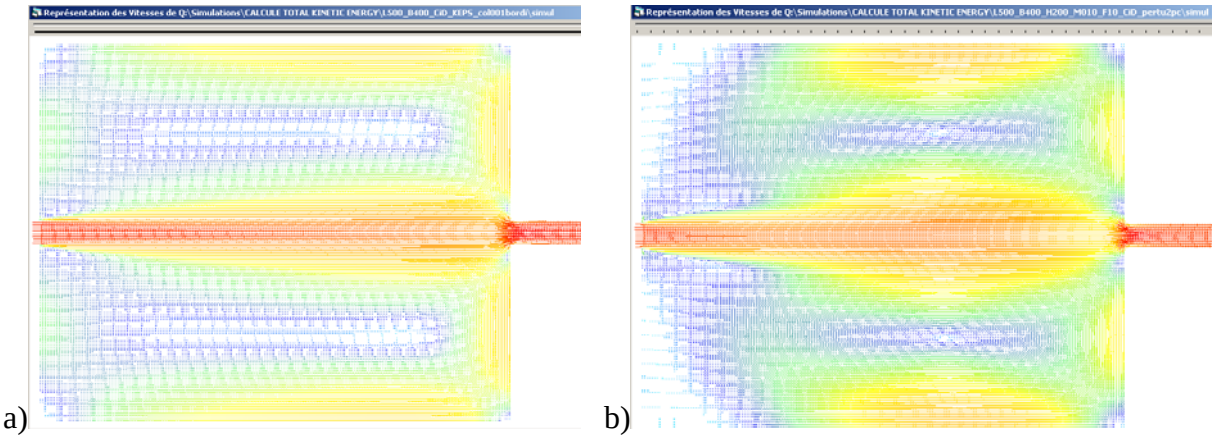

Figure 6. 3– Top view of the flow fields simulated by WOLF2D for a 5.5x4 m reservoir configuration. Left figure: k-ε model. Right figure: Fisher model

6.1.4 Turbulence analysis

A turbulence analysis was performed for the four reference geometries, cited in the paragraph 4.2.1. The experimental values of k were compared to the k values derived from the k-ε numerical model implemented in WOLF. Since the model provides the depth integrated value $k \cdot h$, the model output has been simply divided by the water height h to obtain the usual form of turbulent kinetic energy k.

In Figure 6. 4 and Figure 6. 5, the experimental and the numerical k profiles for different cross sections of the four reservoir configurations are shown. Along the main jet the experimental values match reasonably well the turbulence values resulting from the numerical model. On the contrary, the turbulence in the recirculation zones, outside of the main jet, is usually significantly overestimated by the numerical model. The average ratios between the computed k values k_{num} and the values resulting from the experiments k_{exp} are shown in Table 6.2, for each reservoir configuration.

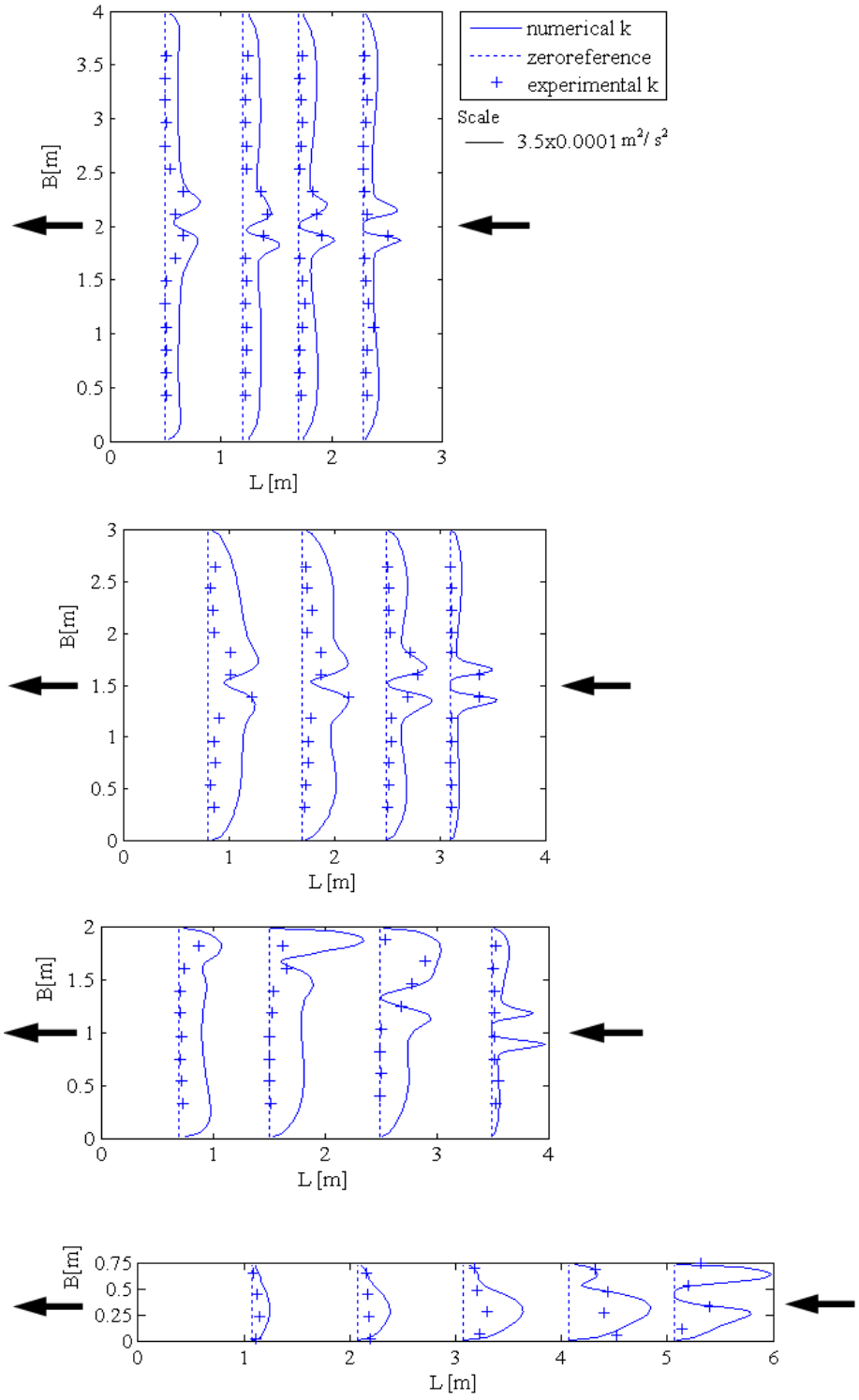

Figure 6. 4– Turbulent kinetic energy *k* for different types of flow patterns: a) *L* = 4 m *B* = 3 m , 4 eddies symmetric flow pattern S1 – b) *L* = 3 m *B* = 4 m, 2 eddies symmetric flow pattern S0 – c) *L* = 4 m *B* = 2 m, asymmetric flow pattern A1 – d) *L* = 6 m *B* = 0.75 m, asymmetric flow pattern A2.

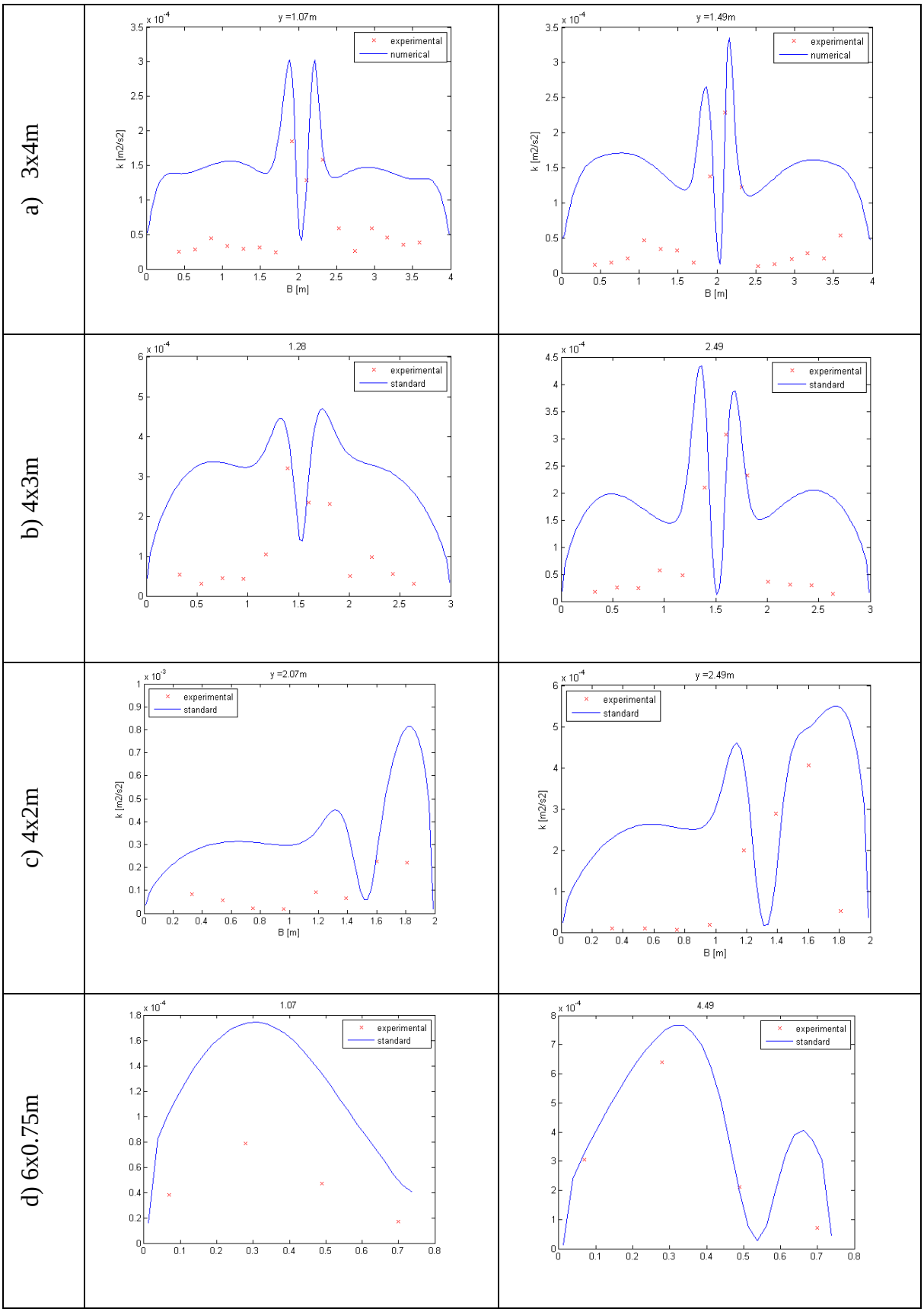

Figure 6. 5– Experimental and numerical values of turbulent kinetic energy *k* at different cross sections along the reservoir, for the four reservoir configurations chosen as reference

Table 6.2 – Average ratio between the *k* value calculated by the numerical model and the experimental value.

L [m]	3	4	4	6
B [m]	4	3	2	0.75
k_{num}/k_{exp}	3.03	2.63	4.53	3.09

6.2. Numerical tests of new geometries

Some new reservoir geometries, which had not been tested experimentally, because of the inadequate size of the experimental facility, were simulated numerically by WOLF, always conserving the same hydraulic conditions (Q = 7 l/s – h = 0.2 m).

The new tested configurations are presented in Table 6.3.

Table 6. 3 – New reservoir configurations studied numerically by WOLF2D

L [m]	8	10	12	10	9	10.5	9	2
B[m]	4	4	3	2	1.5	1.5	1	3
Flow pattern type	A1	A1	A1	A1	A2	A2	A2	S0

The points representing these configurations have been added to the plot of Figure 6. 6, which summarizes all the results in terms of flow patterns classification. As it can be seen, these configurations were tested with the aim to investigate parts of the *L/B – B/b* domain that hadn't been studied before, in particular in order to add more points near the transition between the A1 and A2 flow patterns and to define better the zone of the plot corresponding to the A2 flow field.

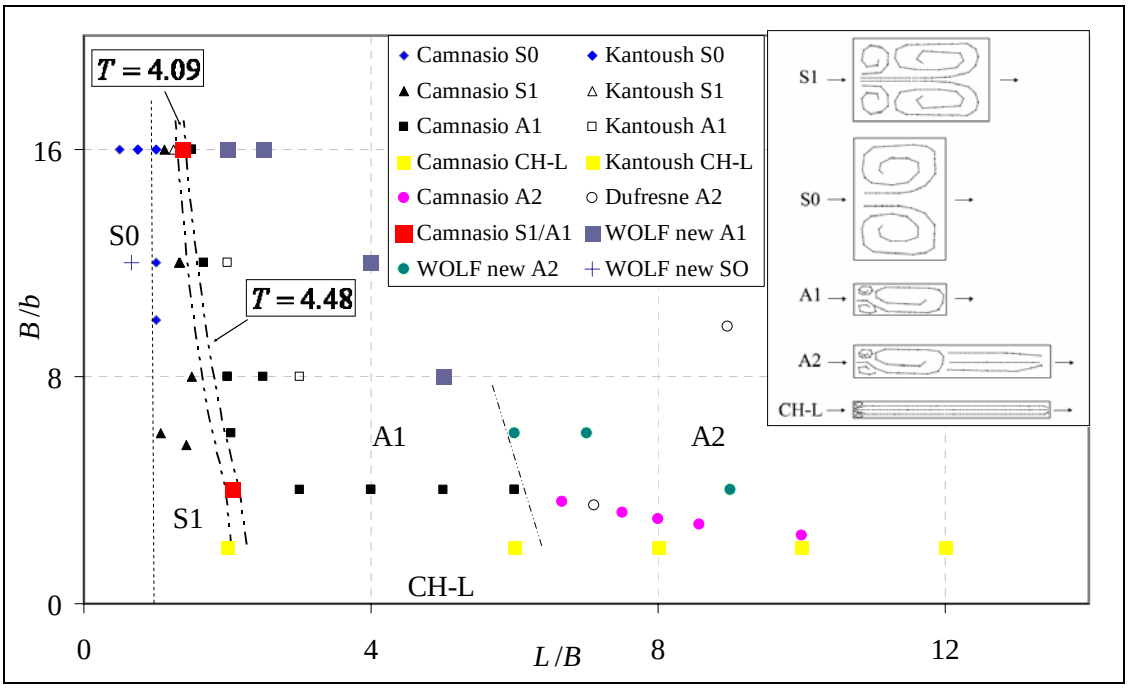

Figure 6. 6 – Flow patterns classification as a function of L/B and B/b, comprehensive of the new geometries tested by WOLF2D.

6.3. Flow patterns simulation for the asymmetric reservoir configurations

Before performing simulations with sediments supplying, the flow fields developing in the asymmetric configurations of the reservoir (see paragraph 3.4.2) have been simulated, in order to compare the results of the model with the results of experiments with clear water (see paragraph 4.5.1).

In these series of simulations, the Fisher model has been chosen as turbulence closure, since it requires less computational time and it was assessed that it lead to results sufficiently near to the experimental ones.

6.3.1 Analysis of the results

Figure 6. 7 shows the simulated flow patterns for the four tested reservoir geometries.

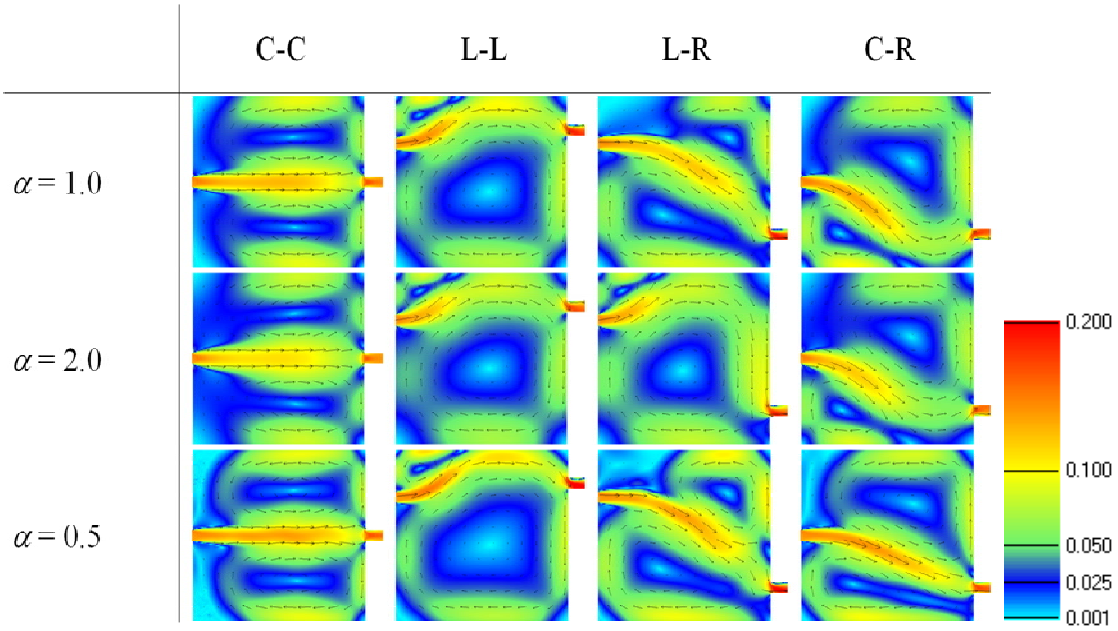

Figure 6. 7 -. Simulated velocity field (m/s) for the four inlet/outlet geometries (*L* = 4.5 m, *B* = 4 m) and three turbulence parameters (initial condition: water at rest, *h* = 0.2 m). The legend indicates velocity intensity (m/s)

In order to assess the sensitivity of the results to the turbulence parameter α of the Fisher model, simulations have been run with three different values: $\alpha = 1$, as used by Dewals et al. (2008), $\alpha = 2$ and $\alpha = 0.5$. In all the simulations, the initial condition corresponds to a basin with 0.2 m water at rest. A slightly disturbed velocity profile is utilized as inflow boundary condition, consistently with the procedure described by Dewals et al. (2008). This method introduces a small linear perturbation on the inlet velocity profile, that allows to reveal the cases in which an instability of the flow field exists. Simulations with different types of perturbation of the inlet velocity profile were performed, but they lead to the same final steady flow pattern, confirming that the slight asymmetry in the boundary condition acts only as a seed for asymmetry, without affecting the final result.

In the reference C-C configuration, the main jet is straight with two re-circulations on both sides. The flow field is essentially symmetric in spite of the seed for non-symmetry introduced through the inflow velocity profile. Like in the experimental results, the computed upstream eddies are very small and the simulated flow pattern corresponds indeed to a transition between the S1 and S0

patterns. The numerical results for C-C configuration are robust, since changing the turbulence parameter has no macroscopic effect on the predicted flow pattern, except a higher diffusion of the jet as α increases.

Consistently with the experimental findings (paragraph. 4.5.1), the computed flow field in the L-L configuration has one reattachment point on the left side-wall. This result is also robust since the simulated flow pattern does not change when the turbulence parameter is varied. The predicted reattachment length shows a limited sensitivity with respect to the turbulence parameter, since it varies by less than 5% when the turbulence parameter varies by a factor four.

In contrast, the simulations of configuration L-R lead to three macroscopically different flow patterns depending on the turbulence closure. For the highest value of α, the predicted flow pattern shows one reattachment point, which is in agreement with most experimental observations in L-R tests with clear water. When the turbulence parameter is reduced ($\alpha = 1$), the flow field macroscopically changes to a pattern without reattachment points, as experimentally obtained during tests with sediments supplying. Furthermore, comparing the numerical results with the experimental findings of tests with sediments, it can be noted that the computed jet impinges on the downstream wall approximately in the same position as found in the experiments.

Transition from one flow pattern to another does not take place continuously as α is varied but the flow patterns change discontinuously for $\alpha = 1.6 - 1.7$.

Finally, for the lowest value of α, the flow does not converge towards a steady state and the jet remains meandering between the inlet and outlet channels. It shows very regular large-scale oscillations with a period of about 21 s. The corresponding flow visualization in Figure 6. 7 is an average velocity field over 21 s.

Consequently, the numerical model has limited predictive capacity for configuration L-R, but it is able to detect the instability of the flow field, which is consistent with experiments.

In addition, the numerical model shows that the flow pattern tends to match the results of experimental tests with suspended load for reduced turbulence parameter values. This may be explained as a damping of turbulence caused by suspended sediments.

Indeed, the effects of suspended load on turbulence can become significant even for volumetric concentrations as low as 10^{-6}, as reported by Cao and Carling (2001). In the present case, sediments volumetric concentration is about $1.3 \cdot 10^{-3}$, so the presence of suspended sediments can actually affect turbulence. According to Nino and Garcia (1999), turbulence can be attenuated or enhanced depending on the size of the particles. If the Reynolds particle number $Re_p^* = \frac{U^* \cdot d}{\nu} < 2$, particle size is smaller than the Kolmogorov length scale, and turbulence is attenuated. In the present case, $Re_p^* = \frac{U^* \cdot d_{50}}{\nu} = 0.44$, so turbulent kinetic energy is reduced by the presence of the particles, since part of the turbulent energy production is used to maintain the particles in suspension, as demonstrated also by Cloutier et al. (2006). This is a case of two-way coupling between particles and flow, in the sense that not only the flow governs particles motion, but also particles have an effect on the flow.

Finally, simulations for the C-R configuration with $\alpha = 1$ and $\alpha = 2$ lead to a flow pattern with one reattachment point on the right side-wall, which was not found in the experiments. The reattachment length is hardly modified as a result of the variation of α. In contrast, when $\alpha = 0.5$, the computed flow pattern does not have any reattachment point, consistently with experimental observations.

Therefore, it may be concluded that, since the best agreement with clear-water experiments is found for configuration L-R with $\alpha = 2.0$ while for configuration C-R with $\alpha = 0.5$, the flow model fails to predict the flow patterns in all geometric configurations based on a single value of α. To this purpose, in order to avoid the dependence of the model on the manual calibration of the turbulent

parameter, it would be necessary to apply a more sophisticated turbulence model, for example the k-ε model utilized for the other simulations, even if it requires an higher computational cost.

Nevertheless, in this case the use of the Fisher model has put in evidence the dependence of the flow pattern on the turbulence level of the reservoir, allowing to appreciate the damping of turbulence effect caused by the suspended sediments.

6.3.2 Influence of the initial condition

Both experimental and numerical results have emphasized the versatility of the flow pattern in the configuration L-R. Therefore, the possible influence of the initial condition on the steady flow was investigated. To this purpose, simulations with a turbulence parameter $\alpha = 1$ and $\alpha = 2$ were repeated starting from two different initial conditions. First, the steady flow previously computed for $\alpha = 2$ has been used as initial condition for the new simulation with $\alpha = 1$ and vice-versa. Second, the simulations have been repeated with an empty basin as initial condition.

As already said, when considering $\alpha = 1$, starting from a basin with 0.2 m water at rest results in a flow pattern without reattachment point on the lateral wall (Figure 6. 8).On the other hand, starting from the flow field previously obtained with $\alpha = 2$, with one reattachment point on the side, a final steady flow, preserving the same flow pattern, is obtained. When $\alpha = 2$, if the simulation is started from water at rest, a flow pattern with one lateral reattachment point is obtained; on the contrary, no reattachment point is found in the final steady flow if the initial condition is the result previously obtained with $\alpha = 1$. So, it may be concluded that in all cases the same flow pattern of the initial condition is preserved. This confirms that both types of flow patterns, with and without lateral reattachment point, are mathematical solutions of the system for both considered values of the turbulence parameter. Nevertheless, either of them is observed depending on their relative stability and the flow history.

In addition, when an empty basin is considered as initial condition, a steady flow pattern with one lateral reattachment point is obtained with both turbulence parameters, in accordance with the experimental results. Numerical errors in filling the basin may allow the development of the instability. This also confirms the relative instability of the flow field in configuration L-R, the pattern of which is shown to be highly sensitive to the initial condition and to the flow history.

The same procedure has been repeated for configuration C-R (Figure 6. 9). The flow pattern with one reattachment point on the right wall is predicted in all cases, except for the low turbulence simulation ($\alpha = 0.5$) with water at rest as initial condition, which leads, as already said, to a flow field without reattachment points, as found in the experiments.

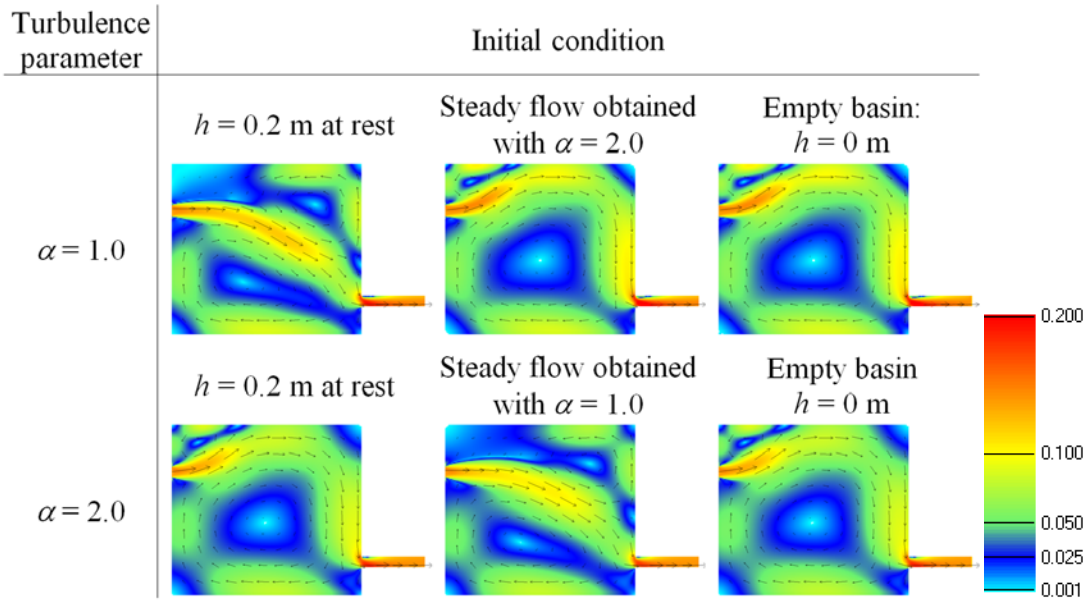

Figure 6. 8 - Final steady velocity field (m/s) in configuration L-R for different initial conditions. The legend indicates velocity intensity (m/s)

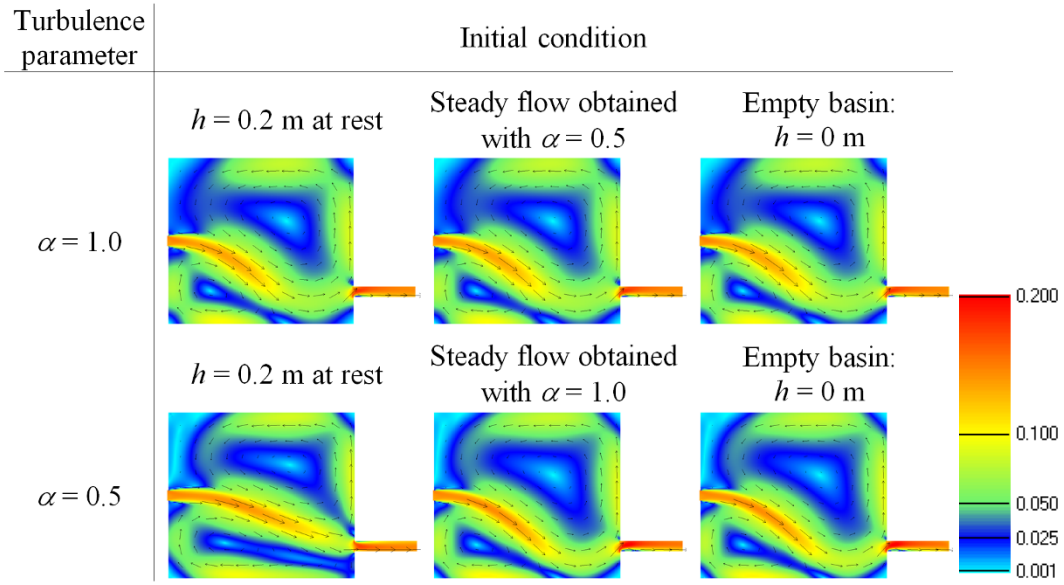

Figure 6. 9 - Final steady velocity field (m/s) in configuration C-R for different initial conditions. The legend indicates velocity intensity (m/s)

6.3.3 Conclusions

The depth-averaged flow model WOLF 2D, with an algebraic turbulence closure (Fisher model), was applied to assess its ability to predict the flow patterns for the four tested reservoir configurations with asymmetric position of the inlet and of the outlet channel.

For configurations C - C and L - L, the numerical model succeeds in providing robust predictions of the flow pattern in agreement with experimental observations. Computed flow patterns remain essentially insensitive to variations of the turbulence parameter and of the initial condition

In contrast, for configurations L-R and C-R, the simulations revealed a higher versatility of the computed flow patterns.

In particular, the simulated flow pattern for configuration L-R is found to have one lateral reattachment point, no reattachment point or to be unsteady depending on the turbulence parameter and on the initial condition. In fact, also in experiments, two different stable types of flow patterns were identified for this reservoir configuration: one, with a reattachment point on a lateral wall, for clear water conditions; the other, with no lateral reattachment, for tests with suspended load. By analyzing numerical simulations and comparing them with experimental results it can be argued

that turbulence intensity is the main cause which lead the flow pattern to change for the L-R configuration, when tests are performed with clear water or with sediments.

Numerical results suggest that the presence of suspended load exerts a turbulence damping effect, in agreement with theoretical considerations about the Reynolds particle number. In fact, the numerical model shows no reattachment if turbulence parameter is reduced, in agreement with the flow pattern observed in experiments with suspended load.

In the configuration C-R, a flow pattern matching experimental observations is predicted only if a low turbulence parameter is used. On the contrary, for higher values of turbulence parameter one reattachment point on the right wall is wrongly predicted.

For these reasons, the turbulence parameter remains for these two reservoir configurations a case-dependent calibration coefficient, and it represents the present limit of the flow model.

6.4. Simulations with sediment supply

The flow patterns defined in the previous paragraph have been used as initial condition for the simulations with an inflowing suspended load, using the purpose-made suspended sediments transport module implemented in WOLDF2D.

At the present moment, the simulations that have been carried out are preliminary simulations, with the aim to test the good functioning of the model; a sensitivity analysis on the parameters of the model which can be object of calibration will be performed in the next future. The final aim is to reproduce the sediments deposits distribution on the bottom of the experimental reservoir, and the global trapping efficiency after 4 hours of sediments supplying; the sediments thickness measurements carried out (see paragraph 3.3.4 and 4.5.2) will be used as the basis to perform the calibration of the sediment transport module parameters.

Anyway, the first results of the simulations performed up to now are encouraging, as it will be shown in the next paragraph.

6.4.1 Preliminary simulations

Preliminary simulations were performed on a coarse grid (5x5 cm) for the 4 reservoir configurations with different positions of the inlet and outlet channel (paragraph 3.4.2)

Table 6.4 presents the parameters adopted for the simulations by WOLF2D, as far as concerns the flow, the numerical method, and the sediment transport module.

The main results produced by the model are:

- maps of sediment concentration in the flow;
- maps of sediment thickness on the bottom of the reservoir;
- temporal evolution of concentration and of the sediments deposits thickness for every cell of the domain.

Table 6.4 – Parameters for the preliminary simulations by WOLF2D

Runge Kutta method	2nd order – 2steps
Max Courant number	0.3
Porosity	0.6
Colebrook roughness	0 m
Turbulence closure	Fisher model α=1
Internal reconstruction	Linear
Sediments diameter d	89 μm
Relative density ρ_s/ρ	1.5
Adaptation coefficient α_{adap}	1
Capacity transport coefficient β	0.034
Turbulent Fisher coefficient for sediments α_s	1

Then, starting from the integration of sediment thickness over the entire reservoir surface, the volume of sediments trapped in the reservoir can be obtained, and consequently the trapping efficiency of the reservoir can be calculated.

Figure 6. 10 shows the thickness of sediments deposits for the 4 analyzed reservoir configuration after 4 hours of sediments supplying. As it can be seen, comparing these results with the experimental data showed in paragraph 4.5.2, the numerical simulations correctly predict that the main sediments deposition occurs along the main jet, with lower sediments deposition in the centre of the recirculation zones. Actually, the thickness of sediments deposits is overestimated by the numerical model along the main jet, while in the recirculation regions the sediments thickness is underestimated .

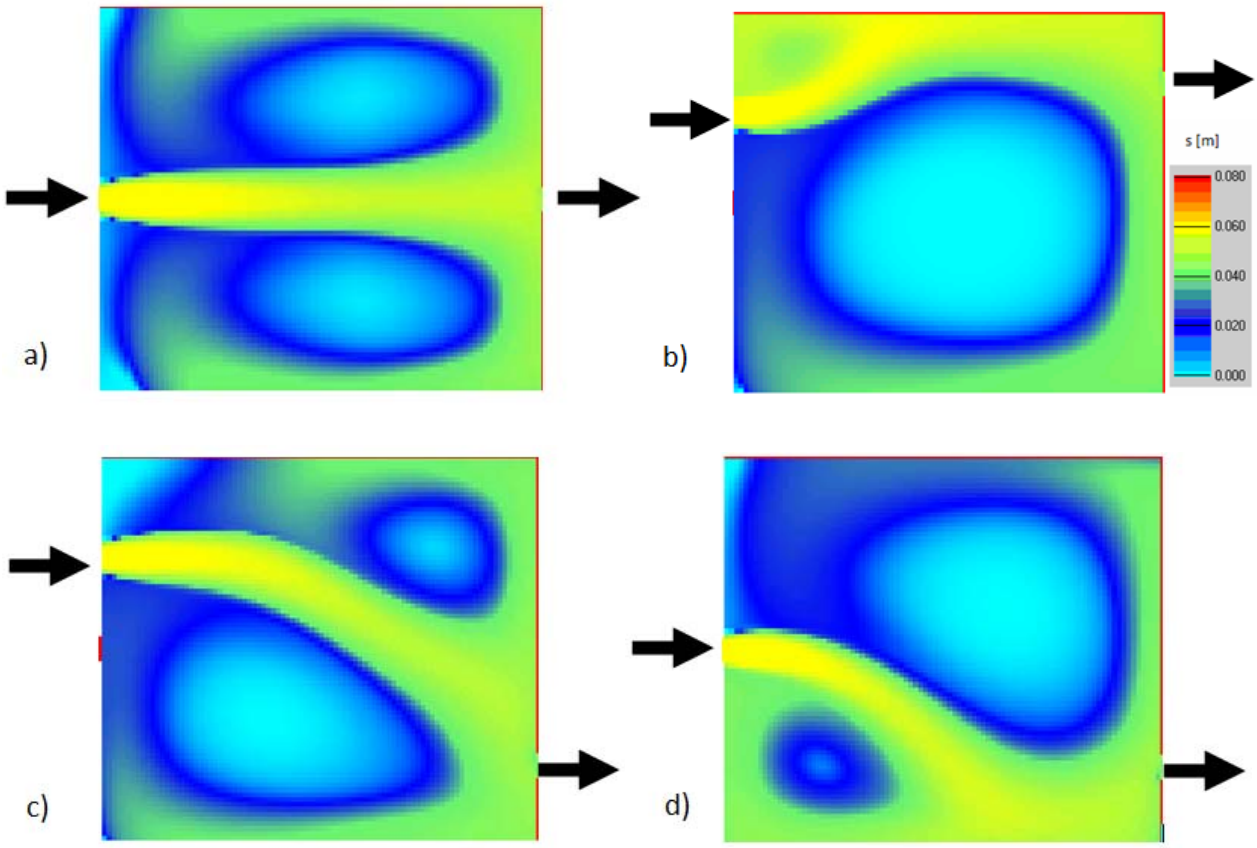

Figure 6. 10 – Sediments deposits thickness forecast by numerical simulation with WOLF2D. a) C-C configuration b) L-L configuration c) L-R configuration d) C-R configuration

As far as concern the global trapping efficiency, the values forecast by the model for the 4 reservoir configurations are shown in Table 6.5 and, as it can be seen, they are higher than the values experimentally found for the EPFL reservoir (Table 4.5).

Table 6. 5 – Trapping efficiency for the 4 reservoir configuration tested numerically by WOLF2D.

reservoir configuration	TE
C-C	0.72
L -L	64
L-R	70
C-R	71

So, in the next future, in order to arrive to a better representation of the sediments deposition on the reservoir bottom, some parameters of the model will be object of a calibration, as it will be explained in the following paragraph.

6.4.2 Future sensitivity analysis

The parameters of the model which could be object of calibration, in order to arrive to a more accurate representation of sediments deposits and of the global trapping efficiency are the following:

- Sediment diameter: since the inflowing sediments have not a unique diameter, while for the moment the software can consider only one diameter class, for the moment a representative diameter was chosen to perform the preliminary simulations; in particular, the average diameter of the sediment mixture, d = 89 μm (v_{ss} = 0.00196 m/s) was adopted. Indeed, a variation of the diameter equal to 11-12%, causes a variation of 23% of the settling velocity, so sediments deposition can be significantly affected from the diameter variation. For this reason, for the future the implementation of a multiple size-classes model will be evaluated, since it could give substantial benefits to the simulations.
- Empirical coefficient of the transport capacity law (Celik and Rodi, 1991): the β coefficient of the transport capacity law for the moment has been adopted as suggested by the paper of Celik and Rodi, that is to say $\beta = 0.034$. since this parameter is empirical, its value could be slightly changed, for example it could be evaluated which is the effect of a doubling of β on the sediments deposits, since an increase of this coefficient should lead to a n increase of transport capacity and so to less deposition in the reservoir.
- Sediment turbulent coefficient α_s: it represents the diffusion of sediments due to turbulence, and its value was adopted equal to 1 in the preliminary simulations, as for the turbulent coefficient of the Fisher model. If the turbulent coefficient of the sediments was increased, the resulting sediment deposits should be more widely distributed along the central jet sides, due to the increased turbulent diffusion.
- Porosity p: the porosity value reflects in a direct way on the sediments deposits thickness and on trapping efficiency: the more porosity is high, the higher is the thickness of sediments

deposits, for the same amount of sediments deposited; on the other hand, the trapping efficiency decreases for higher values of porosity, given a certain sediments deposits thickness, because a smaller amount of sediments is present in the given volume.

Since experimental measurements indicated very high values of porosity (between 0.6 and 0.8), due to the very high water content of sediments deposits, for the preliminary simulations a porosity value of 0.6 has been adopted.

- Coefficient of adaptation α_{adap}: this coefficient modulates the disequilibrium between the capacity transport and the current concentration in the cell of the domain. For the moment it has been left equal to one, but this coefficient can assume a large range of values, between 1 and 10, depending on the Rouse number. In a future, instead of being a fixed number, it could also take the form of one of the proposed empirical expressions, as those suggested by Galappatti and Vreugdenhil, Armanini and Di Silvio or Zhou and Lin (Wu, 2008).

6.4.3 Grid independency

A sensitivity analysis to the size of the mesh cells was also performed, comparing the results of the C-C reservoir configuration obtained for the coarse mesh (0.05 cm) to the results obtained for a fine mesh (0.025 cm). The comparison of the deposits after 2 hours of sediments supplying (Figure 6. 11) showed that the differences between the results of the fine mesh and of the coarse mesh were not appreciable, so the coarse mesh was chosen to perform all the other simulations concerning asymmetric reservoir geometries, since it leads to a saving of computational time.

However, as can be seen in Figure 6. 11, the agreement of the numerical data with the experimental values measured after 2 hours of experiments was not very good: sediments deposits were in general overestimated in the main jet and underestimated in the re-circulation zones by the numerical model, except for the upstream part of the reservoir. For this reason, the sensitivity

analysis (explained in the precedent paragraph) on the parameters of the simulation will be performed, in order to achieve better results in reproducing sediments deposits distribution.

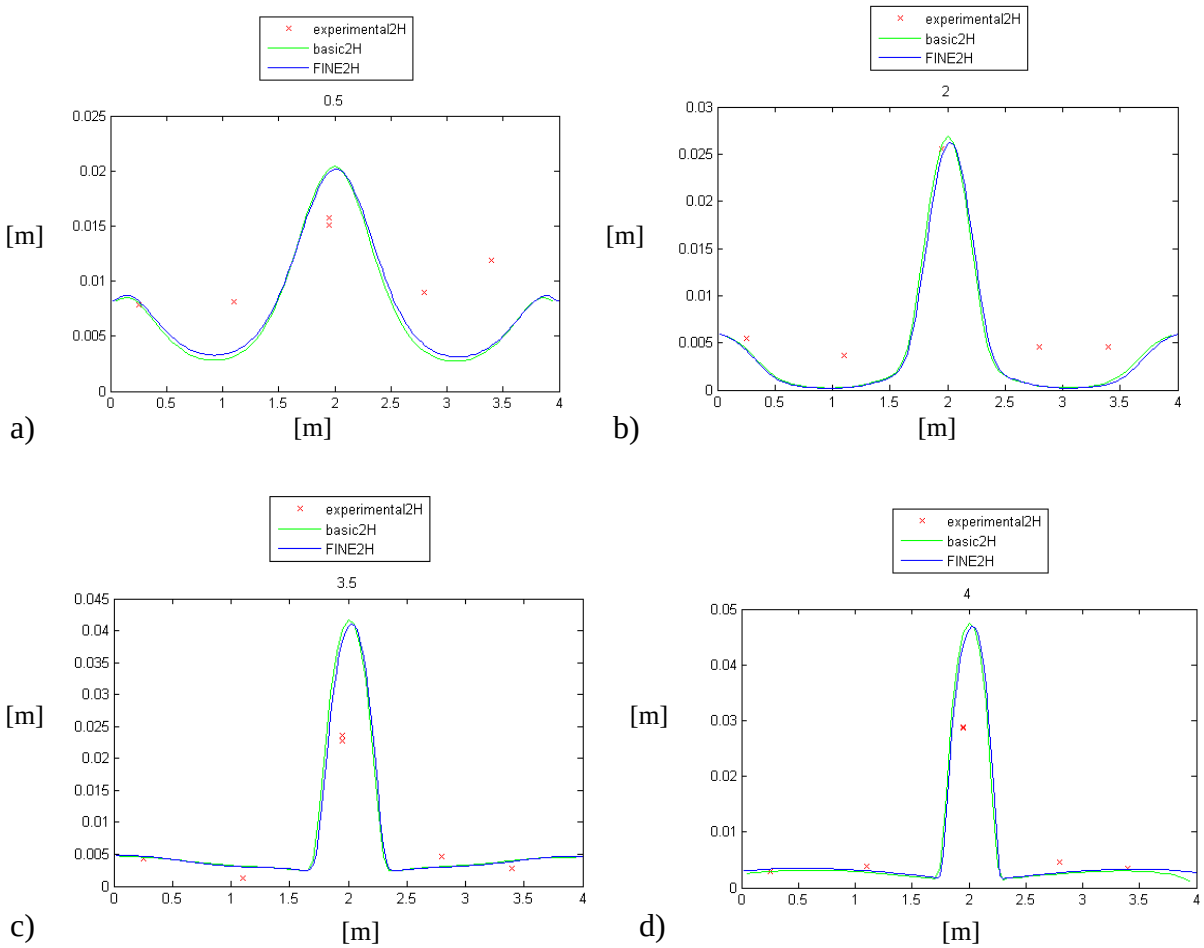

Figure 6. 11– Sediment deposits thickness [mm] at different cross sections x of the reservoir after 2 hours of sediments supplying a) x=0.5 m downstream b) x=2m c) x=3.5 m d) x =4 m - upstream

CHAPTER 7

THE MEANDERING FLOW

In the following chapter a different type of flow pattern, not yet discussed, is presented. It has been chosen to name this type of flow field "meandering flow", since the main central jet, on the axis of the reservoir, presents regular and quite wide oscillations, whose period have been studied by numerical simulations in the framework of this thesis.

This flow pattern exists only for determined Froude numbers, and for this reason it was not detected in the experimental activity of the author at EPFL (chapter 3 and 4), since in that case the Froude number was fixed (F_{in} = 0.1), and the interest was to change the reservoir geometry at fixed hydraulic conditions. On the contrary, thanks to the numerical model WOLF2D, validated on the basis of the available experimental data (as explained in Chapter 6), it has been possible to change the hydraulic condition of the reservoir, by performing new numerical simulations in which the inlet Froude number has been changed. In particular, changing the water depth of the reservoir was changed, keeping a constant discharge, and under these conditions the meandering flow pattern appeared. Moreover, the existence of this type of flow pattern was qualitatively assessed by experimental observation on an experimental facility at Politecnico of Milano, through flow visualizations.

So, it seemed to be worth of being published in this thesis also the first results obtained in the study of this particular flow field, even if the research on this subject is still going on.

In fact, a lot of characteristics of this flow pattern could be investigated, as for example the spatial amplitude of the oscillation of the jet, in relationship with the size of the reservoir; nevertheless, for the moment the present work aimed simply to study the oscillation frequency of the jet, which is represented by the oscillation frequency of the transversal velocity. In particular, the link between the Strouhal number of the "numerical experiment" and the correspondent Froude number has been looked for.

7.1. Previous studies

It does not exist much literature about the subject of a meandering water jet in a reservoir. An example of the study of oscillating flows can be found in the papers of Honeylands and Molloy (1995) and of Davidson and Lawson (1999) but in that case the field of application was very different, since that study concerned confined jets in rectangular cavities during the process of casting of steel.

On the contrary, as far as concerns meandering flows in a reservoir, Kantoush (2008) had already assessed qualitatively the existence of this type of flow pattern, but he hadn't studied the oscillation frequency or other quantitative characteristics of the meandering flow field. He simply observed that for h = 0.15 – 0.1 – 0.075 m a meandering flow pattern develops in the reservoir. Kantoush performed his experiments about the meandering flow keeping constant the discharge Q = 7 l/s and varying the water depth. In this way, besides the variation of the inlet Froude number, a variation of the non-dimensional water depth happens, too. The same experimental procedure has been adopted for the numerical experiments presented in this chapter, even if an other way to modify the Froude number, without affecting the non-dimensional depth, is to operate on the water discharge . This option is for the moment postponed to future research on the subject.

7.2. Experimental apparatus at Politecnico of Milano

In order to have the possibility to observe the meandering jet flow type, in the way to confirm the numerical results of the model, a small reservoir was built in the G. Fantoli Hydraulic Laboratory at Politecnico of Milano. The experimental facility, shown in Figure 7. 1, is a scaled model (≈1:5) of the experimental facility of EPFL; it is a white PVC reservoir endowed of a dedicated closed hydraulic circuit, formed by a pump and some conduits, which allow to re-circulate the discharge from the downstream reservoir to the inlet channel. The dimensions of the reservoir are L = 1,17 m, B = 0.78 m, b = 0.048 m, with a maximum water depth h = 0.1 m

a)  **b)** 

Figure 7. 1 – a) Lateral view of the experimental facility at Politecnico of Milano. b) Top view of the experimental reservoir with seeding for flow pattern visualization.

Experiments were carried out in the reservoir at Politecnico respecting the Froude similarity with the model in Lausanne, obtaining for the discharge a value Q = 0.125 l/s (R_{in} = 10417). In order to visualize the water trajectories, light polystyrene particles have been added to the water, falling into the water from an apposite continuous distributor placed at the beginning of the inlet channel. An high-frames rate camera was placed over the reservoir, in order to have a view of all the reservoir surface and to get videos of the water trajectories highlighted by the floating particles. First of all, in order to exclude the onset of scale effects, it was checked that the meandering jet type developed in the scaled reservoir for the same conditions of the big reservoir. The water depth of the experiments in which Kantoush assessed the existence of the meandering flow was scaled 1:5 and effectively also in this "small" reservoir a meandering jet could be visualized by the seedings under those hydraulic conditions. A video about these flow visualizations is available in the attached dvd.

7.3. Numerical simulations by WOLF2D

Since from the experiments of S. Kantoush it resulted that, for the reservoir configuration 6x4m, the flow pattern is characterized by a central meandering jet if the water height in the reservoir is decreased from 0.2 to 0.15-0.1-0.075 m, (conserving the same Reynolds number, that is to say the same discharge Q = 7 l/s) at the beginning of this research it was chosen to see if the numerical

model was able to detect the existence of a meandering flow pattern in the same geometric and hydraulic condition of Kantoush's experiments.

So, the geometry of the reservoir 6x4 m, where Sameh has assessed the onset of the meandering jet, was reproduced in WOLF2D and the simulations were started. Effectively, simulations showed the existence of the meandering flow pattern for the same water depths signalled by Kantoush (Table 7. 1). An example of an instantaneous velocity map produced by the numerical model is given in Figure 7. 2, while a video of the simulated meandering flow is available in the attached dvd.

Table 7. 1– Oscillation periods and Strouhal number for the reservoir 6x4 m with three different water depths: 0.075 – 0.1 – 0.15 m

	h/b	Experiments Kantoush Q=7 l/s	WOLF2D Initial condition: WATER AT REST	Period T [s]	Strouhal St [-]	Froude F_{in} [-]
h= 0.2m	0.8	Not meandering	Not meandering	-	-	0.1
h=0.15 m	0.6	Meandering	Meandering	7.3	0.18	0.15
h=0.1 m	0.4	Meandering	Meandering	7.8	0.11	0.28
h=0.075 m	0.3	Meandering	Meandering	7.4	0.09	0.43

In Table 7. 1 it can be seen that the Strouhal number based on the inlet channel width *b* has been calculated:

$$St = \frac{b \cdot f}{V_{in}} \qquad (7.1)$$

where *f* is the frequency of oscillation of transversal velocity, that is $f = 1/T$, while T is the period of oscillation.

The period of oscillation of the transversal velocity T is not significantly affected by the variation of the non-dimensional depth, and it keeps an approximately a constant value of about 7.5 s. About the inlet Froude number, it can be observed that the oscillation period remains constant even if the inlet Froude number varies by a factor 3. So it can be concluded that the Froude number, or its correspondent non dimensional depth have not a significant influence on the period of oscillation of the jet. On the contrary, the Strouhal number has a strong variation when the Froude

number changes; so, the relationship between these two non-dimensional groups has been studied and it will be presented in paragraph 7.5.

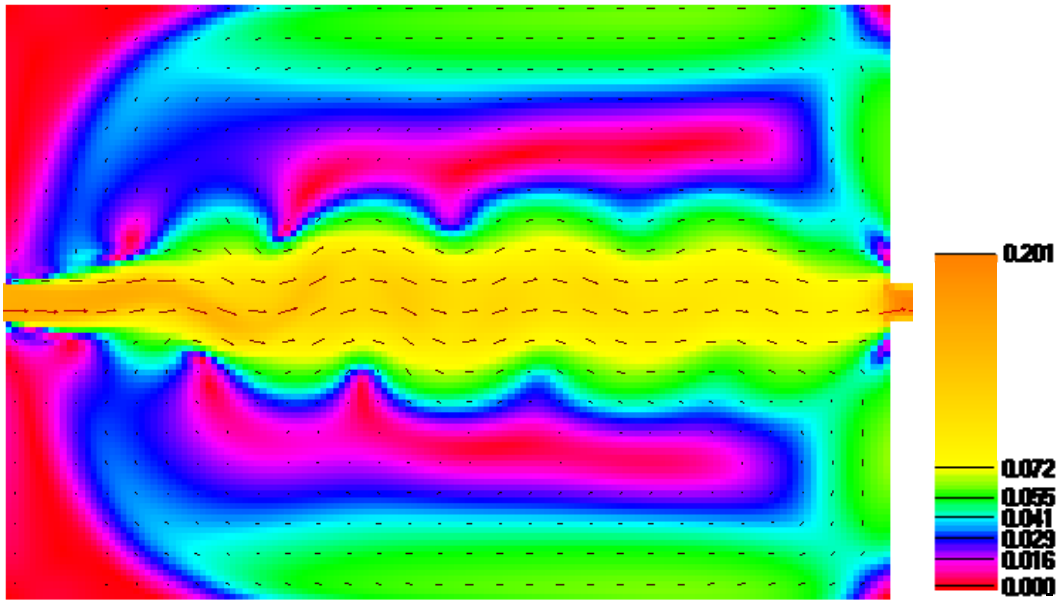

Figure 7. 2 - Velocity map of the meandering jet (the colors indicate the absolute value of velocity [m/s]) reservoir 6x4 m – h =0.2 m Q = 0.007 m^3/s

Then, the phenomenon of the meandering flow has been studied numerically in reference with the reservoir of Politecnico of Milano (L = 1.17 m, B = 0.78 m, b = 0.048), choosing 4 water depths (0.04 – 0.03 – 0.02 – 0.015 m) which lead approximately to the same hydraulic conditions (similar inlet Froude number) of the numerical simulations performed for the 6x4 m reservoir, though the inlet Froude number are not exactly the same due to the not perfect geometrical scaling of the reservoir. The aim was to evaluate if the same meandering flow fields found in the 6x4m reservoir were reproducible at the smaller scale, and to evaluate the possible onset of scale effects.

The results of the performed numerical simulations, in terms of the oscillation period of the transversal velocity and of the Strouhal number are presented in Table 7. 2.

The Froude number of these experiments are not exactly the same of the larger reservoir (Table 7. 1), due to the not perfect scaling of the inlet channel width: in fact, instead of being b = 0.05 m, as already said the Politecnico experimental facility has an inlet channel with b = 0.048 m. Anyway, as a first approximation the three experiments, corresponding to three different water heights in the 6x4 m reservoir, can be considered to have been performed in the same hydraulic conditions of the

three experiments performed in the 1.17x0.78 m reservoir, though the inlet Froude numbers are not exactly the same.

Table 7. 2 – Oscillation periods and Strouhal number for the reservoir 1.17x0.78 m with three different water depths: 0.015 – 0.02– 0.03 m

	h/b	Experiments at Politecnico Q = 0.125 l/s	WOLF2D Initial condition: WATER AT REST	Period T [s]	Strouhal St [-]	F_{in} [-]
h= 0.04m	0.83	Not meandering	Not meandering	-	-	0.1
h=0.03 m	0.63	Meandering	Meandering	3.35	0.17	0.16
h=0.02 m	0.42	Meandering	Meandering	3.35	0.11	0.29
h=0.015 m	0.31	Meandering	Meandering	3.8	0.07	0.45

The oscillation periods presented in Table 7. 1 and Table 7. 2 have been calculated according to the following procedure: first, time series of the transversal velocity component in different points of the reservoir (5 points along the central axis of the reservoir) were extracted from the simulations (Figure 7. 3); then, the temporal signals were treaded by an apposite routine in Matlab that allowed to calculate the discrete Fourier transform $|Y(T)|$ of the signal in the way to individuate the dominant frequencies, that is to say the oscillation period (Figure 7. 4) .

It has to be underlined that the oscillation frequency of transversal velocity was the same for all the points along the reservoir axis, so it was possible to identify the period of oscillation of the meandering jet with the period of oscillation of the transversal velocity component.

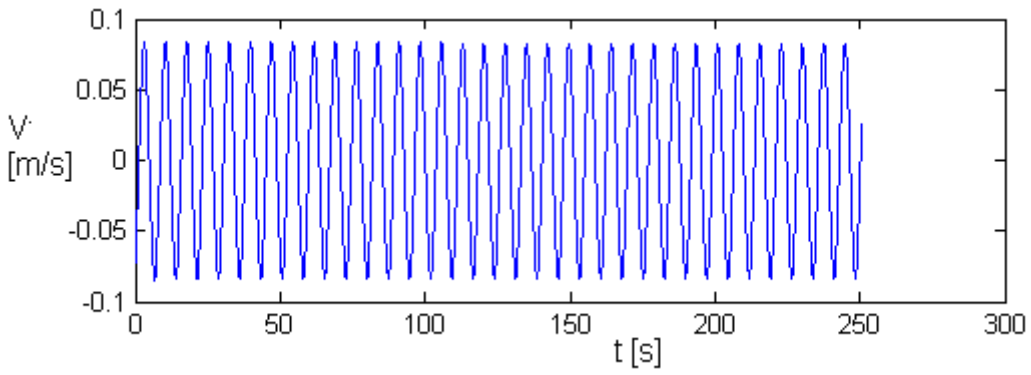

Figure 7. 3 – Temporal signal of the transversal velocity *v* in one point along the axis of the meandering jet (reservoir 6x4m)

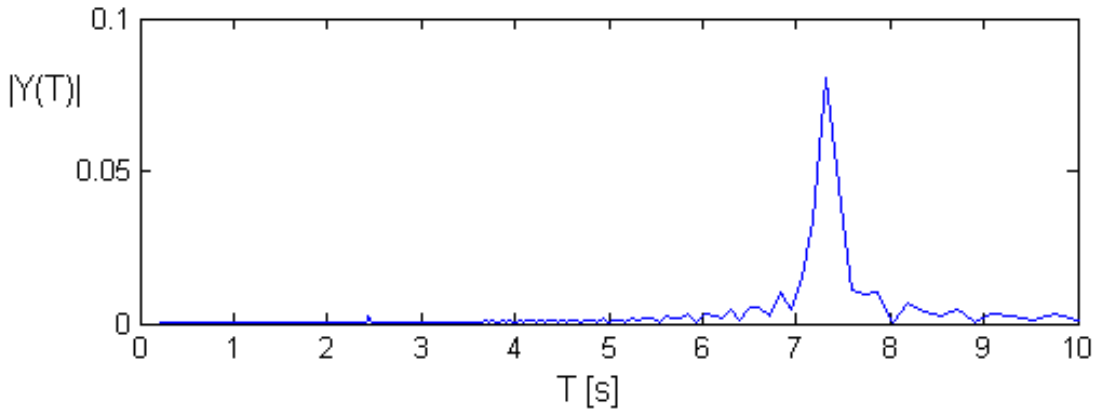

Figure 7. 4 – Spectrum of the transversal velocity *v* in one point along the axis of the meandering jet (reservoir 6x4m)

Moreover, films of the temporal evolution of the velocity vectors in all the reservoir (available in the attached dvd) were produced on the basis of the vectorial maps of WOLF, in order to check visually if the oscillation of velocity resulting from the film corresponded to the calculated one by the discrete Fourier transform, and the oscillation period of about 7.5 s for the 6x4m reservoir and of about 3.5 s for the 1.17x0.78m reservoir were confirmed.

Anyway, the discrete Fourier transform analysis showed also the existence also of longer periods, that is to say of lower frequencies, which are probably associated to slower dynamics of the flow in the reservoir, which are not the object of this study and which would require longer time series in order to be identified more precisely. In fact, as it can be seen in Figure 7. 5a, besides of the high peak correspondent to the macroscopic oscillation of the meandering jet ($\boldsymbol{T} \approx 7$ s), an other smaller but larger peak is visible, having a period of about 60 seconds, as it can be observed also in Figure 7. 5b: besides the high frequency of oscillation, the temporal signal shows an oscillation having a lower frequency, which appears in the figure with only two periods.

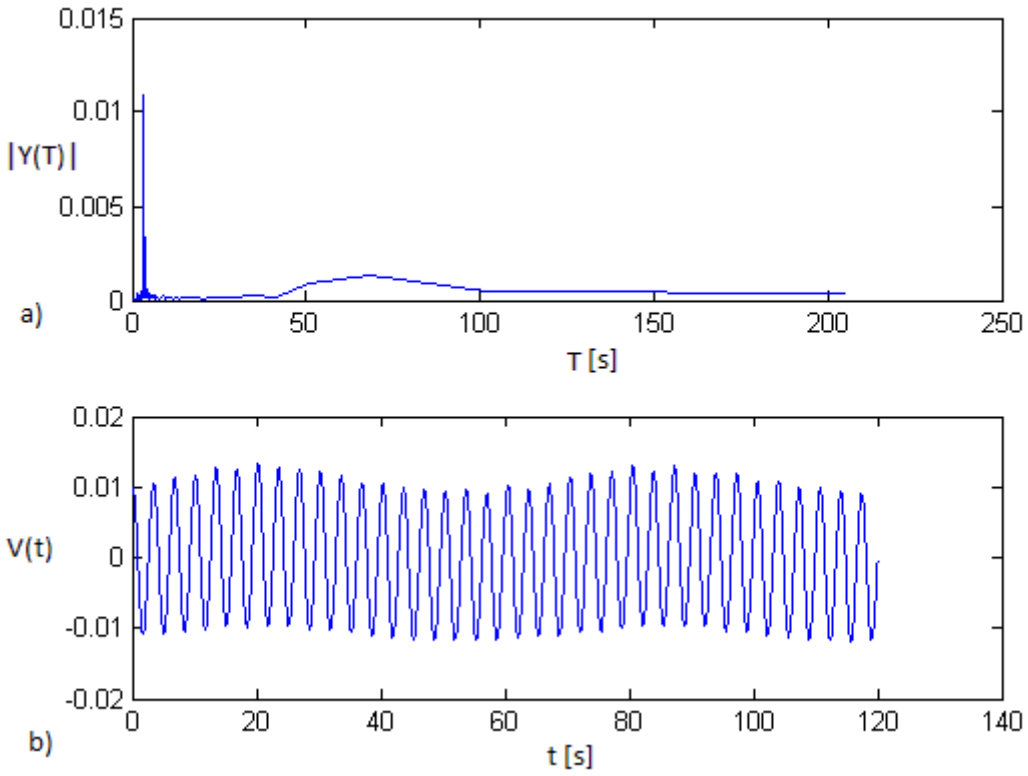

Figure 7. 5 – Complete spectrum and temporal signal of one point in the reservoir 6x4m: the large peak associated to the lower frequency present in the signal is visible.

As far as concern the Froude similarity between the 6x4 m reservoir and the 1.17x0.78m reservoir, the scale for the Strouhal number can be derived in the following way:

$$\lambda_V = \frac{V_m}{V_p} = \frac{\frac{L_m}{t_m}}{\frac{L_p}{t_P}} = \lambda_G \cdot \frac{1}{\lambda_t} \cdot \qquad (7.2).$$

Thanks to equation 3.3, we can substitute λ_V and find the scale for the time λ_t:

$$\sqrt{\lambda_G} = \frac{\lambda_G}{\lambda_t} \longrightarrow \lambda_t = \sqrt{\lambda_G} \qquad (7.3)$$

Then, since the Strouhal number can be defined as:

$$St = \frac{L}{V \cdot t} \qquad (7.4)$$

we obtain that

$$\lambda_{St} = \frac{\lambda_L}{\lambda_V \lambda_t} = \frac{\lambda_L}{\sqrt{\lambda_L} \cdot \sqrt{\lambda_L}} = 1 \quad (7.5)$$

It means that when we move from the prototype to the model, respecting the Froude similarity, also the Strouhal number keeps constant.

Actually, if we observe the results in Table 7. 1 and Table 7. 2, which correspond to nearly constant Froude numbers, we can see that also the Strouhal numbers keeps nearly constant (the ratio between the correspondent Strouhal numbers are 0.8 ÷ 1) . So, we can assess that the phenomenon of oscillation of the meandering jet is not subjected to scale effects, and its characteristics can be studied in whichever of the two reservoirs.

It has to be noted that, even if the inlet Froude number, (the *h/b* ratio and the Strouhal number) remains constant, as a first approximation, in the passage from the "large" to the "small" reservoir, the Reynolds number of the 1.17x0.78 m reservoir (10400) is one order of magnitude lower than the Reynolds number of the 6x4m reservoir (112000), but in both the cases the performed experiments are in a turbulent regime.

7.4. Sensitivity analysis

Before performing the simulations presented in the previous paragraph, a sensitivity analysis to different numerical parameters of the simulation and to the mesh size was carried out, in order to assess that the observed oscillation is not caused by numerical effects, but it represents a real physical oscillation, as the oscillation that could be qualitatively seen in the experimental apparatus.

In particular it was chosen to analyze the effect on the frequency of oscillation of:

1. Courant number (tested values 0.5 – 0.25 – 0.125);
2. Sampling frequency (tested sampling time: 0.5-0.1-0.05 s);
3. Temporal discretization method (Runge Kutta method of first order - 3 steps and Runge Kutta method of second order - 2 steps);
4. Mesh size (Calculus of the Global Convergence Index GCI).

7.4.1 Courant number

As it can be seen in Figure 7. 6, the Courant number with which the simulation was performed has no influence on the results of the simulations. So, the Courant number can be increased up to the maximum value compatible with the stability of the simulation, that is to say with the Courant Friedrich Levy condition for stability (Erpicum, 2006). Usually, a Courant number of 0.5 was used for the simulations, and it was reduced only if numerical stability problems arise.

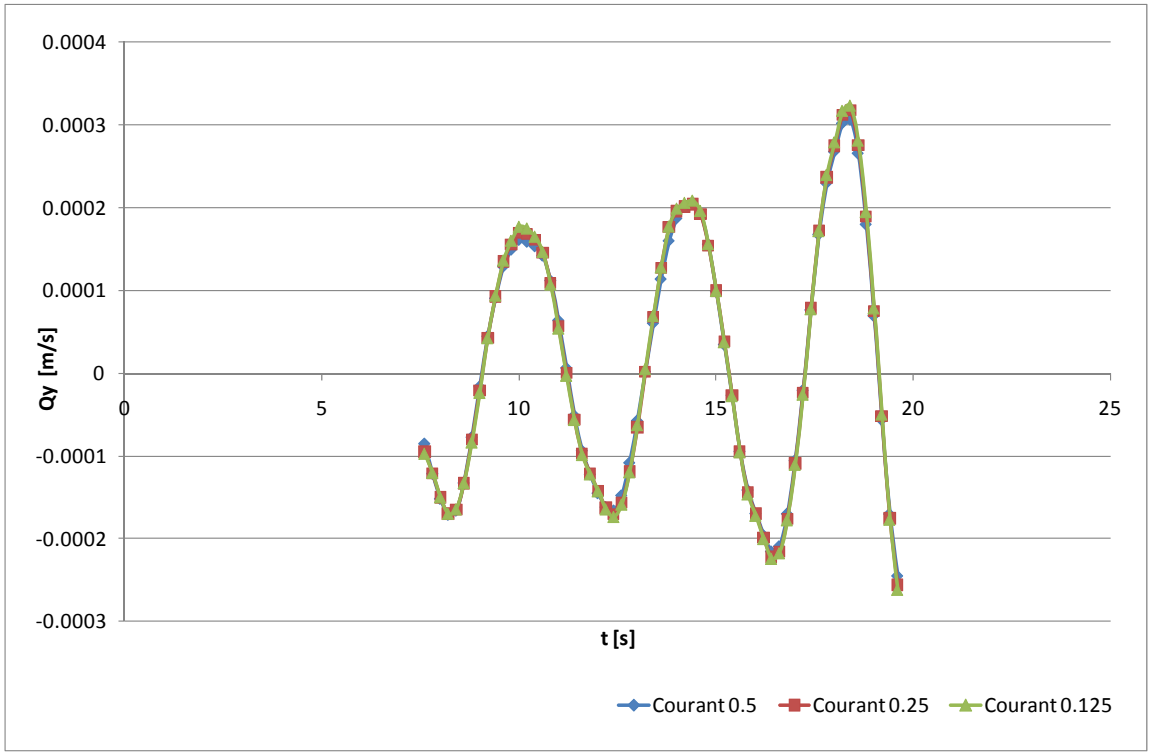

Figure 7. 6– Influence of the Courant number on oscillation frequency

7.4.2 Sampling frequency

In Figure 7. 7 two velocity signals are shown: the blue one corresponds to a sampling frequency of 2 Hz, the red one corresponds to a sampling frequency of 10 Hz. It can be seen that also the blue signal allows to correctly reproduce the oscillation of the signal. Anyway, for the simulations, a sampling frequency of 10 Hz was generally adopted, since it allowed to reproduce with accuracy the oscillation of the signal, without too much computational costs.

It must be remembered that the sampling frequency influences the maximum frequency that can be observed, and this maximum frequency (Nyquist frequency) equals the half of the sampling frequency, so in this case the maximum frequency that can be detected is 5 Hz.

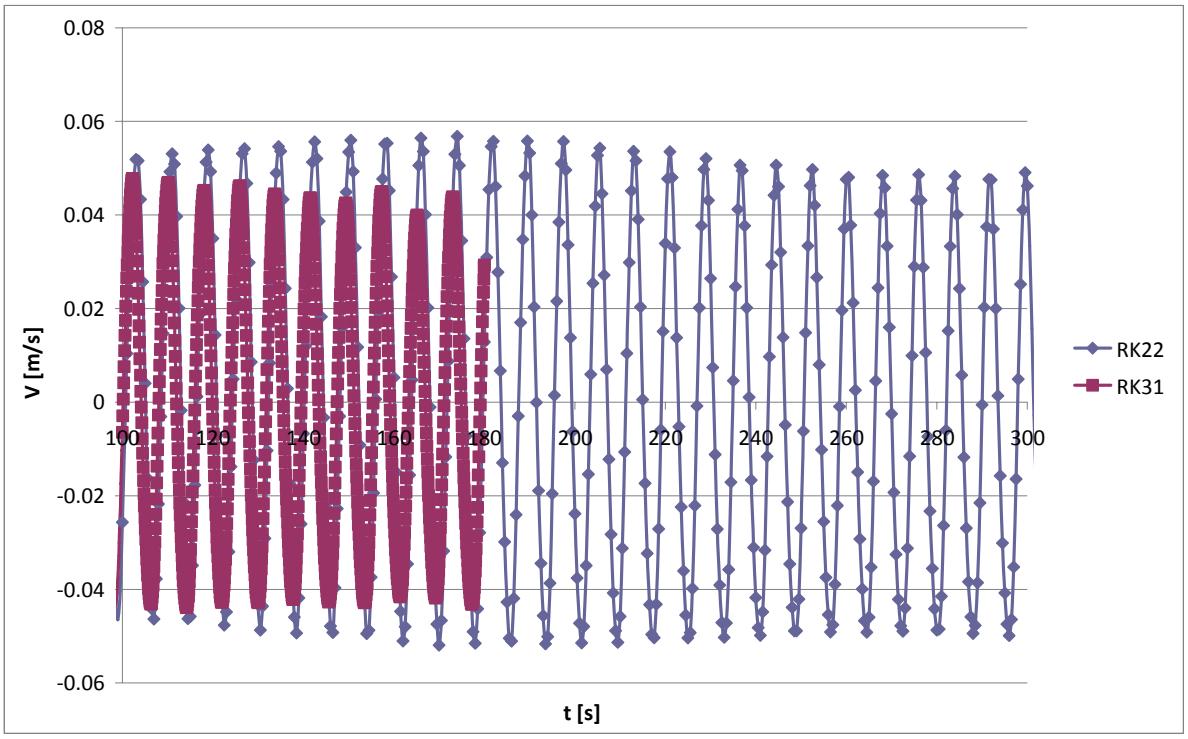

Figure 7. 7 – Analysis of the influence of the temporal discretization method Runge Kutta on the oscillation frequency. Temporal signal of velocity (RK 22 sampling frequency 2 Hz– RK31 sampling frequency 10 Hz)

7.4.3 Temporal discretization method

As it can be seen in Figure 7. 7, the different type of Runge Kutta methods (Erpicum, 2006) used for the simulation doesn't influence significantly the resulting oscillation frequency. A limited influence can be found in the amplitude of velocity oscillation: in fact, the Runge Kutta RK31 (first order 3 steps) tends usually to soften the peaks of a signal, damping slightly the amplitude of velocity oscillations; on the contrary the Runge Kutta RK22 (second order 2 steps) better reproduces peaks and it is more accurate, but the problem is that in some occasions it could introduce numerical oscillations, even if this is not the case. In conclusion, the Runge-Kutta method of second order was definitively adopted for the simulations, since it is more accurate.

7.4.4 Mesh independency (Global Convergence Index)

The influence of the mesh size on the oscillation frequency calculated by the numerical model was checked, in order to assess the grid independency of the results. To this purpose, the Grid Convergence Index (GCI) was calculated according to the procedure suggested by Roache (1994; 1997). In fact, the value of GCI provides an accuracy band (%), or confidence interval, between the numerical grid solution and the true solution of the continuum equations f_{exact}.

The procedure for calculating GCI, when 2 solutions (f_2, f_1) on 2 different grids are available (step Δh_2 coarse = 0.008 mm, step Δh_1 fine = 0.004 mm), and under the hypothesis that the order of convergence of the problem is i = 2, is the following:

- Evaluation of the grid refinement ratio $\boldsymbol{r} = \dfrac{\Delta \boldsymbol{h}_2}{\Delta \boldsymbol{h}_1} = 2$ (7.6)

- Evaluation of the estimated fractional error E_1 for the fine grid: $\boldsymbol{E}_1 = \dfrac{\dfrac{\boldsymbol{f}_2 - \boldsymbol{f}_1}{\boldsymbol{f}_1}}{\boldsymbol{r}^{\boldsymbol{i}} - 1}$ (7.7)

- Evaluation of the estimated fractional error E_2 for the coarse grid:

$$\boldsymbol{E}_2 = \frac{\dfrac{\boldsymbol{f}_2 - \boldsymbol{f}_1}{\boldsymbol{f}_1}}{\boldsymbol{r}^{\boldsymbol{i}} - 1} \cdot \boldsymbol{r}^{\boldsymbol{i}}; \qquad (7.8)$$

- GCI evaluation:

$GCI_{fine} = Fs \cdot E_1$, (7.9)

$GCI_{coarse} = Fs \cdot E_2$ (7.10)

where *Fs* is a safety factor, whose value is 3 when 2 grids are used, on safety side;

- Plot the results with the proper error band:

$$\boldsymbol{f}_{exact} = \boldsymbol{f}_1 \pm \boldsymbol{GCI}_{fine} \cdot \boldsymbol{f}_1 \qquad (7.11)$$

$$\boldsymbol{f}_{exact} = \boldsymbol{f}_2 \pm \boldsymbol{GCI}_{coarse} \cdot \boldsymbol{f}_2 \qquad (7.12)$$

Table 1 – Period of oscillation and GCI for the reservoir L = 1.17 m B = 0.78 m.

Cell size [mm]	Period T [s]	GCI	f_{exact}
8	3.85	0.65%	3.825÷3.875
4	3.86	0.16%	3.86

Anyway, the method can be applied only if the solutions are in the convergence radius of the problem. In order to verify if this condition is respected, it is necessary to dispose of 3 solutions on three different grids. To this purpose, the flow field was calculated also for a very fine grid (size 2 mm) and the solution f_3 concerning the oscillation period was extracted. So, the following steps were performed for the very fine mesh:

- Evaluation of the estimated fractional error E_3 for the very fine grid:

$$E_3 = \frac{\frac{f_3 - f_2}{f_2}}{r^i - 1} \cdot r^i = 0.0197; \qquad (7.13)$$

- GCI evaluation:

$GCI_{very\_fine} = Fs \cdot E_3 = 0.06;$ (7.14)

- Evaluation of the local order of convergence of the method

$$i = \frac{\ln\left(\frac{f_3 - f_2}{f_2 - f_1}\right)}{\ln r} = -3.48; \qquad (7.15)$$

Then, since it is verified that $GCI_{fine} \cong r^i \cdot GCI_{very\_fine} \cong 0.09$, the numerical solutions are in the convergence radius of the problem and the procedure of calculation of the GCI described here above can be considered as reliable.

Then, for the following simulations, it was chosen to use the coarse grid, since the incertitude of the resulting oscillation frequency was considered to be acceptable (0.65% on the oscillation frequency), and since it allowed to gain significant computational time.

7.5. Strouhal-Froude relationship

Thanks to the calculus of the Froude number and of the Strouhal number for the numerical experiments performed in the 6x4m reservoir and in the 1.17x0.78m reservoir, a relationship between the inlet Froude number and the Strouhal number which characterize the oscillation of the meandering jet can be established. The link between these two non-dimensional groups can be approximated quite well (R^2 = 0.97) by a logarithmic relationship, as it can be seen in Figure 7. 8. The formulation of the fitting logarithmic relationship is the following:

$$St = 0.09 \cdot \ln(Fr_{in}) + 0.002 \qquad (7.16)$$

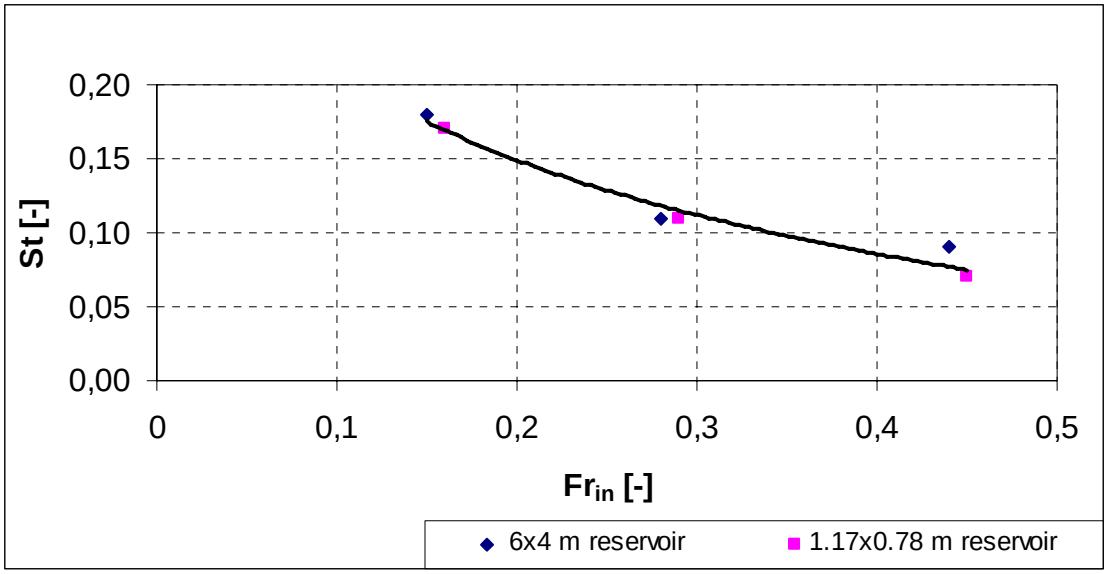

Figure 7. 8 – Strouhal-Froude relationship for the meandering jet

Of course, a future enrichment of the database, as far as concern experimental and numerical results, could lead to a more strong confirmation of this formulation or to a variation of its shape.

7.6. Outlook for further research

The research on the meandering flow pattern, as it is also for the simulations with suspended sediments, is still open and a lot of work has still to be done.

In particular, in the next future, the experimental apparatus present at Politecnico of Milano or the experimental facility at EPFL will be used to investigate quantitatively, by LSPIV or UVP the characteristics of the meandering flow, in order to have an experimental validation of the numerical results obtained up to now.

To get more knowledge about the phenomenon of the meandering jet, other characteristics could be studied, as for example:

- the amplitude of the oscillation of the velocity vectors,
- the spatial amplitude of the oscillation of the jet with respect to the dimension of the reservoir,
- the wave-length of the jet in the reservoir,
- other lower frequencies present in the signal, which does not represent the macroscopic oscillation of the jet, but that are probably linked to slower dynamics of the flow field,
- the frequency of detachment of the lateral vortex on the side of the main jet in the upstream part of the reservoir.

Furthermore, the next and main objective of the ongoing research is to change the Froude number not operating on the water depth but on the inflowing discharge, keeping in this way the h/b ratio as a constant. In fact, actually it is not known if the onset of the meandering flow is due to the increase of the Froude number, as suggested in this thesis, or to a reduction of the water-depth. Anyway, if the water depth will be kept constant, and the Froude number will be varied through an increase of water discharge, it will be possible to see if the meandering flow field develops and shows the same relationship between the Froude and the Strouhal number proposed in this thesis.

CHAPTER 8

CONCLUSIONS AND FUTURE PERSPECTIVES

8.1. Flow patterns study

The experimental and numerical work performed up to now has allowed to get a quite complete view over the effects of geometry in a rectangular shaped shallow reservoir, at fixed hydraulic conditions. In fact, the combined influence of the length-to-width ratio and expansion ratio has been formalized in a plot which allow to know which type of flow pattern can develop in a reservoir as a function of these 2 non-dimensional parameters.

The criterion to distinguish between an asymmetrical flow field A1 and a symmetric flow field S1, already proposed by Dufresne et al. (2010a), has been confirmed by the new experimental data collected in the framework of this thesis. This criterion takes into account the existence of a zone of instability between the asymmetric flow pattern A1 and the symmetric flow pattern S1, which has been studied in detail in this thesis by using the moment of asymmetry, proposed by Dewals et al. (2008) as indicator of the flow field asymmetry. As far as concern the transition between the S1 and the S0 flow pattern, the experimental data collected during this thesis have shown that the flow pattern with only two lateral recirculation zones, the S0 flow field, develops only when the length of the reservoir is shorter than its width. Experiments have also confirmed that for expansion ratio lower than two, the motion in the reservoir degenerates in a channel-like flow, mainly one-dimensional, as it was already suggested by the experiences of Abbott and Kline (1962).

About the transition between the A1 flow field and the A2 flow field, that is an other type of asymmetric flow followed by a nearly plug flow condition, the numerical simulations performed by WOLF2D have partially supplied to the lack of experimental data in correspondence of this transitional zone. Anyway, a definite criterion to distinguish between these 2 types of flow pattern

has not been given yet. Further simulation near the transitional zone, in a future, could lead to a definition of an equation in order to distinguish between the 2 flow patterns types.

So, for the fixed hydraulic condition in which experiments were performed, now we have available an instrument (the length-to-width versus expansion ratio plot) which allows to classify the flow pattern type as a function of the geometrical characteristics of the reservoir.

Nevertheless, what could happen in the reservoir if the hydraulic boundary conditions are changed is still partially an unknown, and it can hide some surprise. In fact, for higher Froude numbers, corresponding to reduced non-dimensional depths, a meandering flow pattern has been found and studied in the framework of this thesis. The study of the characteristics of this type of flow field is far to be completed, but in this thesis the investigation of the oscillation frequency of the meandering jet is presented, together with a first attempt to link the Froude number to the Strouhal number characteristic of the phenomenon.

During this thesis, the flow pattern classification has been associated to some attempts of turbulence analysis and to consideration concerning the kinetic energy content of the reservoirs. In particular, about the kinetic energy content a logarithmic relationship has been proposed in order to link the surface of the reservoir to the kinetic energy content of the reservoir.

In the next future, the study of the flow patterns will concentrate above all on the study of other characteristics of the meandering flow: in particular, first of all it will be investigated which is the spatial amplitude of the oscillation with respect to the total dimension of the reservoir and further reservoir configurations will be studied in order to give more validity to the proposed relationship between the Froude and the Strouhal number.

Furthermore, an important development will be the study of the influence, on the oscillation frequency and on the onset of the meandering flow type, of the Froude number variation at constant non-dimensional depth, by varying the inflowing discharge. In this way, also the Reynolds number will vary, and the effect of its variation on the Strouhal number could be investigated too.

8.2. Sedimentation

As far as concern the study of the sedimentation processes in the reservoir, the performed experiments have shown that, for the hydraulic conditions in which the tests were performed, the sediments settle down mainly in the main jet, with a lower deposits amount in the lateral recirculation zones.

It has been possible to reproduce this sediments behaviour thanks to the new suspended sediments transport module implemented in the numerical model WOLF2D, even if also in this field a lot of work is still necessary before arriving at an accurate reproduction of sediments deposits thickness on reservoir bottom, and consequently to a reliable prediction of the trapping efficiency.

In the next future, a systematic sensitivity analysis concerning the influence on the results of the different parameters of the model will be carried out, in order to calibrate the model on the basis of the available experimental data collected in the framework of this thesis. In particular, the suspended sediments transport model could be modified in order to take into account multiple grain sizes, and different capacity transport laws could be implemented, instead of the Celik and Rodi transport capacity formulation implemented up to now.

An other important branch of the suspended sediments transport study will be the investigation about the damping effect caused by the sediments on turbulence. In fact, experimental results have shown that the presence of sediments in the inflowing water is able to change the flow pattern in the reservoir, and numerical simulations with different values of the turbulence parameter suggest that this effect could be caused by a reduction of turbulence caused by the fine suspended sediments.

So, further studies, numerical and experimental should be carried out in the future to confirm and investigate more deeply this important feedback effect of sediments on the reservoir fluid-dynamic.

In conclusion, even if the experiments and the simulations carried out in this research concern very regular geometries and controlled steady hydraulic conditions, which allow to classify this work mainly as a basic research in fluid mechanics and sediment transport, the obtained results,

conveniently adapted to real cases, could be useful to get a better insight on the complex mechanisms that govern flow patterns formation and sedimentation in more complex artificial or natural reservoirs.

NOTATION

A = reservoir surface (m^2);

B = reservoir width (m);

b = inlet and outlet channels width (m);

B/b = expansion ratio (-);

C = suspended solids concentration (g/l);

c_v, $c_{1\varepsilon}$, $c_{2\varepsilon}$, $c_{3\varepsilon}$, c_μ, σ_k, σ_ε = empirical coefficients for the k-ε model (-);

c_f = drag coefficient (-);

C_T = transport capacity (g/l) ;

C_{vol} = volumetric concentration (-);

D = distance between the laser light source and the top of sediments deposits (mm);

d = sediment diameter (m);

e = relative shifting between two partial average velocities (-);

E_1, E_2, E_3 = estimated fractional error (-);

E_k = average kinetic energy per unit mass (m^2/ s^2);

E_{k_tot} = experimental global kinetic energy content of the reservoir (m^4/s^2);

$E_{k\_tot\_k\text{-}\varepsilon}$ = numerical global kinetic energy content according to the k-ε model (m^4/s^2);

E_{k_unit} = specific kinetic energy content of the unitary surface of the reservoir (m^2/s^2);

E_{k_PF} = theoretical kinetic energy corresponding to a plug flow condition (m^2/s^2);

E_{k_ND} = non dimensional index corresponding the ratio between E_{k_unit} and E_{k_PF} (-);

f_1, f_2, f_3, = numerical solutions for the GCI evaluation (s);

f_{exact} = exact solution of the problem (-);

f = frequency of oscillation (1/s);

F_{in} = inlet Froude number (-);

g = acceleration of gravity (m/s^2);

GCI = global convergence index (-);

Δh = spatial discretization of the numerical mesh (m);

h = water depth (m);

h/b = non-dimensional depth (-);

J= friction slope (-);

k = turbulent kinetic energy (m^2/s^2);

k' = depth integrated turbulent kinetic energy (m^2/s^2);

K = von Karman constant (-);

L = reservoir length (m);

L/B = length-to-width ratio (-);

λ_x = scale of the subscript quantity x (-);

M = global moment of asymmetry (-);

m = local moment of asymmetry (-);

n =Manning roughness coefficient ($s/m^{1/3}$);

NTU = number of turbidity units (-);

i = order of convergence of the numerical method (-);

p = porosity of the deposits (-);

Q = discharge (m^3/s);

Q_s = solid discharge (g/s);

R = shape parameter proposed by Dewals et al. 2008 (-);

r = grid refinement ratio (-);

Rc = critical threshold of transition for the R parameter (-);

Re_p* = Reynolds particle number (-);

R_{in}= inlet Reynolds number (-);

S = output of the laser (V);

s = sediments deposits thickness (m);

St = Strouhal number (-);

t = time (s);

t_1 = temporal interval for integration (s);

T = non dimensional shape parameter (-);

T = period of oscillation of the meandering jet (s);

TE_1 = trapping efficiency linked to turbidimeters measurements (-);

TE_2 = trapping efficiency linked to deposits thickness measurements (-);

u = instantaneous longitudinal horizontal velocity component (m/s);

u = average longitudinal horizontal velocity component (m/s);

u' = fluctuating component of the **u** velocity (m/s);

U = coefficient of uniformity (-);

U* = friction velocity (m/s);

v = instantaneous transversal horizontal velocity component (m/s);

v = average transversal horizontal velocity component (m/s);

v' = fluctuating component of the **v** velocity (m/s);

v_{ss} = settling velocity (m/s);

V = instantaneous velocity vector (m/s);

V = depth-averaged velocity (m/s);

V' = fluctuating component of velocity (m/s);

V_{res} = theoretical plug flow velocity (m/s);

V_{nd} = non-dimensional velocity (-);

w = vertical velocity component (m/s);

W_{dep} = volume of deposited sediments (m^3);

x = longitudinal coordinate (m);

y = transversal coordinate (m);

z = vertical coordinate – height from the bottom of the reservoir (m);

z_b = elevation of the bottom (m);

z_o = reference height from the bottom (m);

α = empirical turbulent coefficient for the Fisher model (-);

α_s = turbulent coefficient for sediments (-);

α_{adapt} = empirical coefficient of calibration for the suspended transport module (-);

β = empirical coefficient of the Celik and Rodi formulation (-);

ΔE_{k_tot}= percentage deviation between experimental and numerical values of total kinetic energy (-);

ΔT = temporal interval (s);

ΔX = displacement vector (m);

ε = rate of dissipation per unit mass (m^2/s^3);

ε' = depth integrated rate of dissipation per unit mass (m^3/s^3);

ε_s = diffusivity of the sediments (m^2/s);

λ = scale of the subscript quantity between the model and the prototype (-);

μ = dynamic viscosity of water (Pa·s);

ν = cinematic viscosity of the water (m^2/s);

ν_T = eddy viscosity (m^2/s);

$\nu*$ = global eddy viscosity (m^2/s);

$\nu_{T\ 3D}$ = three dimensional eddy viscosity for isotropic turbulence(m^2/s);

$\nu_{T\ 2D}$ = two dimensional eddy viscosity (m^2/s);

ρ = water density (kg/m^3);

ρ_s = solids density (kg/m^3);

ρ_{dep} = density of sediments deposits (kg/m^3);

τ = Reynolds stress (N/m^2);

τ_w = wall tangential stress (N/m^2);

Subcripts:

- p = quantity referred to prototype;
- m = quantity referred to the model;
- G = geometry;
- in = inlet;
- out = outlet;
- num = numerical;
- exp = experimental;

REFERENCES

Abbott, D.E., Kline, S.J. (1962). Experimental investigation of subsonic turbulent flow over single and double backward facing steps. *J. Basic Engng.* 84(9), 317-325.

Absi R. (2011). An ordinary differential equation for velocity distribution and dip-phenomenon in open channel flows. *J. Hydr. Res.*,49,(1), 82-89.

Bagnold, R.A. (1966). An approach to the sediment transport problem from general Physics. *U.S. Geological Survey*, Prof. Paper 422-1.

Battaglia, F., Papadopaulus, G. (2006). Bifurcation characteristics of flows in rectangular sudden expansion channels. *Journ. Fluids Eng.*, 128, 671 – 679.

Bollaert, E., Irniger, Ph, Schleiss, A.J. (2000). Management of Sedimentation in a Multipurpose Reservoir in a run-of-river Power Plant Project on Alpine River. Proceedings of DYDRO 2000, 2-4 October, Bern, Switzerland, pp137-146.

Cao, Z., Carling, P.A. (2001). Mathematical modelling of alluvial rivers: reality and myth. Part 2: Special issues. Water and Maritime Engineering 154(4), 297 – 307.

Casarsa, L., Giannattasio, P. (2008). Three-dimensional features of the turbulent flow through a planar sudden expansion. *Physics of Fluids* 20(1), 1-15.

Celik, I., Rodi, W. (1991). Suspended sediment transport capacity for open channel flow. *Journ. Hydr. Engin.*, 117(2), 191 - 204.

Chanson, H. (1999). The Hydraulics of open channel flow: an introduction. Elsevier, Oxford.

Cherdron, W., Durst, F., Whitelaw, J.H. (1978). Asymmetric flows and instabilities in symmetric ducts with sudden expansions. *J. Fluid Mech.* 84(1), 13-31.

Chiang, T.P.,. Sheu, T.W.H, Wang, S.K. (2000). Side wall effects on the structure of laminar flow over a plane-symmetric sudden expansion. *Computers and Fluids* 29(6), 467-492.

Choi, S.U., Garcia, M.H. (2002). k $-\varepsilon$ Turbulence Modeling of Density Currents Developing Two Dimensionally on a Slope. J. Hydr. Eng., 128(55), 55-63.

Cloutier, D., Le Couturier, M.N., Amos, C.L., Hill, P.R. (2006). The effects of suspended sediment concentration on turbulence in an anular flume. *Aquatic Ecology*, 40, 555 – 565.

Davidson, M.R., Lawson, N.J. (1999). Numerical prediction of submerged oscillating jet flow. *Second International Conference on CFD in the Minerals and Processes Industries, CSIRO,* Melbourne, Australia, 6-8 December 1999.

Dewals, B.J., Kantoush, S.A., Erpicum, S., Pirotton, M., Schleiss, A.J. (2008). Experimental and numerical analysis of flow instabilities in rectangular shallow basins. *Env. Fluid Mech.* 8(1), 31-54.

Dewals, B. J., Erpicum, S., Detrembleur, S., Archambeau, P. and Pirotton, M. (2011). Failure of dams arranged in series or in complex, *Nat. Hazards.* Published online: 7 Aug. 2010. DOI: 10.1007/s11069-010-9600-z.

Dufresne M. (2008). La modelisation 3D du transport solide dans les basins en assainissement: du pilote experimental à l'ouvrage reel. *PhD Thesis,* Université Louis Pasteur, Strasbourg.

Dufresne, M. (2010). Ecoulement et dépôt de sédiments dans les bassins rectangulaires peu profonds. Mandat de post- doctorat à l'Ulg pour chercheur étranger, Liège, Belgium.

Dufresne, M., Dewals, B.J., Erpicum, S., Archambeau, P., Pirotton, M. (2010a). Classification of flow patterns in rectangular shallow reservoirs. *J. Hydraulic Res.* 48(2), 197-204.

Dufresne, M., Dewals, B.J., Erpicum, S., Archambeau, P., Pirotton, M. (2010b), Experimental investigation of flow pattern and sediment deposition in rectangular shallow reservoirs, *Int. J. Sediment Res.* 25(3), 258-270.

Dufresne, M., Dewals, B. J., Erpicum, S., Archambeau, P., and Pirotton, M. (2011). Numerical investigation of flow patterns in rectangular shallow reservoirs. *Engineering applications of computational fluid dynamics,* Accepted manuscript.

Durst, F., Melling, A., Whitelaw, J.H. (1974). Low Reynolds number over a symmetrical sudden expansion. *J. Fluid Mech.*, 64, 111 – 128.

Ernst, J., Dewals, B. J., Detrembleur, S., Archambeau, P., Erpicum, S. and Pirotton, M. (2010). Micro-scale flood risk analysis based on detailed 2D hydraulic modelling and high resolution land use data. *Nat. Hazards*, 55(2), 181-209.

Erpicum, S. (2006). Optimisation objective de paramètres en écoulements turbulents à surface libre sur maillage multibloc. Doctoral thesis, Université de Liège, Belgique.

Erpicum, S., Meile, T., Dewals, B. J., Pirotton, M., Schleiss, A. J. (2009). 2D numerical flow modelling in a macro-rough channel. *Int. J. Numer. Methods Fluids*, 61(11), 1227-1246.

Erpicum, S., Dewals, B.J., Archambeau, P. and Pirotton, M. (2010a). Dam-break flow computation based on an efficient flux-vector splitting. *Journal of Computational and Applied Mathematics*, 234(7), 2143-2151.

Erpicum, S., Dewals, B.J., Archambeau, P., Detrembleur, S., Pirotton, M. (2010b). Detailed inundation modelling using high resolution DEMs. *Engineering Applications of Computational Fluid Mechanics*, 2(4), 196-208.

Escudier, M.P., Oliveira, P.J., Poole, R.J. (2002). Turbulent flow through a plane sudden expansion of modest aspect ratio. *Phys. Fluids* 14(10), 3641-3654.

Fearn, R.M., Mullin, T., Cliffe, K.A. (1990). Nonlinear flow phenomena in a symmetric sudden expansion. *J. Fluid Mech*., 211, 595 – 608.

Flowmanager software and introduction to PIV instrumentation. Software User's Guide (2000). Dantec Dynamics, Denmark.

Graf., W.H., Altinakar, M. (2008). *Hydraulique fluviale*: Ecoulement et phénomènes de transport dans les canaux à géométrie simple. Presses Polytechniques et Universitaires Romandes, Lausanne.

Hannoun, I.A., Boulos, P.F. (1997). Optimizing distribution storage water quality: a hydrodynamic approach. Appl. Math. Modelling, 21, 495-502.

Honeylands, T.A., Molloy N.A. (1995). Oscillations of submerged jets confined in a narrow deep rectangular cavity. *Twelfth Australian Fluid Mechanics Conference*. University of Sydney, Australia, pp. 493 – 496.

Kantoush, S. A., Bollaert, E., Boillat, J.L., Schleiss, A.J. (2005). Suspended load transport in shallow reservoirs. Final Proc. XXXI IAHR Congress. Korea Water Resources Association, Seoul, South Korea, 1787-1799.

Kantoush, S.A. (2008). Experimental study on the influence of the geometry of shallow reservoirs on flow patterns and sedimentation by suspended sediments. Communication 37, Laboratory of Hydraulic Constructions, Ed. A.J. Schleiss, EPFL, Lausanne, ISSN 1661-1179.

Kantoush, S.A., Schleiss, A.J. (2009). Large scale PIV-measurements at the surface of different shallow reservoir geometries, Journal of Visualization 12(4), 361-373.

Koelzer, V.A., Lara, J.M. (1958). Densities and compaction rates of deposited sediments, Journal of the Hydraulic Division, 84, 2, 1603.

Labview^{TM} (2007). Getting started with Labview, User's Guide. National Instruments.

Launder, B.E., Spalding, D.B. (1972). *Lectures in mathematical models of turbulence,* Academic Press, London.

Meselhe, E.A., Peeva, T., Muste, M. (2004). Large Scale Particle Image Velocimetry for Low Velocity and Shallow Waters Flows. *Journ. Hydr. Eng.* , 130(9), 937-940.

Mizushima, J., Shiotani, Y. (2000). Structural instability of the bifurcation diagram for two-dimensional flow in a channel with a sudden expansion. *J. Fluid Mech.,* 420, 131-145.

Mizushima, J., Shiotani, Y. (2001). Transitions and instabilities of flow in a symmetric channel with a suddenly expanded and contracted part. *J. Fluid Mech.* 434, 355-369.

Morris, G.L., Fan, J. (1998). Reservoir sedimentation handbook: design and management of dams, reservoirs and watersheds for sustainable use. MacGrow Hill Professional, New York.

Nino, Y., Garcia, M. (1999). Engelund's analysis of turbulent energy and suspended load. *Journ. of Engin. Mech.*, 124(4), 480-483.

Oca, J., Masalò, I., Reig, L. (2004). Comparative analysis of flow patterns in aquaculture rectangular tanks with different water inlet characteristics. Aquacultural Engineering, 31, 221-236.

Oca, J., Masalò, I. (2007). Design criteria for rotating flow cells in rectangular aquaculture tanks. Aquacultural Engineering, 36, 36-44.

Persson, J., Somes, N.L.G., Wong, T.H.F. (1999). Hydraulic efficiency of constructed wetlands and ponds. Wat. Sci. Tech., 40(3), 291-300.

Persson, J. (2000). The hydraulic performance of ponds of various layouts. Urban Wat., 2, 243-250.

Persson, J., Wittgren, H.B. (2003). How hydrological and hydraulic conditions affect performance of ponds. Ecological Engineering, 21, 259-269.

Roache, P.J. (1994). Perspective: a method for uniform reporting of grid refinement studies.. *Annu. Rev. Fluid. Mech.*, 29,123-160.

Roache, P.J. (1997). Quantification of uncertainty in computational fluid dynamics. *Annu. Rev. Fluid. Mech.*, 29,123-160.

Roger, S., Dewals, B.J., Erpicum, S., Schwanenberg, D., Schüttrumpf, H., Köngeter, J., Pirotton, M. (2009). Experimental and numerical investigations of dike-break induced flows. *Journ. Hydr. Res.* 47(3), 349-359.

Shapira, M., Degani, D., Weihs, D. (1990). Stability and existence of multiple solutions for viscous flows in suddenly enlarged channels. *Comp. and Fluids* 18(3), 239-258.

Sobey, I.J., Drazin, P.G. (1986). Bifurcation of 2D channel flows. *J. Fluid Mech.* 171, 263-287.

Solitax sc User Manual, October 2005, Edition 3, Hach Company, Germany.

Stovin, V.R. (1996). The prediction of sediment deposition in storage chambers based on laboratory observations and numerical simulations. *PhD Thesis,* Department of Civil and Structural Engineering. University of Sheffield, Sheffield.

Stovin, V.R, Saul, A.J. (1994). Sedimentation in storage tank structures. *Wat. Sci. and Tech.* 29(1-2), 363-372.

Sumix Corporation (2006). Megapixel USB2.0 CMOS Camera User Guide. SMX-155 USB2.0 Cameras. Oceanside, CA.

Swamee, P. K., Ojha, C. S. P. (1991). Drag coefficient and fall velocity of non-spherical particles, Journal of Hydraulic Engineering, 117, 5, 660 – 667.

Thackston, E.L., Shields, F.D., Schroeder, P.R. (1987). Residence time distribution of shallow basins. Journal of Environmental Engineering 113(6), 1319-1332.

Ushijima, S., Kantoush, S.A., Sumi, T., Schleiss, A.J. (2009). Numerical prediction of flow instabilities in shallow basins. 23rd CFD Symposium, Sendai, Japan.

UVP Monitor – Model UVP-DUO with software version 3. User's Guide (2002). Metflow SA, Lausanne, Switzerland.

Van Rijn, L.C. (1993). *Principles of sediment transport in rivers, estuaries and coastal seas.* Aqua Publication, Amsterdam, The Netherlands.

Versteeg H.K., Malalasekera W. (1995). An introduction to computational fluid dynamics. The finite volume method. Longman, Essex, England.

Vreugdenhil, C.B. (1994). *Numerical methods for shallow-water flow*, 21-25. Kluwer Academic, Dordrecht.

Wang, L.P., Maxey, M.R. (1993). Settling velocity and concentration distribution of heavy particles in homogeneous isotropic turbulence. J . Fluid Mech., 256, 21-68

Weitbrecht, V., Kuhn, G., Jirka, G.H. (2002). Large scale PIV-measurements at the surface of shallow water flows. Flow measurement and Instrumentation 13, 237-245.

Wille, R., Fernholz H. (1965). Report on the first European Mechanics Colloquium, on the Coanda effect. *J. Fluid Mech.* 23(4), 801-819.

Wood, M.G., Howes, T., Keller, J., Johns, M.R. (1998). Two dimensional computational fluid dynamic models for waste stabilization ponds. Wat. Res., 32(3), 958 – 963.

Wu, W. (2008). Computational river dynamics. Taylor and Francis, London.

PUBLICATIONS

For conferences:

Camnasio, E., Schleiss, A.J.. (2010a) 1st EPFL Doctoral conference in Mechanics: Advances in modern aspects of fluid mechanics - Flow fields investigation in shallow reservoirs, Lausanne, Switzerland, February 2010

Camnasio, E., De Cesare, G., Kantoush, S. (2010b). 7th ISUD Conference, Goteborg, Sweden, April 2010 - Flow field and sediment deposition in a rectangular shallow reservoir with non symmetric inlet and outlet configuration.

Camnasio, E., Erpicum, S., Orsi, E., Pirotton, M., Schleiss, A.J., Dewals, B. (2012a). 6th International Conference on Scour and Erosion, Paris, France, 27-31 Agoust 2012. Feedback from reservoir sedimentation on the flow pattern in rectangular basins. (abstract sent for acceptance)

Camnasio, E., Dewals, B. (2012b). 3rd International Symposium on Shallow Flows, Iowa, USA, 4-6 June 2012. Experimental and numerical investigation of a meandering jet in a shallow rectangular reservoir under different hydraulic conditions. (abstract sent for acceptance)

For peer reviewed journals:

Camnasio, E., Orsi, E., Schleiss (2011). Experimental study of velocity fields in rectangular shallow reservoirs. Journal of Hydraulic Research, 49(3), 352-358.

Camnasio, E., Erpicum, S., Orsi, E., Pirotton, M., Schleiss, A.J., Dewals, B. (2011). Effects of inlet and outlet location on flow patterns and sedimentation in a rectangular basin. International Journal of Sediment Research (under review).

Co-supervision for Bachelor and master thesis:

Celenza, A., (2010). Caratterizzazione del campo di moto e turbolenza in un serbatoio di acque basse di dimensioni variabili: analisi con tecnica LSPIV. Relatore: prof. Orsi Enrico, Correlatrice: Ing. Camnasio Erica. Tesi di laurea specialistica in Ingegneria civile, Politecnico di Milano.

Carrara, S., Gervasoni, L. (2010). Caratterizzazione del campo di moto in un serbatoio di acque basse rettangolare di dimensioni variabili. Relatore: prof. Orsi Enrico, Correlatrice: Ing. Camnasio Erica. Tesi di laurea in Ingegneria civile, Politecnico di Milano.

ACKNOWLEDGEMENTS

At the end of these three years of doctoral studies, there are many people which I would like to thank sincerely:

- my family, which supported me in every moment;
- my supervisor prof. Enrico Orsi and my tutor prof. Alberto Guadagnini of Politecnico of Milan, which were two excellent guides for me during these years;
- prof. Anton Schleiss and the entire L.C.H. staff of Ecole Polythecnique Fédérale de Lausanne, who hosted me in a very kind way for six months, giving me the opportunity to carry out precious experiments and to live a beautiful experience of life;
- prof. Michel Pirotton of Liège University, who was so kind to invite me to join his research group to carry out the numerical simulations, and prof. Benjamin Dewals who was a very effective fellow of my work, helping me with precious suggestions and explaining me in a very clear and patient way the features of the software WOLF;
- the entire staff of the Hydraulic Section of the D.I.I.A.R. at Politecnico of Milano, which made funny and unforgettable my days of work.